Optics and Optoelectronics of Two-dimensional Semiconducting Monolayers and Heterostructures

Jason Solomon Ross

A dissertation

submitted in partial fulfillment of the

requirements for the degree of

Doctor of Philosophy

University of Washington

2016

Reading Committee:

Xiaodong Xu, Chair

Arka Majumdar

Lih-Yuan Lin

Program Authorized to Offer Degree:

Materials Science & Engineering & Nanotechnology

University of Washington

Abstract

Optics and Optoelectronics of Two-dimensional Semiconducting Monolayers and Heterostructures

Jason Solomon Ross

Chair of the Supervisory Committee:
Associate Professor Xiaodong Xu
Physics and Materials Science & Engineering

Until recently, the physics of truly two-dimensional (2D) excitons could only be explored theoretically. Following the discovery of graphene, many 2D materials were quickly identified and isolated, one system being the semiconducting Group VI-B transition metal dichalcogenides (TMDs). These semiconductors are the first air-stable materials that are atomically thin (three atomics thick), and yet can be produced in arbitrarily large lateral sheets. They have a direct band gap in which confinement leads to large spatial overlap of electrons and holes resulting in strongly coupled excitonic transitions that dominate light-matter interactions. The direct band-gap of monolayer TMDs occurs at the corners of the hexagonal Brillouin zone, referred to as the K valleys. Entirely unique to these materials, excitons in adjacent K valleys selectively couple to light of opposite circular polarization, i.e. the K (K') valley is selective to right (left) circularly

polarized photons. This property offers the possible realization of novel devices that will manipulate the valley index, known as valleytronics. Further, creating a stacked heterostructure (HS) of two TMD monolayers of different molecular species can exhibit type-II band alignment leading to the first atomically sharp built-in p-n junction and a bright interlayer exciton with long lifetimes. Being flat 2D sheets, it is easy to couple these materials to nearby systems such as microfabricated electrodes and photonic crystal cavities allowing for unique modulation and device schemes.

Here, I employ both optical and electronic techniques to study the unique physics of 2D excitons in TMDs as well as demonstrate some of their first optoelectronic and valleytronic devices. The most notable achievement is perhaps the first demonstrations of both atomically thin and 2D heterostructure light emitting diodes and photovoltaic devices. Other breakthroughs include the first demonstration of exciton charging tunability in a 2D system, the first valleytronic demonstration via electrical control of the degree of valley polarization, and resonant excitation investigations of the interlayer exciton's role in absorption and emission in heterostructures. This work paves the way for future studies of 2D semiconducting systems and utilizing them in important new devices ranging from LEDs to photovoltaics to photonically coupled nanosystems such as a 2D nanolaser.

TABLE OF CONTENTS

LIST OF FIGURES

Page

ACKNOWLEDGEMENTS

I would like to thank first and foremost my principle investigator Xiaodong Xu for his unmatched support, intellectual contribution, and intuition for what is important. I would also like to thank Prof. Di Xiao of Carnegie Mellon University along with Prof Wang Yao and Dr. Hongyi Yu of Hong Kong University for their priceless theoretical contributions, Prof. David Cobden for providing essential equipment and enlightening discussions, Prof. David Mandrus for MX_2 crystal synthesis, and Professor Arka Majumdar for his collaborations related to photonic crystal cavities. I would like to thank Dr. John Schaibley, Dr. Grant Aivazian, Dr. Aaron M. Jones, Sanfeng Wu, Pasqual Rivera, Genevieve Clark, Kyle Seyler for discussions and support with optical measurements, Eric Lee Wong, Marie Scott and Philip Klement for assistance in device fabrication, and The Washington Nanofabrication Facility, especially Richard Bojko for support with electron beam lithography. And last but not least, I would like to extend a warm thank you to my lovely wife, Keiren Bond, for her constant injection of moral support, calming words, and unending optimism that has fueled my motivation to complete my research and this degree.

DEDICATION

I dedicate this thesis to my parents, Ellie and Elliot Ross who have always respected and promoted my interests and pursuits even if it meant driving me across LA county for acting auditions or loaning me money so I can afford the skyrocketing cost of attending university in USA.

Chapter 1. INTRODUCTION

The two-dimensional (2D) material gold-rush began in 2004 with the discovery and characterization of graphene[1], a semi-metallic monolayer of carbon atoms that form a hexagonal structure. Graphene exhibits massless Dirac fermions[2], ultrahigh electron mobility of 200,000 $cm^2V^{-1}s^{-1}$[3], 2-3% broadband absorption of visible light [4, 5], and extraordinary mechanical properties. Since then, many stable 2D crystals have been recognized, isolated, or predicted[6]. Of these, there are two of important note for this work.

First, there is the insulating hexagonal boron nitride (BN), an atomically flat hexagonal layer like graphene but with a boron and nitrogen atom making up the crystalline base. It has a band gap of 5.97 eV [7], a relative dielectric constant of 3-4, and a breakdown voltage of roughly 0.7 V nm^{-1} [8]. With these properties and its atomically smooth surface, BN has proven to be the ideal substrate and gate dielectric for bringing out the intrinsic properties of other 2D materials[9].

Second, and the main focus of this work, there is the semiconducting group-VIB transition metal dichalcogenides (TMDs)[10]. This is a family of 2D materials in itself, all of which represent the first group of air-stable, semiconducting monolayers discovered. Single molecular layers of TMDs have a direct bandgap[11] leading to optical properties that are dominated by tightly bound excitons[12–17] with emissions in the visible to NIR regime. Further, the optical properties are electrically tunable[12, 14] and exhibit unique selectivity to polarized light[13, 18–21]. Integration with graphene and BN has brought forth an all-2D devices paradigm with working FETs, photodetectors, p-n junctions, and LEDs[6, 22–24].

Exciton physics confined to a plane has mainly been studied in quasi-2D quantum well heterostructures such as GaAs. Here, the carrier wavefunction occupies at least tens of atomic

layers. Investigating and applying the physics of truly 2D excitons has thus been a long pursued goal, motivated centrally by the expectation that binding energies will be largely enhanced in the 2D limit[12, 25], providing stable states even at room temperature. In addition, being flat atomic sheets, 2D materials are highly responsive to external stimuli such as electrostatic gates[26], ions gels[27], self-assembled molecules[28], doped substrates[29], and, as will be described in detail in this work, light-matter interactions. It's also obvious that building the next generation of electronic and optoelectronic devices out of atomically thin materials offers the ultimate miniaturization of solid state systems while maintaining the ability for large-area mass production akin to silicon. This means more efficient use of materials, lower power requirements, and the possibility of realizing completely novel devices and applications.

The aim of this work is to elucidate some of the first breakthroughs made in realizing the above advantages and prospects in the context of 2D semiconducting TMDs. In Chapter 2, I present an overview of the crystallographic, electronic, and optical properties of 2D TMDs. I will also introduce TMD heterostructures and describe the novel methods of constructing 2D material stacks which were developed in the course of this research.

In Chapter 3, I explore how the physics of excitons is modified due to confinement in two dimensions leading to large binding energies and charged excitons. Demonstrations of electrostatic control of the exciton charging effect are described in detail.

Chapter 4 demonstrates how 2D material stacking techniques led to the creation of the first light emitting diode and p-n junction photovoltaic from all-2D materials. Tuning of the excitonic emission of this device is discussed.

This work concludes with Chapter 5 where the properties of TMD heterostructures are discussed in detail and the first demonstration of electroluminescence from the interlayer exciton

is described. Resonant excitation photocurrent measurements are also presented which explore the role of the interlayer exciton in heterostructure TMD optoelectronics.

Chapter 2. 2D TRANSITION METAL DICHALCOGENIDES

In this chapter I introduce the structural, electronic, and optical properties of monolayer TMDs including their unique, polarization-selective light-matter interactions. I also briefly describe heterostructures made from two TMDs and the monolayer stacking techniques involved in making them.

2.1 TMD STRUCTURE

Group VIB TMDs have the molecular formula MX_2 where M is the group-VIB transition metals Mo or W and X is the chalcogens S or Se. Monolayer TMDs show only two polymorphs, trigonal prismatic and octahedral. This thesis focuses on the former, which form 2D hexagonal crystals with trigonal prismatic coordination around the metal atom belonging to the D3h point group [30] (Figure 2.1a). Extending this out in two dimensions, the monolayers form in what is called the 2H phase and lack an inversion center, as made apparent when looking at a monolayer lattice from the side (Figure 2.1b). This lack of symmetry is a vital ingredient in making the properties and applications of 2D TMDs exciting, as well be discussed in length throughout this thesis. With strong in-plane covalent bonds, these 2D crystals (Figure 2.1c) can extend indefinitely in the lateral direction but only weakly bond to other layers via Van der Waals forces in the vertical direction. Owing to this property, 2D materials are also commonly referred to as Van der Waals materials[6] and can all be isolated via mechanical exfoliation using adhesive tape, first popularized with graphene [2]. And with a lack of dangling bonds on the surface of these materials, they are stable in air up to hundreds of degrees centigrade[30].

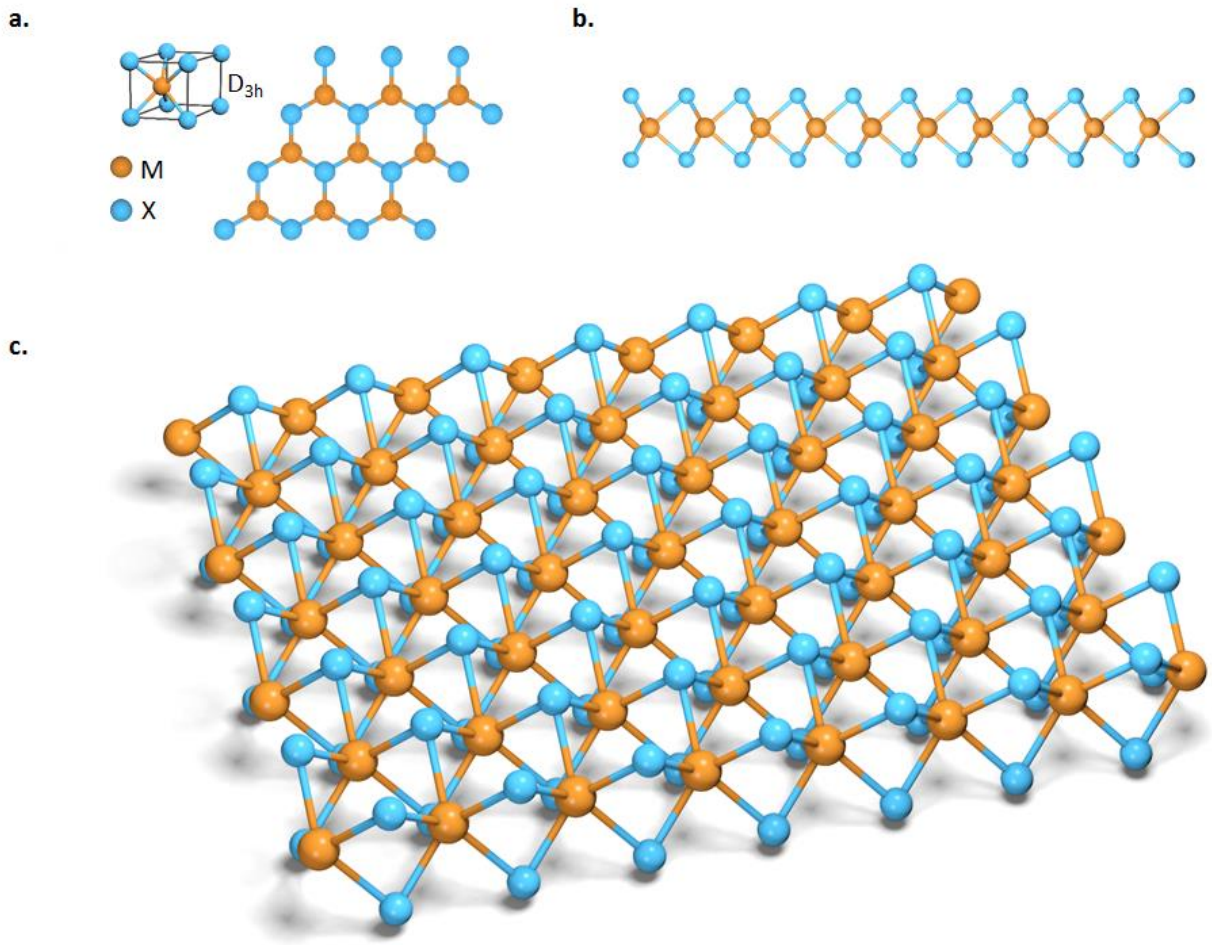

Figure 2.1. **Monolayer TMD Crystal Structure**. **a,** Coordination structure and top view of monolayer TMD. **b,** front and side view of monolayer. **c.** 3D schematic of monolayer crystal piece.

2.2 2D Semiconducting Properties and Devices

Without a way to chemically dope monolayer TMDs, initial studies focused on field effect transistors (FETs) to characterize their semiconducting properties via electrostatic doping. These early works used standard electron beam lithography (EBL) and metal evaporation to define

electrodes which showed room temperature mobility on the order of 10 to 100 $cm^2V^{-1}s^{-1}$ [26, 31]. With ion gel gating, ambipolar conduction behavior was observed, giving promise to future p-n junction studies[22], which is the focus of Chapter 4 of this paper.

Device performance of these initial studies and most still today is largely inhibited by the poorly understood Schottky barriers that form between the 2D semiconductor and the 3D metal contact. This manifests as contact resistances on the order of giga-ohms and poor carrier concentrations on the order of 10^{12} cm^{-2} at large gate voltages[12]. Three recent advances circumvent this barrier. One study made metallic contact to the edge of few-layer WSe_2 following a recent breakthrough where a one-dimensional contact to the edge of a graphene sheet showed mobilities approaching the theoretical limit[32]. In the WSe_2 few-layer case, field effect mobility as high as 6000 $cm^2V^{-1}s^{-1}$ is observed at low temperature[33]. Another workaround implements a thin, < 1 nm, layer of BN between the metal contacts and the monolayer TMD. Being so thin, electrons easily tunnel through the BN layer under a bias voltage [34, 35] but a large Schottky barrier buildup is avoided. This has the added bonus of being able to electronically access TMDs that are encapsulated in BN layers while serving as a protecting layer and providing an ideal dielectric environment for 2D excitons. Such TMD devices have shown resistances as low as 1 KΩ and offer the ability to measure 2D materials that are otherwise unstable in ambient conditions[36, 37]. Finally, lithium ion intercalation into 2D semiconductors has demonstrated the ability to convert the crystal structure and thus properties of the material. Specifically, it forces a phase transition from the regular 2H phase (semiconducting) to 1T phase (metallic) greatly reducing contact resistances from the MΩ regime to just hundreds of Ω[38]. In this thesis I will mostly take advantage of the tunneling BN contact as demonstrated in Chapter 4 on heterostructure LEDs. This method is chosen as it is the easiest to implement and simultaneously provides device passivation.

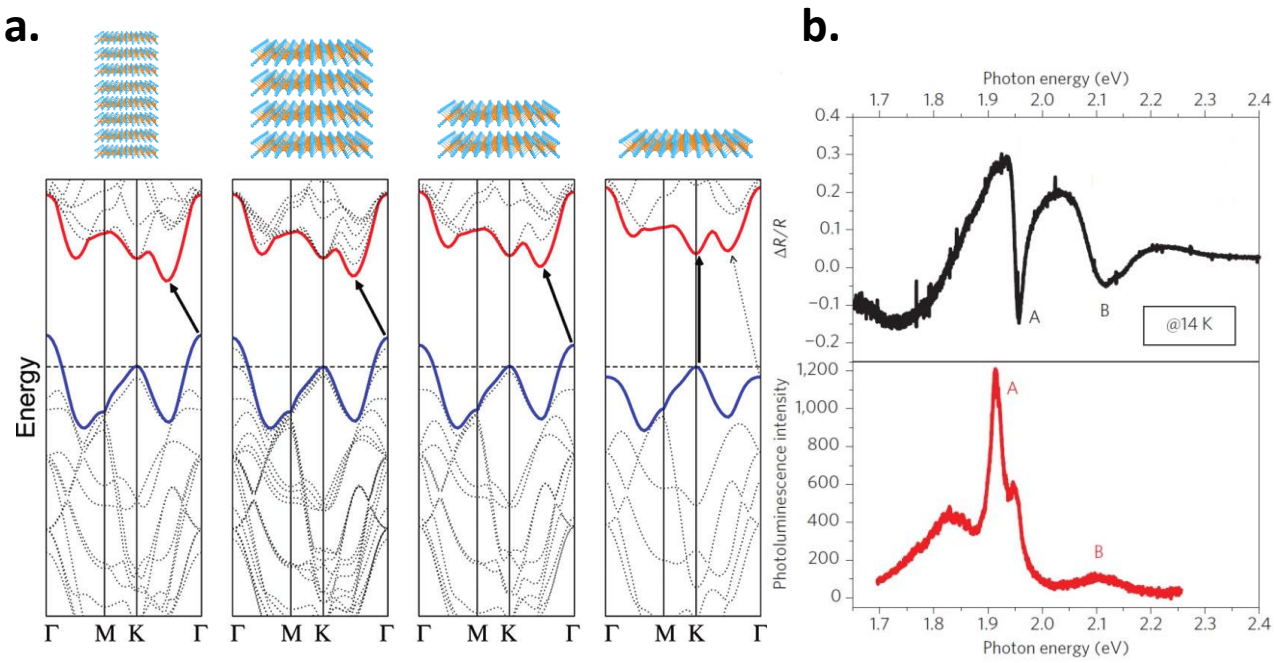

Figure 2.2. **Monolayer direct band-gap and 2D excitons**. a, MoS_2 band structure as a function of number of layers. From left to right: bulk, 4-layer, 2-layer, single layer. From reference [39]. b, Reflectance and photoluminescence spectra of monolayer MoS_2 at 14 K. Taken from reference [20].

2.3 2D Exciton Optics

Monolayer TMDs are endowed with exceptional optical. When thinning bulk TMDs from several layers down to a single monolayer, the electronic bandgap transitions from indirect to direct (Figure 2.2a), fulfilling the most basic requirement for efficient light emission [11, 39]. Additionally, large carrier effective masses and reduced screening in 2D yield electron-hole interactions that are much stronger than in conventional semiconductors, resulting in exciton binding energies on the order of hundreds of meV[15–17]. This leads to neutral and charged

excitons with large binding energies dominating the optical properties of TMDs. In fact, the binding energies are so significant that room temperature photoluminescence (PL) is attributed entirely to excitons and shows no electronic band-edge emission.

At low temperatures, reflectance and PL features clearly show A and B exciton states with energy splitting corresponding to the spin-splitting of the valence band (Figure 2.2b) [20]. PL emission also exhibits spectrally sharp (FWHM < 5 meV), well separated (~30 meV) charged exciton states that are amenable to electrical manipulation [12–14]. Details of 2D exciton physics are the focus of Chapter 3 of this thesis. With optical properties that rival quasi-2D systems, it is natural that a lot of attention is being given to making optoelectronic devices to take advantage of this new realm. Groundbreaking 2D versions of photodetectors[40–43], solar cells[44–46], and light-emitting diodes[37, 47–52] have already been made. Details of the first 2D LED is the focus of Chapter 4 of this paper. And with the ability to integrate 2D TMDs with planer photonic crystal cavities that lead to emission enhancement[53] and even optically pumped lasing[54], exciting 2D nanophotonic devices such as a 2D nanolaser seem right around the corner.

2.4 Unique Optics: Spin and Valley Physics

Monolayer TMDs have a direct bandgap ranging from 1 to 2 eV [30] where the direct transition is located at the corners of the hexagonal Brillion zone, known as the K valleys (Figure 2.3**,** a and c). Due to strong spin-orbit coupling, the valence and conduction bands are spin-split at the K points[55]. The effects are most pronounced in the valence band with splitting ranging between 150-450 meV depending on the TMD (Figure 2.3b). Additionally, due to time reversal symmetry and the lack of inversion symmetry, equivalent bands in opposite valleys must have opposite spin, therefor distinguishing the –K and +K valleys as unique (Figure 2.3c).

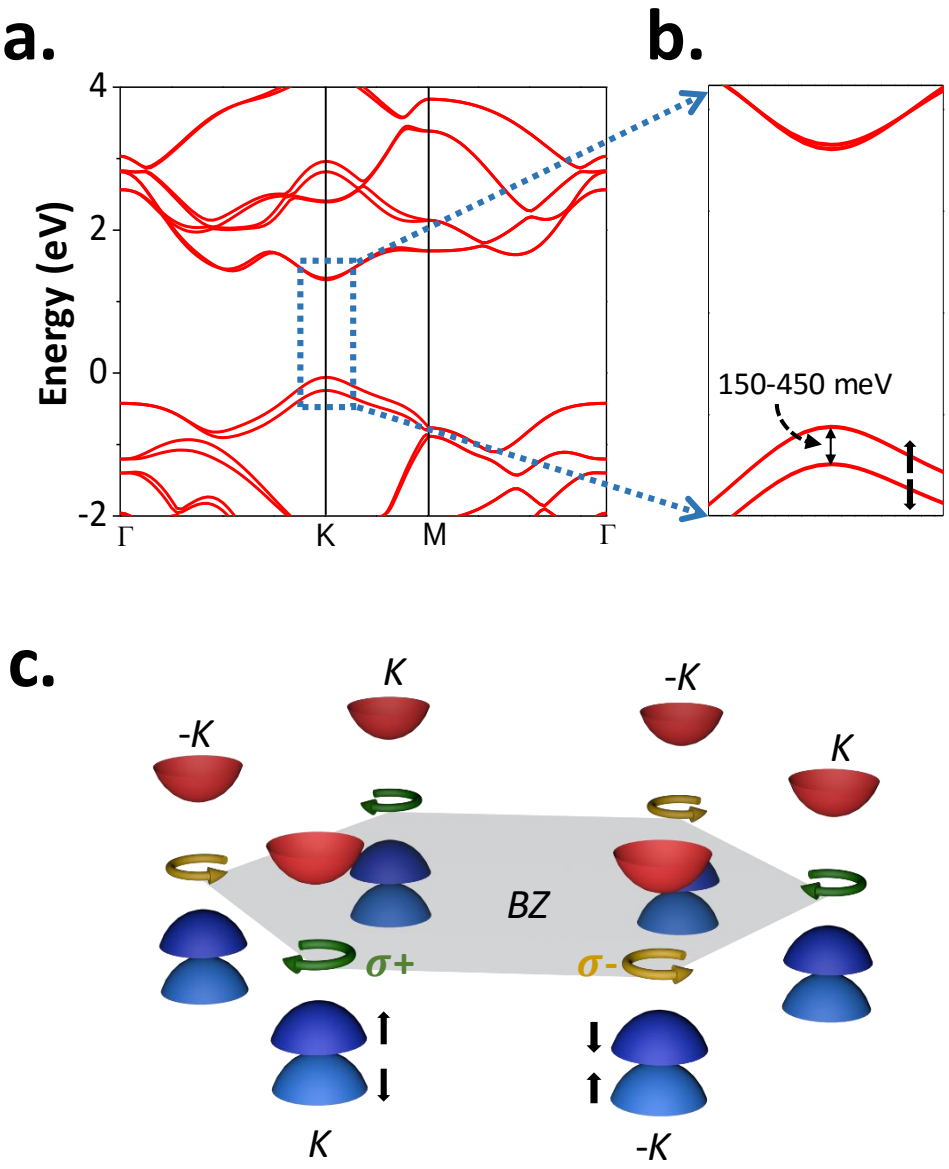

Figure 2.3. **Spin and Valley Properties**. **a**, Density function theory calculated band structure. **b**, band structure at K point shows hundreds of meV valence band splitting due to spin-orbit coupling. Black arrows represent spin. **c**, Circularly polarized optical selection rules at K points in the hexagonal Brillouin zone (BZ). Right-circularly polarized light couples to the K valley with spin up holes while left-circularly polarized light couples to the –K valley with spin down holes.

This leads to perhaps the most interesting fact about these materials. That there is a difference in optical properties of excitons between the K and -K valley. Unique to monolayer TMDs, The combination of large spin-orbit coupling[55] and a lack of inversion symmetry provides a connection between spin and valley degrees of freedom[18], light polarization[13, 20, 21, 56], and magnetic and electric fields[57] that can be exploited for novel device platforms and operations. Specifically, along with the opposite spin splitting in the two K valleys, each valley selectively absorbs and emits opposite circularly polarized photons (curved arrows in K valleys in Figure 2.3c). As of yet, they are the only known materials to intrinsically possess this property without outside stimuli or non-equilibrium crystal modification.

With WSe_2 as the prime material example, the above properties have shown to result in two significant consequences in terms of optical excitation measurements of TMDs. 1) When circularly polarized light is incident on TMDs, the PL of all exciton states will show an overall circular polarization that matches the excitation (Figure 2.4a) [20, 21, 56]. 2) When linearly polarized light is incident, the PL of the neutral exciton alone follows the polarization axis of the excitation (Figure 2.4b). To understand this, first consider that linear polarized light can be written as a superposition of right and left circularly polarized light, $H \propto \sigma_+ + \sigma_-$. So in WSe_2, a coherent superposition of K and –K valley states persists through absorption of the excitation laser and then through emission as measured by PL. Thus linearly polarization of the neutral exciton is evidence of valley coherence[13] which suggest that this system might offer a new scheme for quantum mechanical computation.

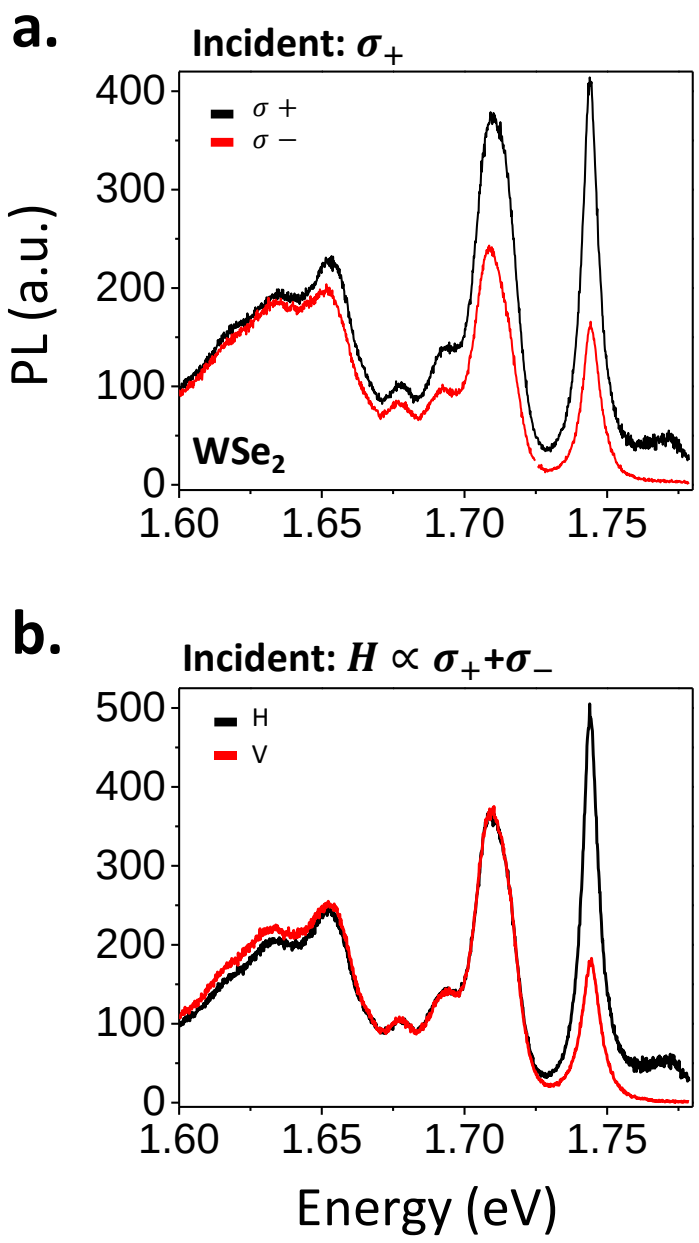

Figure 2.4. **Valley Dependent Photoluminescence. a**, The photoluminescence of WSe_2 under a right circularly polarized excitation (σ_+) will show stronger right circularly polarized emission (black) as opposed to left (red) for all exciton states (Xo and X- here). **b.** Under linearly polarized excitation such as horizontal here (H), the PL of the neutral exciton alone follows the excitation polarization. Adopted from reference [13].

Since inversion symmetry is restored in AB stacked bilayers and PL is very week in multilayers, valley polarized emission is only significant in monolayer TMDs. However, there is a twist in the story of bilayer polarization that was observed early on. It was found that you could turn on the valley polarization in bilayers and even tune the degree to which it is polarized. To explain, let us first examine the crystal symmetry of this monolayer TMD.

Figure 2.5a shows side view schematics of MoS_2 crystals. In the monolayer case, no inversion center can be found. In contrast, AB stacked bilayers open up an inversion center (arrow reticle in

Figure 2.5a middle). This should turn off valley polarization by making K valleys equivalent. However if an FET device is fabricated such that a gate voltage V_G will apply a vertical, out-of-plane E-field across the bilayer, the inversion symmetry can be broken (

Figure 2.5 right). This was found to tune the degree of valley polarization $\eta = \frac{\sigma_+ - \sigma_-}{\sigma_+ + \sigma_-}$, where $\sigma_\pm$ is the PL signal for a right and left circular polarization, across a range of -15% to 15% [58]. This is illustrated in

Figure 2.5b where I see the valleys switch their preference for left or right circular polarization due solely to inversion symmetry breaking as a function of gate voltage. This result can be considered the first demonstration of so-called valleytronics.

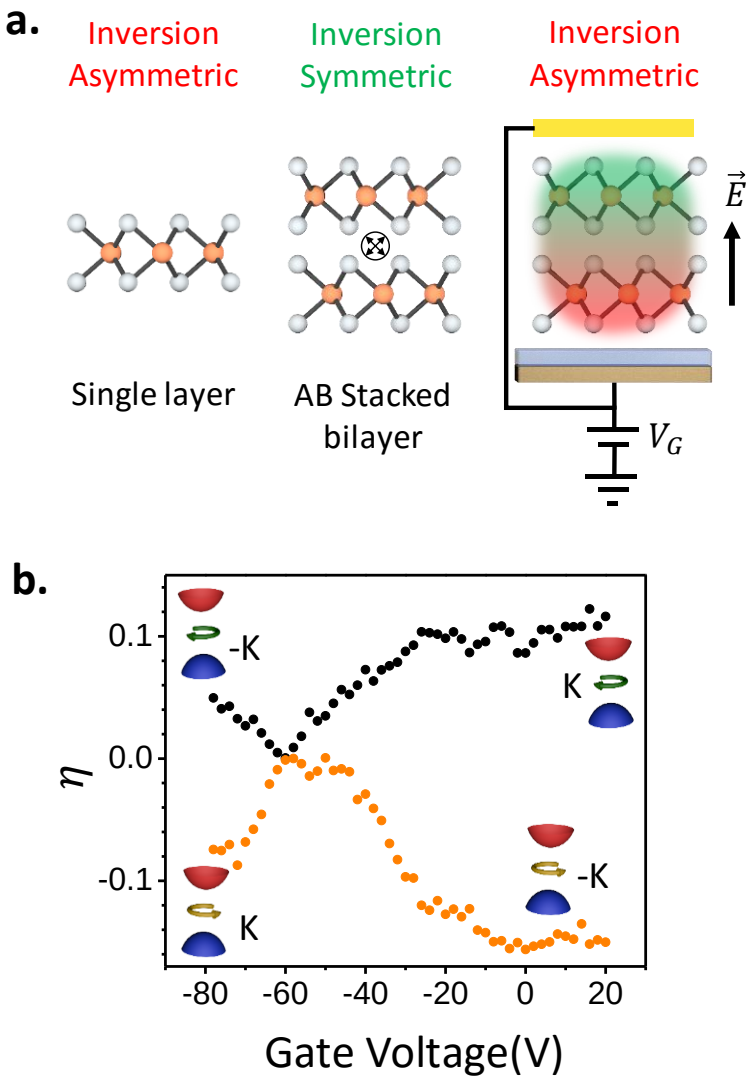

Figure 2.5. **Inversion Symmetry Tuning. a**, Schematic of mono- and AB stack bi-layer MoS_2 illustrating how an electric field in the vertical direction can break the inversion symmetry of the bilayer. **b.** As a function of the gate voltage, the degree of valley polarization is turned on and off and even reversed in terms of which valley (K and –K) prefers which helicity of light (curved arrows).

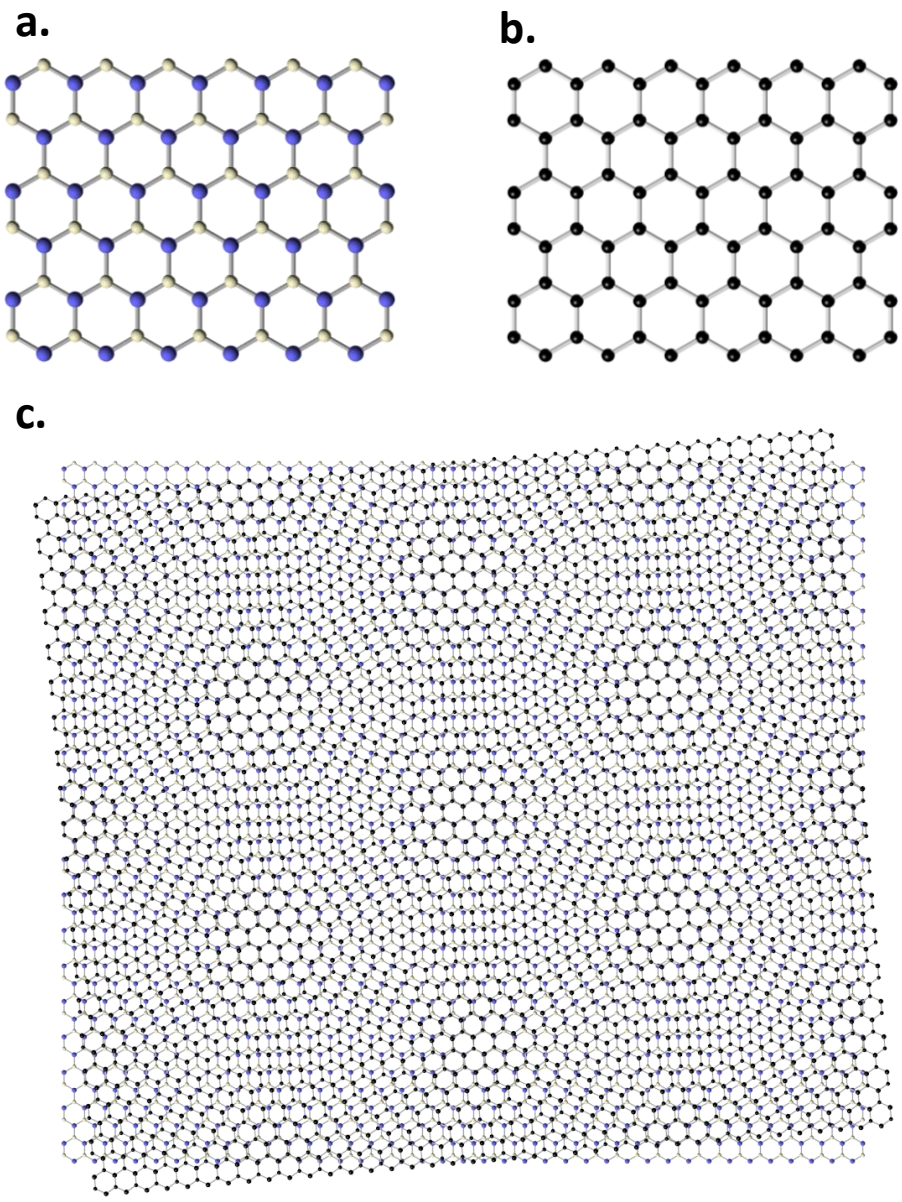

Figure 2.6. **Graphene-BN Superlattices. a**, Top view of small boron nitride (BN) 2D lattice. Boron atoms are blue and nitrogen atoms are gray. **b.** Top view of graphene lattice with black carbon atoms. **c.** Top of larger sheets graphene on BN with 5-degree twist angle. An obvious superlattice pattern forms in this heterostructure which can lead to modified electronic and optical properties for the constituent materials.

2.5 2D SUPERLATTICES AND HETEROSTRUCTURES

Interest in Van der Waal heterostructure (HS) combinations of TMDs, graphene, and BN has existed since the discovery of these materials[6], motivated largely by the chance to study superlattices and atomically sharp quantum wells. For instance, if one takes a monolayer BN crystal (Figure 2.6a) and places it on top of a crystal of graphene (Figure 2.6b) with a small twist angle between the lattices, a repeating heterostructure pattern with unit cell size larger than the constituent materials forms, known conventionally as a Moiré pattern. Figure 2.6 illustrates this for a twist angle of 5 degrees showing a new larger hexagonal pattern forming. This type of HS is more technically called a superlattice and the superimposed lattice repetition can have dramatic effects on the constituent heterostructure materials. In graphene on BN, the superlattice provides ideal length scales allowing access to the Hofstadter butterfly fractal pattern created by the recursive interplay of Landau levels and Block bands that would normally be inaccessible at practical magnetic fields in isolated graphene[59–61].

More important for this thesis, if one stacks two different TMD materials such as $MoSe_2$ and WSe_2 (Figure 2.7a), recent work has predicted type II band alignment can occur[62–65]. This is when the smallest energy transition in the combined HS band diagram is between the valence band of one material and the conduction and of the other (Figure 2.7b). This causes free electrons and holes to charge transfer and separate to opposite layers [66, 67]. Evidence for this has been observed in WSe_2-$MoSe_2$ HSs where a bright, long-lived, indirect exciton state is emerges at a lower energy than the regular intralayer excitons [68]. The indirect exciton binding energy is widely tunable with an applied vertical electric field because it is essential an interlayer electric dipole formed between electrons in one material and holes in the other. In other words, there is evidence for an atomically sharp p-n junction where the built-in field is widely tunable and controls

a tunable bright exciton. This is exciting both intellectually and technologically. Further details of TMD HS physics and a demonstration of the first LED and photodetector based on the interlayer exciton is the detailed in Chapter 4 of this thesis.

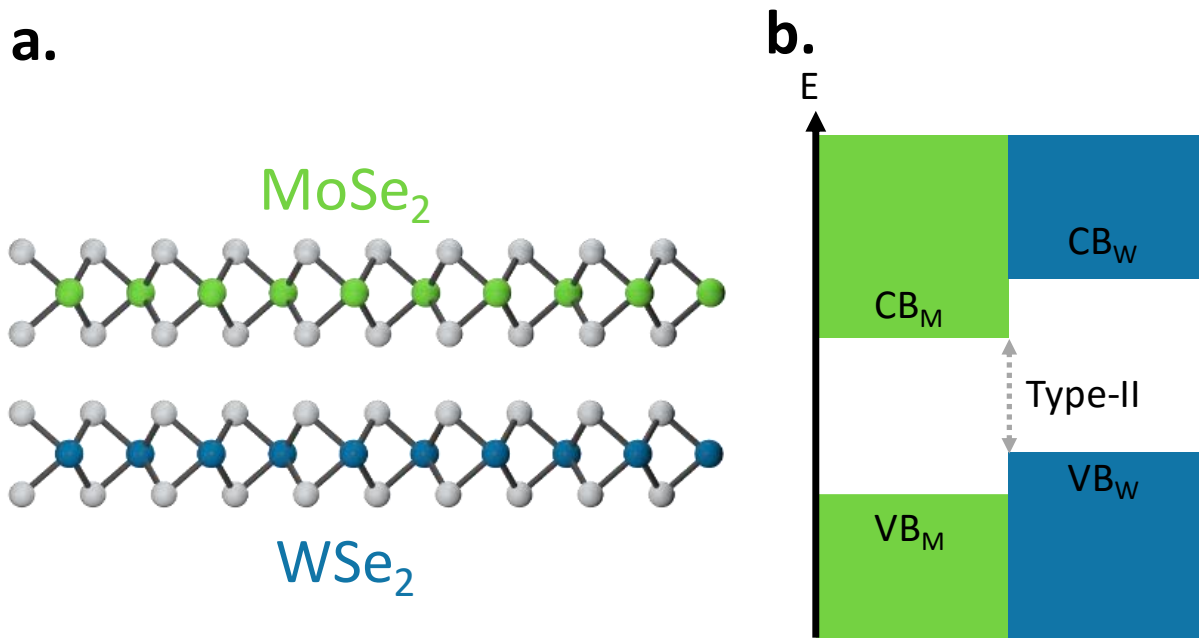

Figure 2.7. **TMD Heterostructures. a.** Front view of $MoSe_2$ (green metal atoms) crystal on top of WSe_2 (blue metal atoms) crystal. **b.** Energy band alignment of the heterostructure in (d). Due to differing work functions, the lowest energy conduction band is in $MoSe_2$ while the highest energy valence band is in WSe_2, together known as type-II band alignment.

2.6 Exfoliation and Transfer Techniques

Mechanically exfoliated samples are still favored for their higher crystalline quality and intrinsic properties. This is especially true for TMDs where no direct-to-monolayer growth method

has produced crystals with purity or properties like the exfoliated variety. And so in this thesis, I focus on 2D materials that have been mechanically exfoliated onto 300 nm silicon oxide (SiO_2) on highly doped Si substrates. This is simply accomplished by spreading bulk TMD crystals across adhesive tape through repeated self-sticking then pressing the tape down onto the silicon chip and rubbing out the bubbles before pulling back the tape (Figure 2.8a). From there, they are either studied directly, fabricated into simple FETs, or combined with other exfoliated samples to form HS devices. The reason for the 300 nm thick SiO_2 is that it maximizes the contrast of a single layer of material when viewed in an optical microscope. This fact was the first major breakthrough for isolating and characterizing graphene and subsequently all 2D layered materials[1, 10]. For TMDs studied in this thesis, due to efficient absorption of visible light, optical contrasts of about 10% are observed on 300 nm SiO_2 (Figure 2.8b). Now if this is how one finds individual layers, how are separate 2D material samples combined into a HS? The answer is collectively known as transfer techniques, and its rapid evolution over the past few years is described below.

The first transfer technique was borrowed from graphene CVD growth methods. Graphene monolayers grow most effectively on metal substrates such as copper[69] and nickel[70] and so they must be transferred to insulating substrates like SiO_2 before they can be made into devices and studied. The solution is to spin-coat a layer of PMMA, a standard EBL resist, and then etch away the metallic substrates leaving monolayers of graphene stuck to a PMMA membrane floating on water. These are then scooped up by a clean SiO_2 chip and the PMMA is subsequently dissolved away in acetone[69].

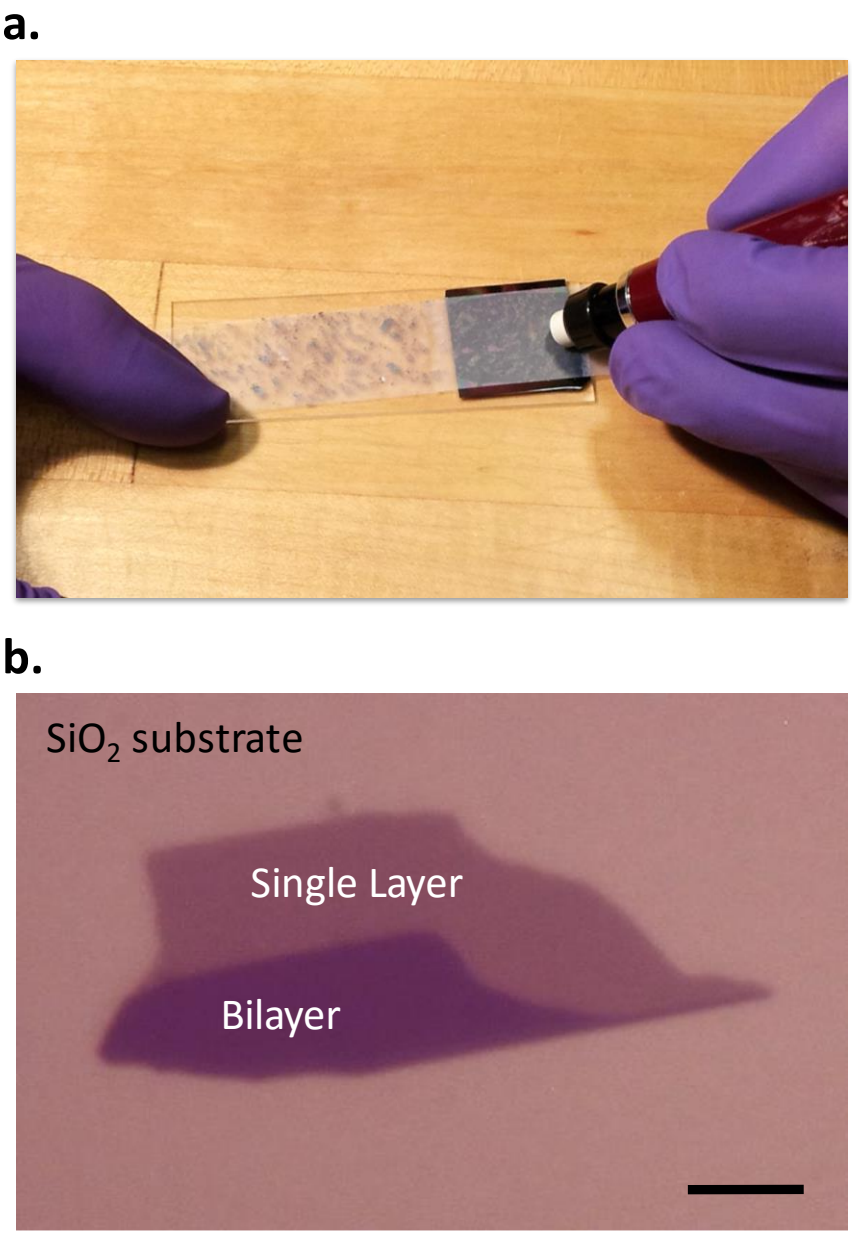

Figure 2.8. **Mechanical Exfoliation. a.** Rubbing out the bubbles in adhesive tape on a silicon oxide chip. After peeling back the tape, monolayer materials can be found deposited on the substrate. **b.** White light illuminated optical micrograph of a WSe_2 sample showing single and bilayer regions. The single layer has about a 10% optical contrast due to efficient absorption of visible light. Scale bar: 5 μm.

Adopting this “wet transfer” technique for exfoliated samples meant one could no longer exfoliate directly onto SiO_2. Instead, a silicon chip is spin coated with a water soluble layer of polyvinyl alcohol (PVA) and then a layer of PMMA. The thickness of the PMMA is tuned to get the favorable optical contrast qualities of the 300 nm SiO_2. 2D materials are then exfoliated onto the PMMA. With a sample identified, the chip is floated in DI water, dissolving the PVA, causing the chip to sink and the PMMA layer with the 2D material on top of it to float on the water’s surface. The floating polymer is then scooped up by a glass slide with a hole in it. This so-called “stamp” is attached to micromanipulators and lined up underneath an optical microscope objective (Figure 2.9a). The stamp is lowered down onto a SiO_2 substrate which would have another 2D material on it and which is affixed to a heater stage. The two materials, one on the stamp and one on the substrate, can be positioned with micrometer accuracy while the stamp is lowered into contact. Once contact is made, heating up the bottom substrate causes the PMMA to stick and release from the stamp. PMMA is then dissolved in acetone and the heterostructure is ready either for another transfer or for device fabrication and measurement[8].

This wet-transfer technique, due to water floating and PMMA dissolving, leaves polymer residues between each 2D layer. The more layers in the heterostructure, the more contamination, leading to a roadblock for complex, high performing 2D heterostructure devices. Researchers at Manchester University recently modified this technique, figuring out how to disconnect the 2D crystals off the PMMA stamp without melting the PMMA, thereby avoiding the solvent clean step[36, 37]. However, for utmost cleanliness, it is desirable to create stacks of materials that never came in contact with any polymer or solvents. This ensures clean interfaces and minimal distance between layers allowing for maximum interlayer coupling effects.

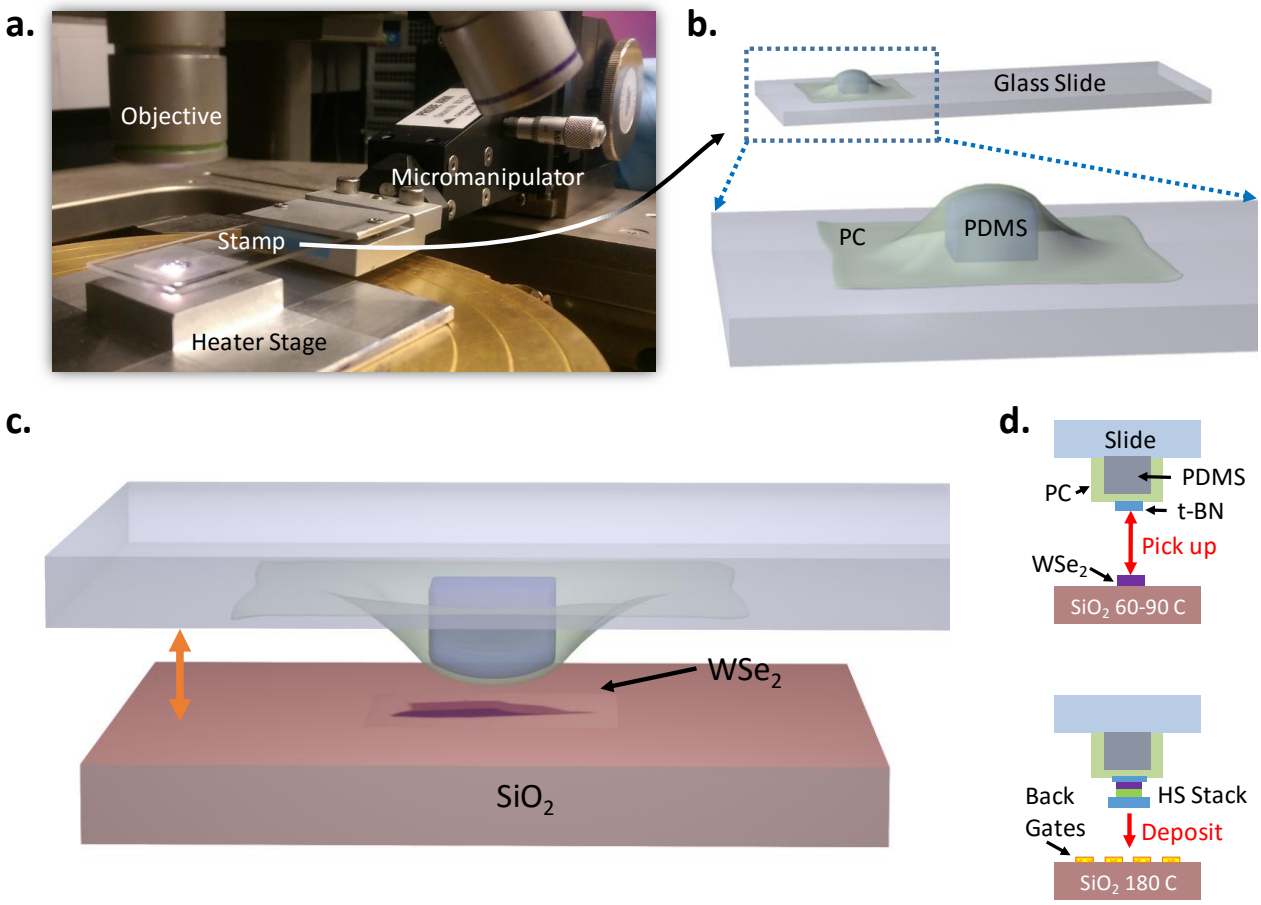

Figure 2.9. **Monolayer Transfer Techniques. a**, Photograph of transparent stamp micropositioning transfer setup. **b,** Illustration of glass slide stamp with PC van der Waals polymer draped over flexible PDMS substrate. **c,** Illustration showing the stamp being brought down onto a WSe_2 monolayer that it will easily pick up off of SiO_2. **d,** Process illustration for creating complex 2D heterostructure using PC stamp method ending with depositing the HS onto metallic back-gates.

In response, new Van der Waals or "dry transfer" techniques were developed[32, 71]. These techniques rely on polymers which have a stronger Van der Waals interaction to the 2D materials than does SiO_2. This allows 2D materials exfoliated on regular 300 nm SiO_2 to be directly pulled

off onto a stamp, with positioning techniques similar to the wet transfer method. The first generation dry transfer method used Polypropylene carbonate (PPC) as the Van der Waals layer. The preferred stamp in this process was a regular glass slide with a small piece of the gel polymer PDMS stuck on it and then thin PPC layer draped over the PDMS (Figure 2.9 a and b) [32]. The PDMS is flexible and transparent allowing the stamp to easily be push down and conform to 2D layers on SiO_2 (Figure 2.9c). Once one sample is picked up, it can either be melted down onto a target sample, or a second sample can be immediately picked up. This allows for arbitrarily complex heterostructures to be fabricated where the interfaces between the 2D layers are free of contaminates. Figure 2.9d illustrates the procedure for creating tunneling-BN/WSe_2/$MoSe_2$/BN dielectric heterostructures and depositing them on pre-defined metallic back gates. This procedure is used to create the HS 2D LED discussed in Chapter 4. Only the top-most layer is exposed to solvents when the stack is finally melted off the stamp and the PPC is dissolved in chloroform. This layer is usually an encapsulating layer of BN and not the active region of the device. The PPC dry transfer technique proved itself when it enabled a BN-graphene-BN sandwich device with one-dimensional metal contacts to the edge of the graphene showing mobility approaching the phonon-scattering limit[32].

But the PPC technique is not perfect. Most importantly, it has a hard time starting with thin layers of 2D materials, whether its monolayer graphene or TMD or a thin tunneling BN layer. One usually has to start with a BN layer that is several nm thick. This limits the type of devices that can be fabricated and means all heterostructures end up encapsulated in an insulating layer, which may not be favorable for certain experiments.

Thankfully a new dry transfer process was developed which simply replaced PPC with polycarbonate (PC). PC has a much stronger Van der Waals interaction with 2D materials. It's

able to pick up any 2D material of any thickness at even lower temperatures than PPC. The technique is otherwise the same. A glass-slide-PDMS stamp is covered with a layer of PC and multiple pickups and transfers are performed in a microscope (Figure 2.9d). When the stack is finished, it is melted onto an SiO_2 chip at ~170^0C[71]. This process seems to be the most versatile transfer technique to date, allowing for any vertical arrangement of any combination of 2D materials.

The research present in this thesis was very much dictated by the development of the above exfoliation and transfer techniques which sequentially opened up more and more heterostructure possibilities. In Chapter 3, freshly exfoliated samples are directly fabricated into devices on SiO2 via EBL techniques and their optoelectronics studied. In Chapter 4, the PVA wet transfer technique was used to make WSe_2-BN heterostructures with metallic back-gates enabling later p-n junctions. And in Chapter 4, the PC dry transfer technique had become the standard and enabled a complex device stack of BN-WSe_2-$MoSe_2$-BN, resulting in an LED and photodetector based around the interlayer exciton in the WSe_2-$MoSe_2$ HS.

2.7 SUMMARY

It is clear that TMDs offer a playground for studying exciton physics in truly monolayer and atomically sharp heterostructure systems, developing ultra-thin optical devices, and exploring the new realm of coupled spin and valley physics. For the remainder of this thesis research, specific examples of these will be explore. Chapter 3 focuses on 2D exciton charging effects in monolayer $MoSe_2$. Chapter 4 presents the first LEDs made from WSe_2. And finally in Chapter 4, I present an LED based on the built-in $MoSe_2$-WSe_2 heterostructure p-n junction which sheds light on the optoelectronic properties of the interlayer exciton.

Chapter 3. CHARGED EXCITONS IN TWO DIMENSIONS

In this chapter the spectral features of excitons as they behave in two dimensions are described using monolayers of $MoSe_2$ as a case study. Specifically, photoluminescence (PL) spectroscopy of field effect transistor devices is used to identify which spectral features correspond to neutral and charged excitons. Temperature dependence is always studied to investigate how these tightly bound quasiparticles persist up to room temperature. For more details and similar work, I refer the reader to references [12–14].

3.1 $MoSe_2$ Introduction

Above bandgap photo-excitation creates electrons and holes in the conduction and valence bands respectively. If the screening is weak enough the attractive Coulomb interaction between one electron and one hole creates a bound quasi-particle known as a neutral exciton (Xo) which has an energy structure similar to a neutral hydrogen atom. Excitons can further become charged by binding an additional electron (X-) or hole (X+) to form charged 3-body excitons (called trions) analogous to H– or H2+ respectively[72–74]. These exciton species are elementary quasi-particles describing the electronic response to optical excitation in solids and are integral to many optoelectronic applications from solar cells and light emitting diodes (LEDs)[75] to optical interconnects[76] and quantum logical devices[77, 78].

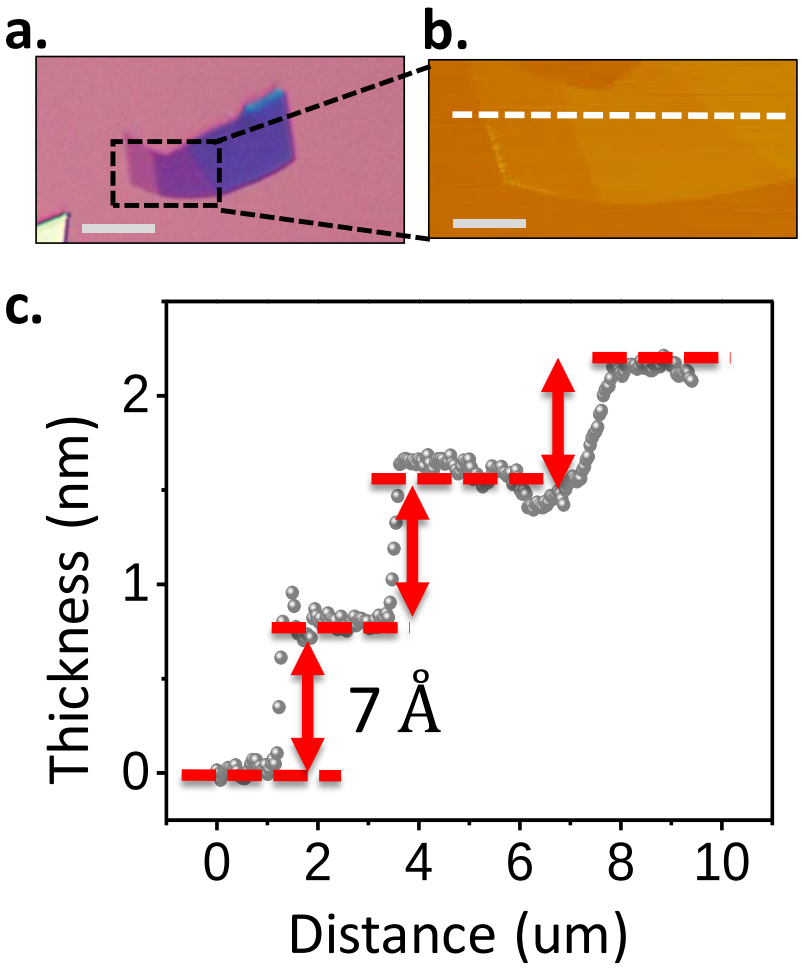

Figure 3.1. **Single Layer $MoSe_2$.** **a,** Optical micrograph of exfoliated $MoSe_2$ flake on 300nm SiO2. Scale bar: 5 µm. **b,** atomic force microscope (AFM) image of area highlighted in (a). Scale bar: 1 µm. **c,** AFM line scan along dashed line in (b).

Investigating and applying the physics of truly 2D excitons has thus been a long pursued goal, motivated centrally by the expectation that binding energies will be largely enhanced in the 2D limit[12, 25], providing stable states even at room temperature. This chapter presents the experimental observation and control of the truly 2D exciton physics by utilizing high quality monolayer molybdenum diselenide ($MoSe_2$). Initial TMD optics studies focused on MoS_2, including the demonstration of having a direct bandgap[11, 39], high mobility electronics[26],

optical generation of valley polarization[20, 21, 56], and electrical control of Berry phase properties[58]. However, the crystal quality of MoS_2 is poor and therefore the linewidths of PL features are broad making it difficult to resolve the multiple underlying excitons states that could possibly be making up the spectrum.

Using a back-gated field effect transistor (FET) device, I demonstrate the reversible electrostatic tunability of the exciton charging effects from positive (X^+) to neutral (X^o) and to negative (X^-). A large trion binding energy of 30 meV with a narrow emission linewidth of 5 meV is observed. These narrow, well separated features have temperature dependence of typical 2D excitons and exist at high temperature suggesting remarkable stability. Interestingly, the binding energies of X^+ and X^- are similar implying that low energy electrons and holes in $MoSe_2$ have the same effective mass. This work demonstrates that monolayer $MoSe_2$ is a true 2D semiconductor opening the door for the investigation of phenomena such as exciton condensation[79–81] and the Fermi-edge singularity[82, 83], as well as for a new generation of optoelectronic devices such as LEDs and excitonic circuits[76].

3.2 Single Layer $MoSe_2$ and FET Device Transport

Mechanical exfoliation is used to obtain monolayer $MoSe_2$ on 300 nm SiO_2 on n+ doped Si and atomic force microscopy (AFM) to identify the layer thickness[10]. Figure 3.1 a and b show the optical micrograph and the corresponding AFM image of a representative sample. AFM data shows this sample to have a single layer stepwise staircase in which the monolayer thickness of ~0.7 nm is identified at each step [26] (Figure 3.1c).

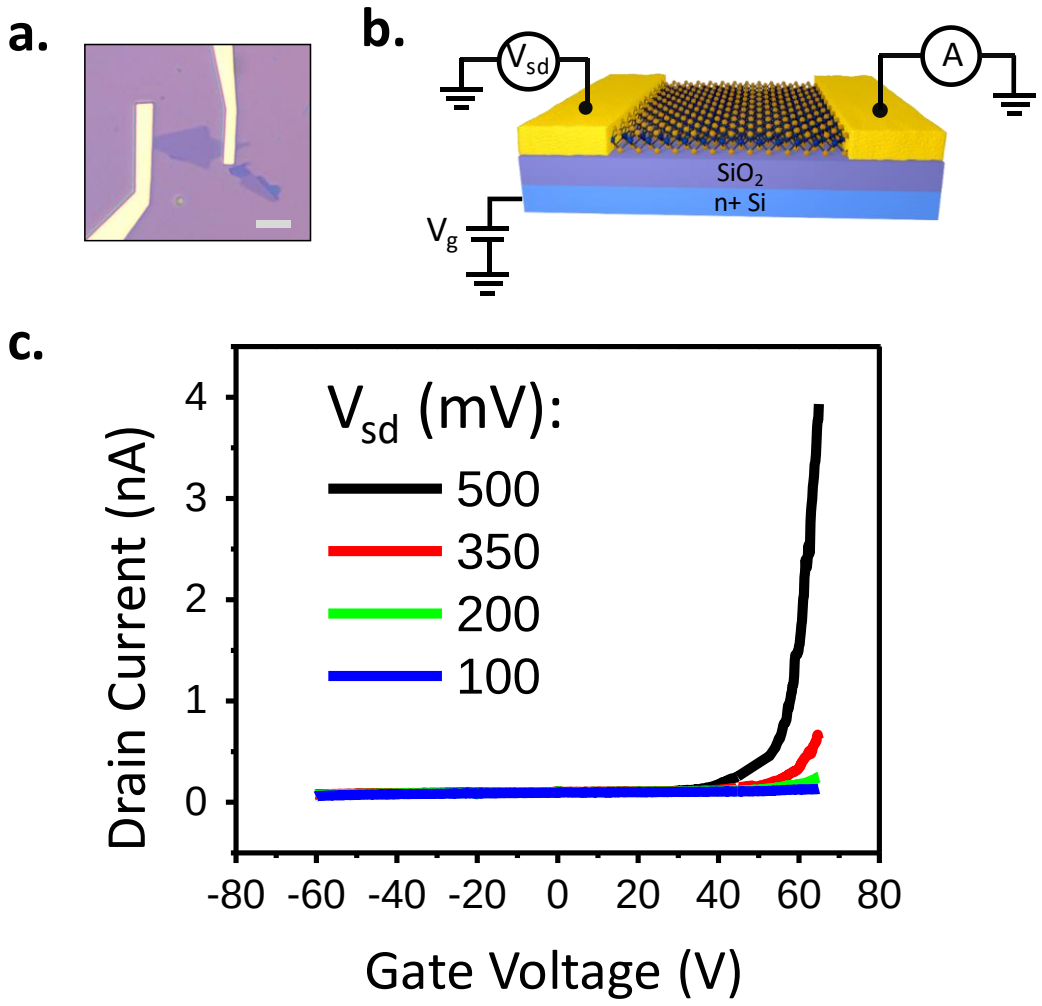

Figure 3.2. **$MoSe_2$ FET Device and Transport**. **a,** optical micrograph of $MoSe_2$ device. Scale bar: 5 µm. **b,** schematic of back-gated $MoSe_2$ device. **c,** Gate dependent transport characteristics of $MoSe_2$ FET device under various source-drain currents.

Standard electron beam lithography (EBL) is used to fabricate monolayer FETs with 6/60 nm V/Au evaporation deposited contacts (Figure 3.2a). With the contacts simply grounded, the n+ Si functions as a back gate (V_g) providing uniform electrostatic doping in the $MoSe_2$. And a source-drain bias (V_{sd}) can be applied to measure channel current (Figure 3.2b). All measured devices in this study show n-doped transport characteristics (Figure 3.2c).

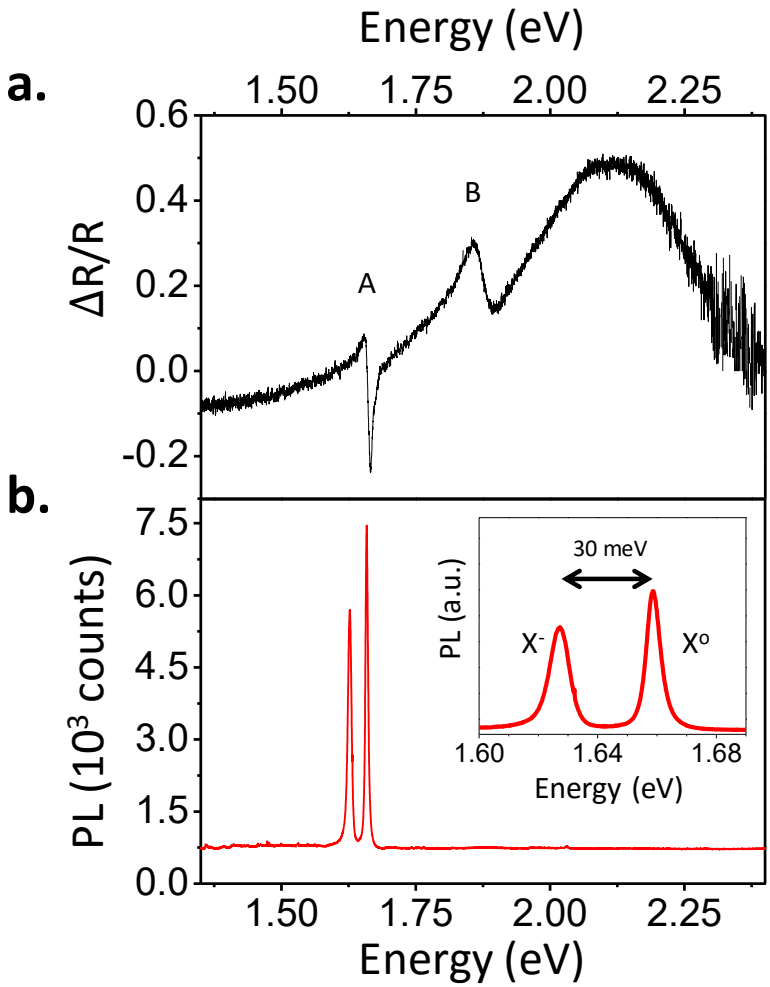

Figure 3.3. **Low Temperature Reflectance and PL Spectra**. **a,** Differential reflectance shows A and B excitons. **b,** Photoluminescence (PL) excited by 2.33 eV laser shows neutral exciton (X^o) and the lower energy charged exciton (X^-). PL from the B exciton has not been observed. Inset: PL of the exciton peaks. The X^- shows a binding energy of about 30 meV.

3.1 Spectral Features

The excitonic features of $MoSe_2$ are investigated by differential reflectance and micro-photoluminescence (μ-PL) measurements. Figure 3.3 shows the results from an unpatterned

$MoSe_2$ sample, S1. At 20 K, I observe two main features associated with the A and B excitons in the differential reflection spectrum[11, 20, 39, 84–86] (Figure 3.3a). As mentioned previously, the presence of A and B excitons is attributed to spin-orbit coupling induced valence band splitting in bulk[85]. The observed energy difference of ~200 meV agrees well with the calculated splitting of 180 meV in $MoSe_2$ monolayers.

With the same sample under 2.33 eV laser excitation, the PL spectrum does not show a measurable feature which can be attributed to the B exciton, likely since it is not the lowest energy transition. Instead, I observe two pronounced peaks at 1.659 and 1.627 eV in the vicinity of the A exciton (Figure 3.3b). It's important to note that the PL spectrum lacks the broad low energy peak observed in MoS_2 which has been attributed to defect-related, trapped exciton states[11, 20, 39, 86].

The striking spectral features demonstrate the high quality of my $MoSe_2$ samples and represents the first evidence for monolayer $MoSe_2$ being a direct bandgap semiconductor where the two distinct transitions are excitons. The higher energy emission at 1.659 eV is the neutral exciton, X^o, and as is proven below the lower energy peak is a trion[74]. All measured unpatterned samples show a charging energy, which is the energy difference between trion and X^o, of ~30 meV (Figure 3.3b inset). This is more than twice typical values reported in GaAs quantum wells[74, 87, 88] and similar to a recent observation in MoS_2[20]. In unpatterned samples, the trion is assumed to be X^- based off the n-doped transport and gate dependence behavior of all devices as described below in sections 3.4:More Gate Dependence.

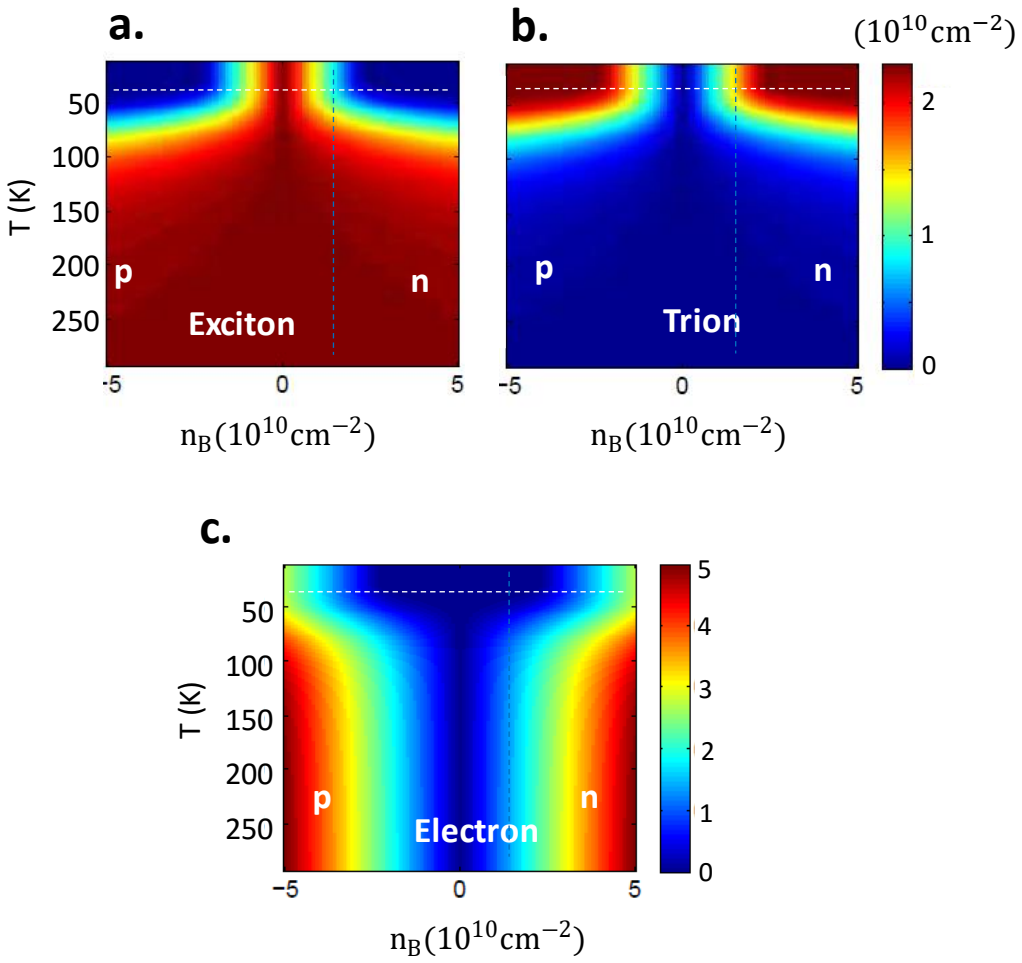

Figure 3.4. **Mass Action Model Plots**. Calculated densities of **a**, exciton, **b**, trion and **c**, electron 2D $MoSe_2$ as a function of background electron density and temperature with a fixed amount of absorbed photons of 3.2×10^{10} cm^{-2} during exciton life time. The white and blue lines correspond to the experimental data in the main text for gate and temperature dependence respectively.

3.2 Mass Action Model

Before we can understand how the different exciton states are filled and modulated by gate dependence and determine the relative intensity of their PL signals, we must adopt a steady state (dynamical equilibrium) mass action model of all the particles in our system. Here, for simplicity,

we consider the electron-trion, X^-, and assume that the free hole in the system is negligible. We denote n_X, n_{X^-}, and n_e for the concentration of X^o, X^-, and free electrons. $n_P \equiv n_X + n_{X^-}$ denotes the number of photoexcited electrons, and $n_B \equiv n_e + n_{X^-}$ denotes the background electrons (doping level) before light excitation. n_B and n_P are the initial conditions controlled by gate voltage and laser intensity, while n_X, n_{X^-}, and n_e are steady state variables.

To establish the relationship between these quantities we first write the reaction rate equation for trion formation, $X^o + e^- \rightarrow X^-$. From the law of mass action with trions we have[89–91]:

$$\frac{n_X n_e}{n_{X^-}} = A\, k_B T \exp(-\frac{E_T}{k_B T})$$

Here T is the temperature, k_B is Boltzmann constant, E_T is the trion binding energy and $A = \frac{4M_{X^o} m_e}{\pi\hbar^2 M_{X^-}} = 6.18 \times 10^{11} \frac{1}{\text{cm}^2\,\text{meV}}$ in $MoSe_2$ in which $M_{X^o} = m_e + m_h$ and $M_{X^-} = 2m_e + m_h$ are the exciton and trion effective masses respectively. Next, from charge conservation we obtain:

$$n_e + n_X + 2n_{X^-} = n_P + n_B.$$

Solving the above equations gives

$$n_{X^-} = \frac{n_P + n_B + n_A - \sqrt{(n_P + n_B + n_A)^2 - 4n_P n_B}}{2}$$

Here, $n_A = A\, k_B T \exp(-\frac{E_T}{k_B T})$. By plotting these quantities as a function of T and n_B, we are able to model the full range of our experimental gate-dependence data (Figure 3.4). We note that the entire picture and the values we have here for electron-trion can be applied directly to the hole-trion thanks to the same effective mass of electron and hole in our massive Dirac Fermion system. Therefore this has also addressed the gate dependent PL data in the hole-domain, which is covered by the negative values of n_B in Figure 3.4.

3.3 GATE DEPENDENCE

With a mass action model, we are now in the position to confirm the previously assumed exciton species identification and charging effects by performing gate dependent PL measurements. Here, the excitation laser is at 1.73 eV for better resonance with the luminescent states. Figure 3.5a shows a color map of the PL spectrum of device D1 at 30 K as a function of V_g in which I clearly observe four spectral features whose intensities strongly depend on V_g. Near zero V_g the spectrum shows a broad low energy feature around 1.57 eV and a narrow high energy peak at 1.647 eV. With large V_g of either sign, these peaks disappear and a single emission peak dominates the spectrum. Both peaks (at negative or positive V_g) have similar energies and intensities with the latter increasing with the magnitude of V_g.

This observed gate dependence confirms the assignment of states as labeled in Figure 7a. Since the broad low energy peak does not show up in unpatterned samples before FET fabrication, I attribute it to exciton states trapped to impurities (X^I)[11, 20, 39, 86] which in comparison to the unpatterned sample S1, seem to be introduced during EBL processing. The sharp peak at 1.647 eV is the X^o, slightly red-shifted compared to unpatterned samples. From the gate dependence, I identify the peaks near 1.627 eV as the X^- and X^+ trions when V_g is largely positive and negative respectively. Remarkably, these two distinct quasi-particles (X^+ and X^-) exhibit a nearly identical binding energy. The difference is within 1.5 meV over the whole applied V_g range. Since the binding energy of a trion is dependent on its effective mass, this observation implies that the electron and hole have approximately the same effective mass.

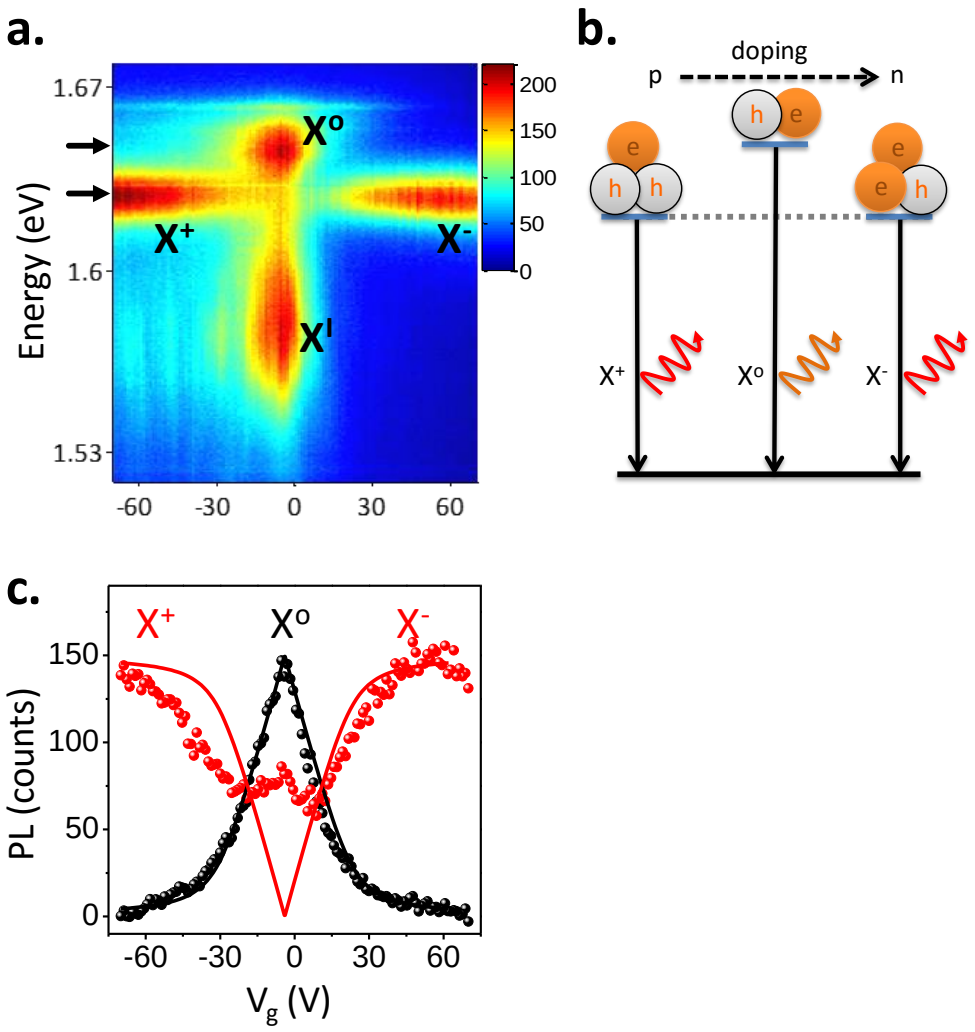

Figure 3.5. **Electrostatic control of Exciton Charge**. **a,** $MoSe_2$ photoluminescence (color scale in counts) is plotted as a function of back-gate voltage. Near zero doping, I observe mostly neutral and impurity-trapped excitons. With large electron (hole) doping, negatively (positively) charged excitons dominate the spectrum. **b,** Illustration of the gate dependent trion and exciton quasi-particles and transitions. **c,** trion and exciton peak intensity vs. gate voltage at dashed arrows in (a). Solid lines are fits based on the mass action model.

The gate dependent measurements unambiguously demonstrate the electrical control of exciton species in a truly 2D semiconductor, as illustrated in Figure 3.5b. The conversion from X^o to trion can be represented as $e(h) + X^o \rightarrow X^- (X^+)$, where e and h represent an electron or a hole respectively. By setting V_g to be negative, the sample is p-doped, favoring excitons to form lower energy bound complexes with free holes. As V_g decreases, more holes are injected into the sample and all X^o turn into X^+ to form a positively charged hole-trion gas. With positive V_g a similar situation occurs with free electrons to form an electron-trion gas. In the following, I show that a standard mass action model can be used to describe the conversion dynamics.

Figure 3.5c shows the extracted X^o (black) and trion (red) peak intensity as a function of V_g where I have adjusted the negative V_g data due to background signal. The plot shows that the maximum X^o intensity is about equal to the saturated trion PL when X^o vanishes. This observation indicates conservation of the total number of X^o and trion in the applied voltage range and similar radiative decay rates for both quasi-particles. Thus the PL intensity represents the amount of the corresponding exciton species. Since the dynamic equilibrium of free electrons, holes, and excitons are governed by the rate equation and law of mass action[88], I calculate the gate dependent X^o and trion abundance, shown by the solid lines in Figure 7c, which agrees with the data.

In the simulation, I first fit the X^o curve to obtain my two free parameters: the maximum background electron concentration $n_{\mathrm{B}}^{\max} = 3.6 \times 10^{10}\mathrm{cm}^{-2}$ when the trion intensity saturates and the photo-excited electron concentration $n_{\mathrm{P}} = 1.5 \times 10^{10}\mathrm{cm}^{-2}$. I then fit the trion gate dependence with these parameters held fixed. The deviation in the trion experimental data from the calculated curve near zero V_g is artificial due to the mutual background from X^o and X^I. I note that this inferred electron concentration is much smaller than the product of the gate capacitance and V_g.

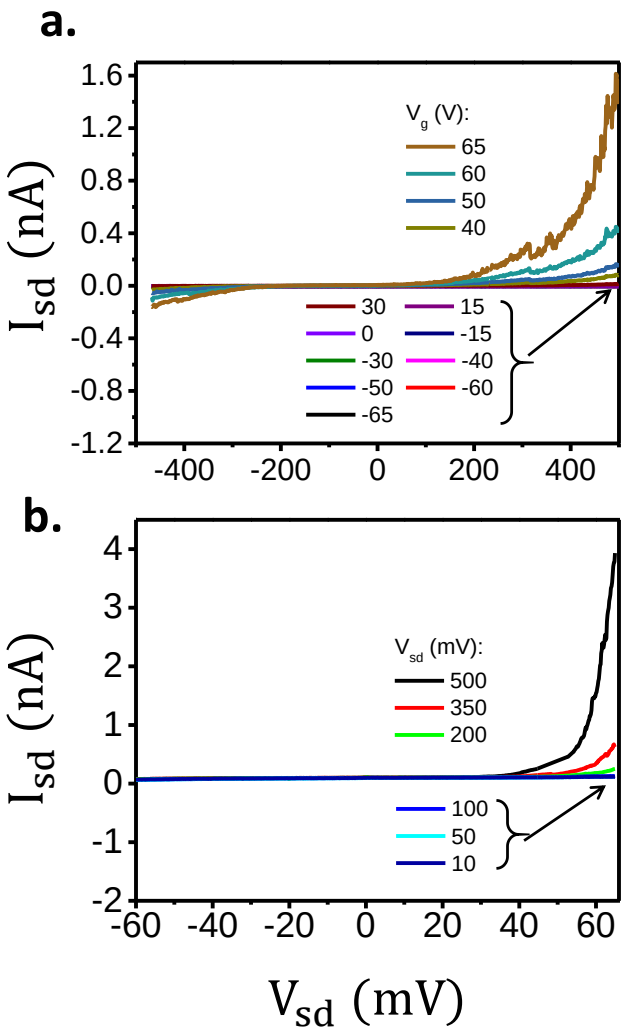

Figure 3.6. **Low Temperature transport**. **a,** Source-drain bias vs. current for various gate voltages. **b.** Gate voltage vs. current for various source-drain biases.

This discrepancy can be attributed to the large contact resistance of this type of FET design, which prevents the carrier concentration from reaching equilibrium on the experimental time scale at 30 K. The gate dependent presented above was measured at zero source-drain bias. Figure 3.6a illustrates that at any gate voltage, there is miniscule conductance for this experimental condition. Specifically, we find the resistance near zero bias to be on the order of 100 GΩ for all gate voltages. Only with appreciable biases above 100 mV do devices show significant conduction. With this in

mind, it will be interesting to investigate the gate dependent PL with Ohmic metal contacts. With the recent advancements in recent low resistance contacts described in section 2.2: 2D Semiconducting Properties and Devices, it would be prudent to recheck this phenomenon today.

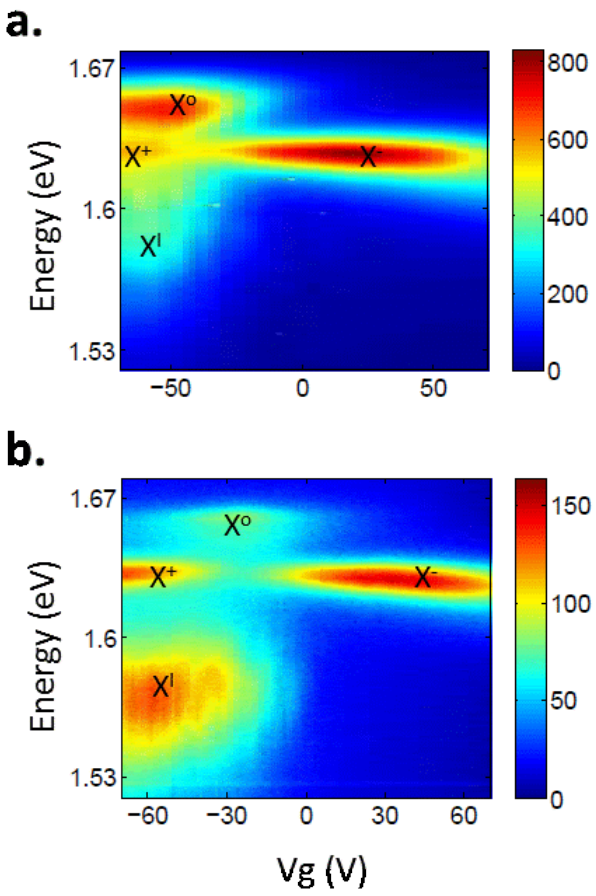

Figure 3.7. **More Gate Dependence**. **a,** Device D2 under 1.96 eV laser excitation. **b,** Device D3 under 1.73 eV laser excitation. Both show nonzero electron doping at back gate value of $V_g = 0$.

3.4 More Gate Dependence

Previously, we've assume that trions observed in unpatterned samples (no device fabrication after mechanical exfoliation) are negatively charged electron-trions, or X^-. Here we provide supporting

evidence of this by presenting gate dependence of other additional $MoSe_2$ FET devices. In Figure 3.7a and b we see, as with all $MoSe_2$ devices investigated during this study, a negative gate voltage is required in order to maximize the X^o. Since a maximized X^o corresponds to a minimized free carrier density (see section 3.2:Mass Action Model), this gate dependence supports the fact that all freshly exfoliated samples are originally n-doped. This is also consistent with observations[20, 26] in MoS_2, suggesting a similar defect mechanism is present in both cases.

3.5 Temperature Dependence of $MoSe_2$ Photoluminescence

The observed exciton states also show fine features consistent with 2D excitons, such as temperature dependent line shape, peak energy, and relative weight of X^o and trion, which further supports the excitonic nature of this monolayer system.

Figure 3.8a shows the evolution of X^- and X^o (normalized PL) as a function of temperature in an unpatterned sample, S2, under 1.96 eV laser excitation. At low temperatures, I again observe a binding energy of 30 meV. As the temperature rises I see the X^- signal drop significantly at about 55 K which I attribute to electrons escaping their bound trion state due to thermal fluctuations.

Figure 3.8b is the zoom-in plot at 15K where I observe slightly different line shapes for X^- and X^o. The X^o peak is symmetric showing homogenous thermal broadening effects and is well fit by a hyperbolic secant function which yields a full width half maximum of 5 meV[88, 91]. However, the X^- peak shows a slightly asymmetric profile with a long low-energy tail consistent with electron recoil effects[88]: The recombination of a X^- with momentum k will emit a photon and leave a free electron with the same momentum k due to momentum conservation. From energy conservation, the emitted photon has an energy $\hbar\omega = \hbar\omega_o - \frac{\hbar k^2}{2m_e^{*2}}\frac{M_{X^o}}{M_{X^-}}$, where $\hbar\omega_o$ is the energy

of trions with $k = 0$, and M_{X^o} and M_{X^-} are the X^o and X^- effective masses, respectively. The lineshape of trion PL will thus be the convolution of a symmetric peak function (hyperbolic secant) and an exponential low-energy tail function (See Section 3.6: Trion Recoil Effects for me details on recoil effects). When the temperature is above 70K, I find homogenous broadening dominates over electron recoil and the PL spectrum is fit well by two hyperbolic secant functions (Figure 3.8c)

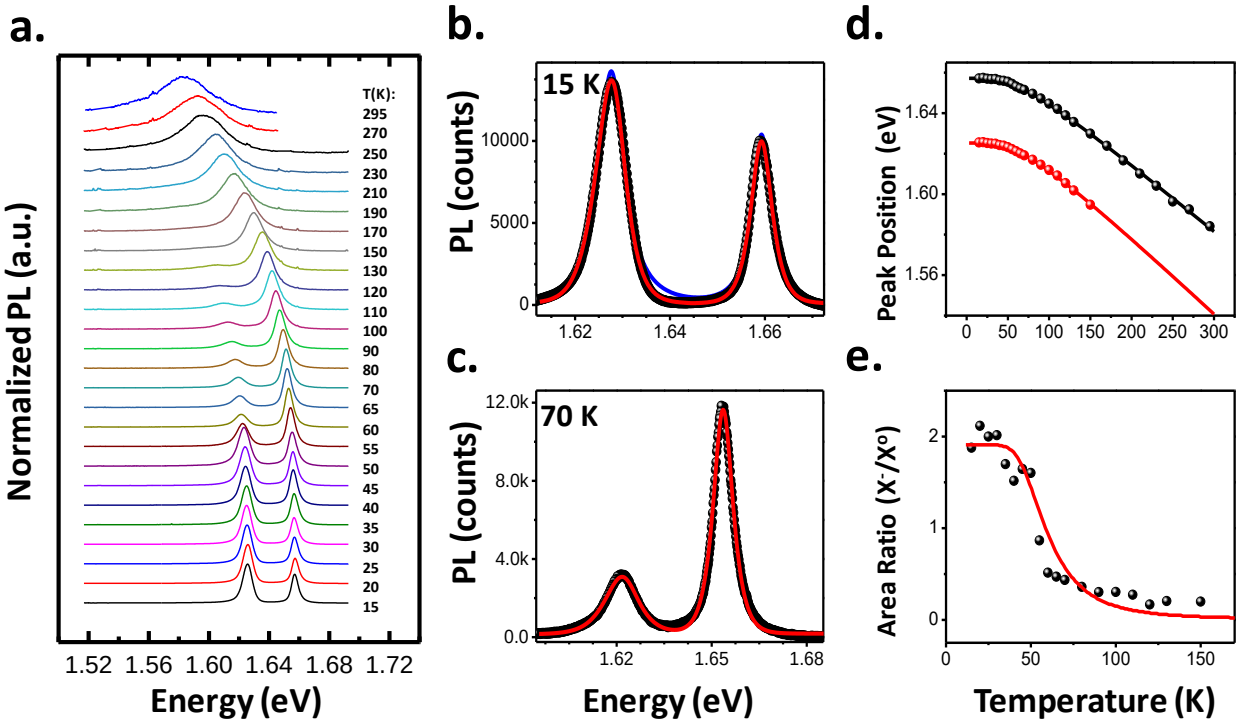

Figure 3.8. **Temperature Dependence of PL Spectrum**. **a,** Normalized photoluminescence of monolayer $MoSe_2$ vs. temperature. **b,** Line shape fitting at 15 K. Black is data. Red and blue curves are fits with and without considering the electron-recoil effect. **c,** Data and fit at 70 K using two symmetric peaks. **d,** Neutral exciton (black)

and trion (red) peak position vs. temperature with fits (solid lines). **e,** Integrated area ratio of trion:exciton vs. temperature with mass action model fitting (red).

From the fits I extract the X- and Xo peak position (Figure 3.8d) and the ratio of the integrated intensity of the X- to the Xo (

Figure 3.8e) where I do not present trion data above 150 K because it becomes negligible. I find that the peak positions are fit well (solid line in Figure 7d) using a standard semiconductor bandgap dependence[92] of $E_{\mathrm{g}}(T) = E_{\mathrm{g}}(0) - S\langle\hbar\omega\rangle\left[\coth\left(\frac{\langle\hbar\omega\rangle}{2kT} - 1\right)\right]$ where $E_{\mathrm{g}}(0)$ is the ground state transition energy at 0 K, S is a dimensionless coupling constant, and $\langle\hbar\omega\rangle$ is an average phonon energy. From the fits I extract for Xo (X-) the $E_{\mathrm{g}} = 1.657$ (1.625) eV, $S = 1.96$ (2.24) and $\langle\hbar\omega\rangle = 15$ meV for both. Applying my mass action model with a trion binding energy of 30 meV results in a good fit to the X-:Xo intensity ratio (solid line in

Figure 3.8e).

3.6 Trion Recoil Effects

Because of energy and momentum conservation, the radiative recombination of an electron- trion with center of mass wave vector **k** results in a conduction electron with wave vector **k** and a photon with energy $\hbar\omega = \hbar\omega_o + \frac{\hbar^2k^2}{2M_T} - \frac{\hbar^2k^2}{2m_e^*} = \hbar\omega_o - \frac{\hbar k^2}{2m_e^{*2}}\frac{M_X}{M_T}$, where $M_T = 2m_e^* + m_h^*$ is the trion mass, $M_X = m_e^* + m_h^*$ is the exciton mass, and $\hbar\omega_0$ is the energy of trion with **k** = 0. The photon emission rate is given by the optical matrix element $M(\mathbf{k})$ and trion distribution $f(\mathbf{k})$, which is

$$R(\omega) = \int d\mathbf{k}|M(\mathbf{k})|^2 f(\mathbf{k})\delta(\hbar\omega - \hbar\omega_0 + E(k))$$

where $E(k) \equiv \frac{\hbar k^2}{2m_e^{*2}} \frac{M_X}{M_T}$. In the low density limit, the distribution function $f(\mathbf{k})$ can be approximated by the Boltzmann distribution $f(\mathbf{k}) \propto \exp\left(-\frac{\hbar^2 k^2}{2M_T k_B T}\right)$. The optical matrix element $|M(\mathbf{k})|^2$ has already been numerically evaluated by Stébé *et al.*[93]. Although for the 2D case they only give results for $\sigma \equiv \frac{m_e^*}{m_h^*} =$ 0, 0.1, 0.2, and 0.3, we find those curves can all be well approximated by an exponentially decaying function $|M(\mathbf{k})|^2 = |M(\mathbf{0})|^2 e^{-27.3E(k)/E_0}$. With $E_0 \equiv 2(1+\sigma)|E_X^{3D}|$, and E_X^{3D} is the 3D exciton binding energy. We expect this equation applies for any $\sigma \in [0,1]$.

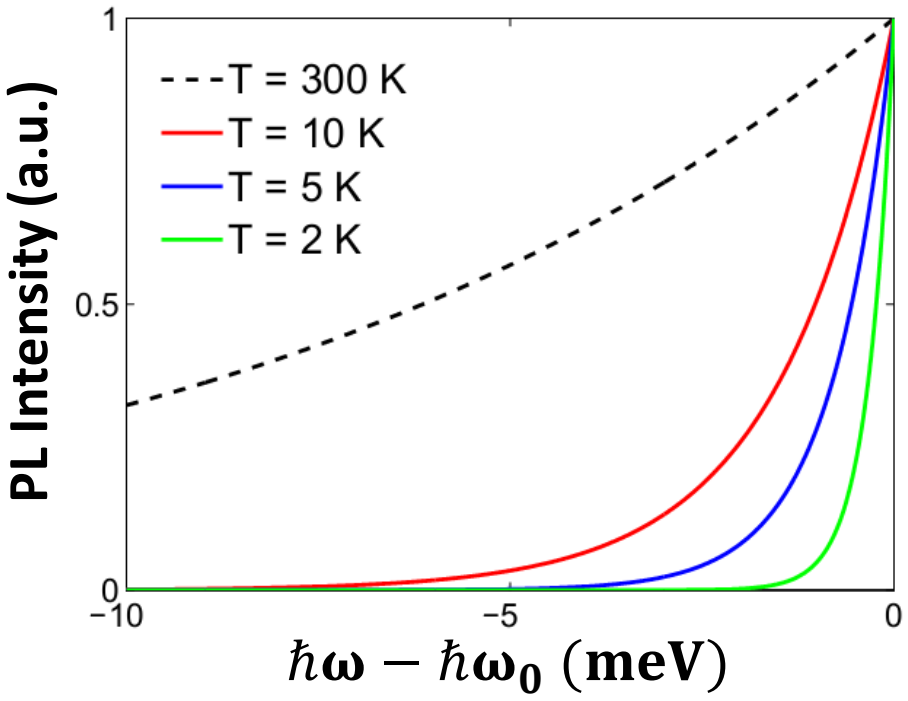

Figure 3.9. **Trion Recoil PL Line shape**. Electron recoil effects result in a temperature dependent exponential line shape on one side of the photoluminescence peaks of trions.

The photon emission rate as a function of ω is then

$$R(\omega) = \int d\mathbf{k}|M(\mathbf{k})|^2 f(\mathbf{k})\delta\left(\hbar\omega - \hbar\omega_0 + E(k)\right)$$
$$= R(\omega_0)\exp\left[-\left(\frac{27.3}{E_0} + \frac{m_e^*}{M_X}\frac{1}{k_B T}\right)(\hbar\omega_0 - \hbar\omega)\right]\Theta(\omega_0 - \omega)$$

Here Θ is the Heaviside step function. In the $MoSe_2$ system, $\sigma = 1$ and the 3D exciton binding energy is $E_X^{3D} = R_y^* = 50$ meV. We have plotted the line shape $R(\omega)$for several temperatures in Figure 3.9. Thus the trion line shape can be fit through convolution of the above contribution with a symmetric broadening effect.

3.7 Final Remarks

I have shown that monolayer $MoSe_2$ is a true 2D excitonic system which exhibits strong electrostatic tuning of exciton charging via a standard back-gated FET. The observed narrow, well separated spectral features are well within standard tunable Ti-Sapphire laser systems' range (Figure 3.10) and thus provide remarkable opportunities to selectively probe and control specific excitons using current continuous wave and ultrafast laser technologies. My results further demonstrate that high quality monolayer dichalcogenides can serve as a platform for investigating excitonic physics and photonic applications in the truly 2D limit with the potential to outperform quasi-2D systems. The results represent unique prospects for this burgeoning class of 2D materials in addition to the attention received for their valley physics.

This work was published in *Nature Communications*[12] and it is important to note that an independent observation of negatively charged excitons was made in monolayer MoS_2[14] as well as an investigation of the PL intensity of thin film $MoSe_2$ as a function of temperature[94].

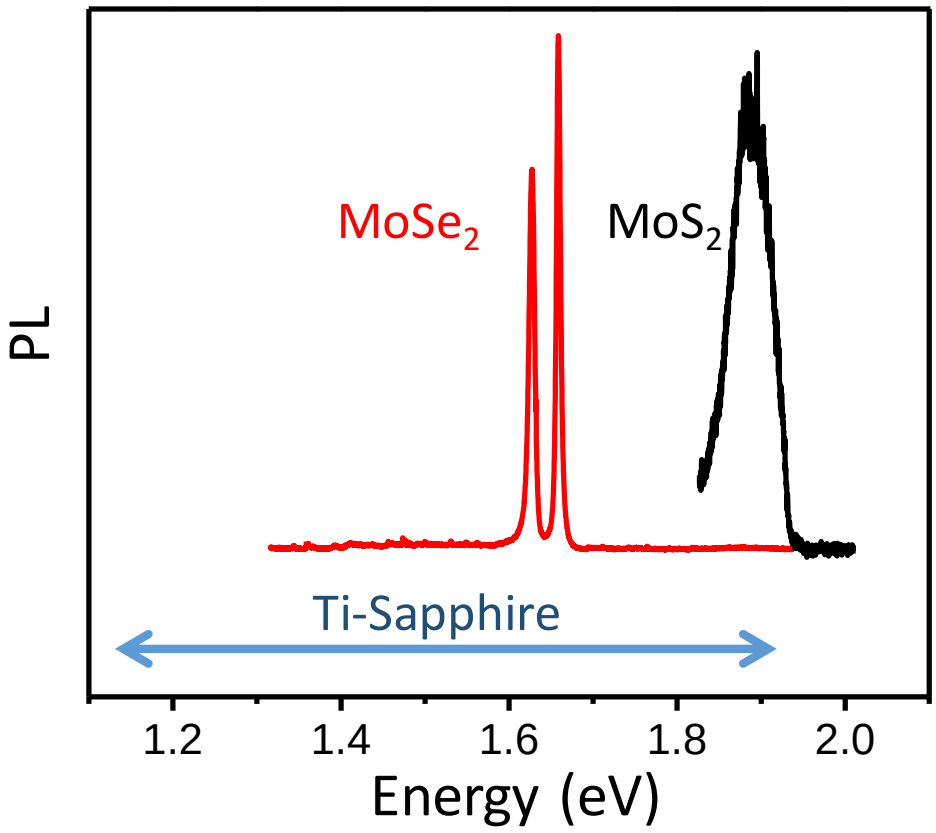

Figure 3.10. **Ti-Sapphire Laser Range and TMDs**. This figure shows the range of standard tunable Ti-Sapphire laser systems and how $MoSe_2$ excitons are well within the range while MoS_2 is on the edge.

Chapter 4. TWO-DIMENSIONAL LIGHT EMITTING DIODE

The development of novel light-emitting diodes (LEDs) with improved efficiency, spectral properties, compactness and integrability is important for lighting, displays, optical interconnects, logic and sensors applications [95–102]. In this chapter we present the first every LED to be created and demonstrated from all-2D materials. Beyond the technological breakthrough, we discuss the merit that these devices might offer in terms of being a valley optoelectronic component. For more discussion of 2D LEDs and valley devices we refer the reader to references [37, 48–50, 52].

4.1 WSe_2: The Quintessential Valley Polarized TMD?

The exciton and trion states of $MoSe_2$ have not been found to show significant circular polarization, hinting at a valley scattering mechanism in the system. Therefore, despite its well-defined excitons states, it does not stand as a favorable 2D valleytronic material. However, WSe_2 has been found to have the same exciton charging effects along with significant and interesting valley effects as discussed in Section 2.4: Unique Optics: Spin and Valley Physics. First, all the excitons present in the PL show substantial circular polarization. Second, and more interesting, the neutral exciton shows significant linear polarization no matter the axis of the incident linearly polarized excitation. Because linearly polarized light can be made up of a combination of left and right circularly polarized light, this result is attributed a valley coherence: The two valleys, K and –K, work together to maintain the initial polarization state of the incident light long enough for emission. This work is published in *Nature Physics*[13].

Valley coherence has exciting implications for new schemes of quantum computation. And with the already significant circular polarization of all the excitons, WSe_2 stands as the

quintessential valley material. This is why WSe_2 was chosen as the active emitter for the first 2D LED in hopes of realizing circularly polarized electroluminescent devices.

4.2 2D Electroluminescence Background

TMD Electroluminescence (EL) was first reported from monolayer MoS_2 FETs, occurring near the Schottky contact with a metal[47] or with highly doped silicon[29]. However, the efficiency and spectral quality was much lower than has been demonstrated for other nanoscale light emitters such as carbon nanotubes[101], for two reasons. First, efficient EL requires effective injection of both electrons and holes into the active region, which should therefore be within a p-n junction. Second, MoS_2 is known to have poorer optical quality than other group VIB TMDs, possibly due to impurities. It has been previously shown that, in contrast, monolayer WSe_2 has excellent optical properties[13, 103]. In this chapter, we demonstrate that using electrostatic doping to establish a p-n junction in a WSe_2 monolayer produces efficient and electrically tunable excitonic light-emitting diodes. These LEDs emit light with 1000 times smaller injection current and 10 times smaller spectral linewidth than in the MoS_2 studies. Further, the EL is clearly seen to be made up of neutral and charged excitons where the dominant luminescing species can be tuned by the source-drain bias applied across the diode. With this and the polarization properties of WSe_2, all the ingredients are present for realizing valley polarized light emission which could lead to novel applications such as valley-based photonics and computing.

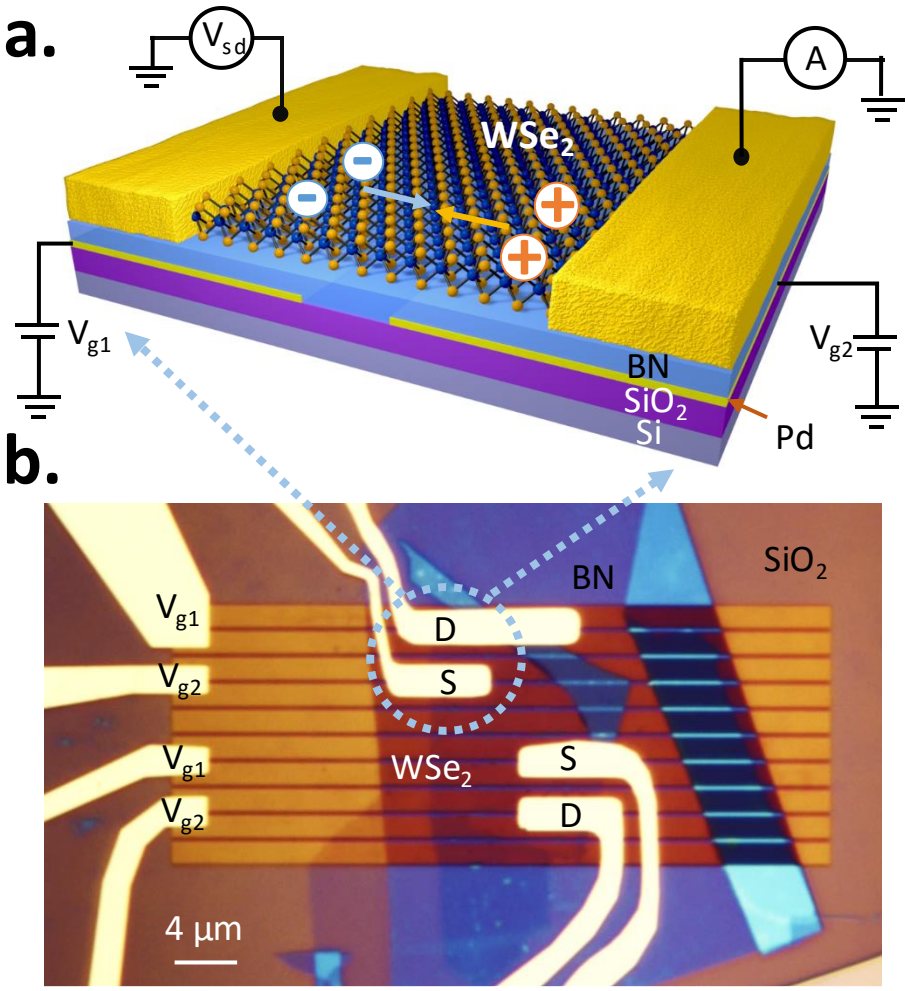

Figure 4.1. **WSe_2 p-n Junction Design**. **a,** Cartoon and **b**, optical micrograph of multiple monolayer WSe_2 p-n junction devices with palladium back gates (V_{g1} and V_{g2}) and source (S) and drain (D) contacts. The source-drain voltage (V_{sd}) is applied to one contact and the current (A) is read out of the other. During electroluminescence in the WSe_2, electrons (blue) and holes (yellow) move towards each other (arrows) and recombine. The back gates are separated from the WSe_2 by hexagonal boron nitride. The device sits on a layer of silicon dioxide on a silicon substrate.

4.3 WSe_2 LED Device Design

An optical image and a schematic of a device, made by a combination of electron-beam lithography and transfer of exfoliated sheets, are shown in

Figure 4.1 a and b. A monolayer WSe_2 sheet sits on a sheet of hexagonal boron nitride (BN), typically 10 nm thick, which acts both as a smooth, disorder-free substrate to minimize non-radiative energy relaxation pathways and as a high quality gate dielectric[20]. Applying voltages to the two 7 nm palladium gate electrodes beneath the BN can create two separate electrostatically doped regions in the WSe_2 separated by a 300 nm wide undoped strip. Gold/vanadium (60/6 nm) source and drain contacts are evaporated on top. Importantly, they overlap the gates in order to reduce the Schottky barriers for efficient current injection. For electrical transport measurements a dc bias V_{sd} is applied to one contact (the source) and the current I from the other (the drain) is measured by a virtual-earth current preamplifier (Figure 9b). The silicon substrate is grounded.

4.4 Device Transport

I start by showing that a p-n junction diode can be created electrostatically. First I set the gate voltages V_{g1} and V_{g2} to the same value. Figure 4.2a shows the current produced by a bias V = 0.5 V as the gate voltage $V_{g1} = V_{g2}$ is swept at 60 K. The current increases rapidly for gate voltages > +6.5 V (electron doping) and < -6.5 V (hole doping), demonstrating ambipolar operation. In the inset the red *I-V* curve, taken at $V_{g1} = V_{g2}$ = +8.0 V, is almost symmetric as expected for both gated regions being equally electron-doped. The nonlinearity near zero bias can be associated with the undoped gap between the gates and residual Schottky barriers at the contacts. In contrast, the blue *I-V* curve, taken with V_{g1} = +8.0 V and V_{g2} = -8.0 V, shows the strong rectification behavior expected for a p-n junction diode.

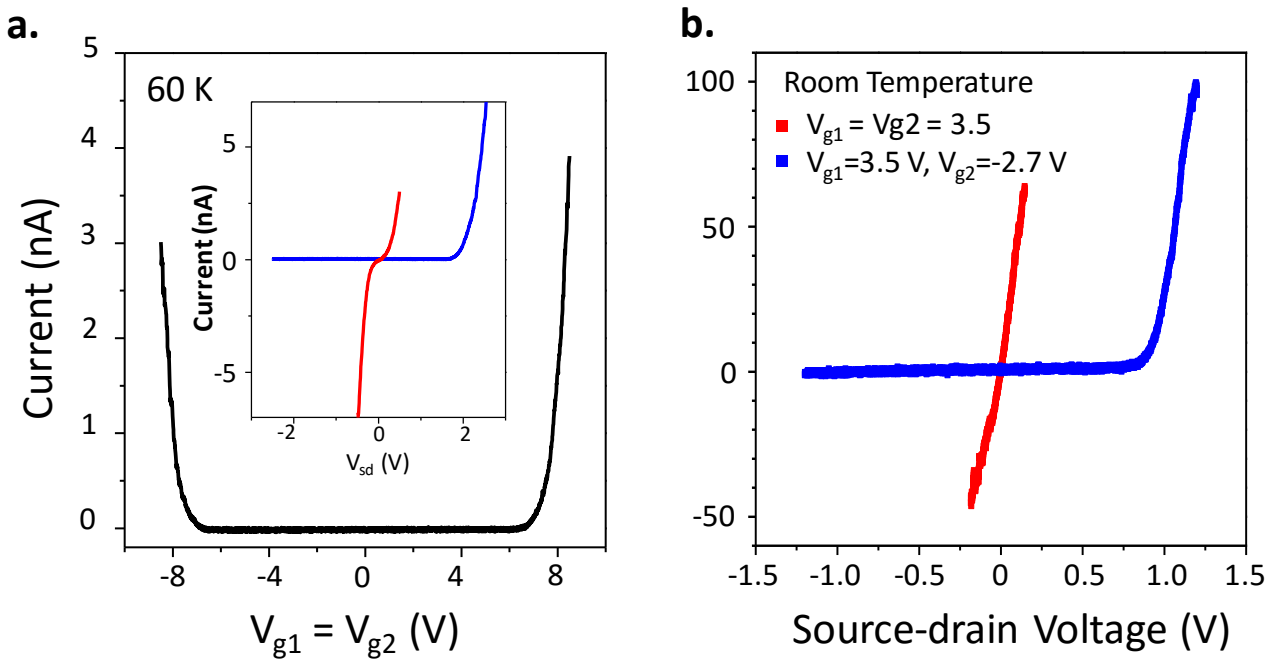

Figure 4.2. **Device Transport**. **a,** Main panel: variation of current with both bottom gate voltages set equal (V_{g1}=V_{g2}=V_g) for one junction at bias V_{sd} = 500 mV, showing ambipolar behavior. Inset: I-V_{sd} characteristics when the two gate voltages are set to equal (V_{g1}=V_{g2}=8 V, red) and opposite (V_{g1}=-8 V, V_{g2}=8 V, blue) values above the injection threshold. **b,** Room temperature electron doped conduction (black) and p-n junction forward bias (red)**.**

At room temperature we see the nonlinearity in the electron doped bias sweep disappear (Figure 4.2b, red curve) and forward bias conduction with about an order of magnitude increase in current (Figure 4.2b, blue curve).

4.5 Device Photoresponse

The p-n junction can be investigated in detail by scanning optical measurements[40, 43]. Figure 4.3a is a microscope image of a device and Figure 4.3b is a corresponding scanning

photocurrent image, measured with zero bias at 100 K using a 10 μW diffraction-limited 660 nm laser spot scanned over the sample. I see a large photocurrent signal localized between the gates, with a peak magnitude of 5 nA. Taking into account the 1% absorption of WSe_2 monolayers at 660 nm[104], the internal quantum efficiency reaches a maximum of about 5%. Such a photocurrent is the natural result of the junction functioning as a photodiode, with photogenerated carriers separated by a strong depletion field concentrated in the undoped gap. The sensitivity of the photodiode can be tuned over a wide range by varying the gate voltages and bias (not shown).

Figure 4.3c is a corresponding map of the integrated PL intensity, which illustrates the uniform optical quality of the WSe_2 sheet and shows that the luminescence is not substantially quenched by the underlying gates. More revealingly, Figure 4.3d shows a color map of the peak PL photon energy, exhibiting two distinct regions clearly correlated with the expected n-doped (blue) and p-doped (red) parts of the WSe_2 above the gates. The reason for this is made clear in Figure 4.3e, which shows PL spectra taken at three key positions. These spectral features are due to exciton charging effects as in $MoSe_2$, with the detailed origins having been subsequently described in WSe_2[13]. On the gate held at V_{g1} = +8.0 V (blue trace) the negatively charged X^- trion (two electrons and one hole) dominates, implying an excess of electrons. And on the other gate, held at V_{g2} = -8.0 V (red trace), the higher-energy positively charged X^+ trion (two holes and one electron) dominates, implying an excess of holes. In the gap between the gates (black trace) the neutral exciton X^o peak can also be seen, consistent with no doping in that region. Here the superimposed X^+ and X^- peaks likely come from the gated regions, since the laser spot is larger than the undoped gap.

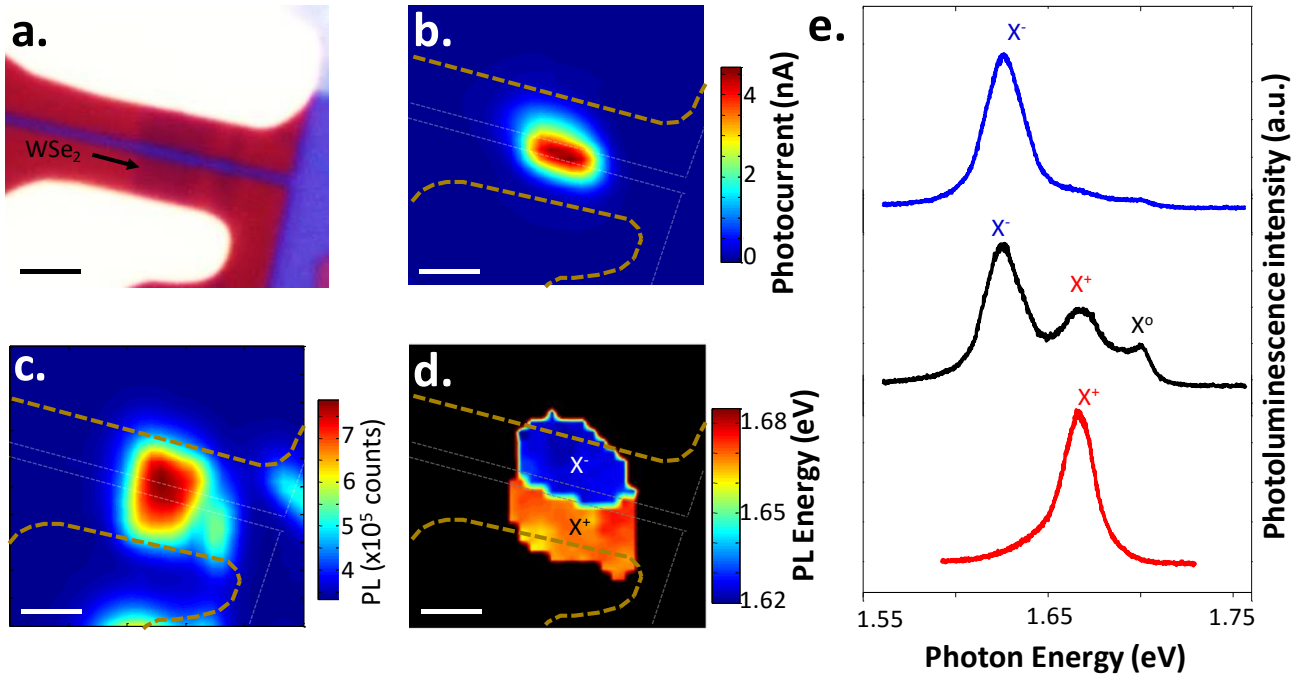

Figure 4.3. **Photoresponse of p-n Junction at 100 K**. **a,** Microscope image of a monolayer p-n junction device. The source and drain contacts are white, the two bottom gates are red, and the boron nitride is blue. **b**, Corresponding scanning photocurrent image showing pronounced photocurrent generation localized to the junction. The thicker dashed lines outline the source and drain contacts while the thinner dashed lines outline the back gates. **c**, Integrated photoluminescence map. **d**, Peak photoluminescence energy map showing p and n regions as a result of the different energies of oppositely charged excitons. X^- (X^+) represents the negatively (positively) charged exciton found in the n (p) region **e**, Top to bottom: selected spectra from n-doped region (blue), junction (black), and p-doped region (red) with negative, neutral (X^o), and positive exciton features indicated. All maps taken with V_{g1} = +8 V, V_{g2} = -8 V. Scale bars: 4 µm.

The sensitivity of the photodetector can be tuned over a wide range by changing the gate voltages and bias. Figure 4.4a shows scanning-laser (10 mW at 532 nm) reflection (top row) and corresponding photocurrent (PC, bottom row) images at different p-n junction fields as controlled by the opposite split-gate voltages. PC is generated at gate voltages as low as ±1 V. The location and shape of the PC spot, especially at high gate voltages, demonstrates that the p-n junction in the gap between the split gates governs the photoresponse, as opposed to Schottky barriers at the contacts. Sweeping the bias voltage can increase the sensitivity enabling a highly effective photodetector with miniscule voltages as small as ± 1 V on back gates and -500 mV bias while collection currents approaching 10 nA (red curve in Figure 4.4b). Such a sensitive photodetector is quite surprising considering we are working with a single molecular layer of material and has great promise for development of low-power, ambient energy optoelectronic devices.

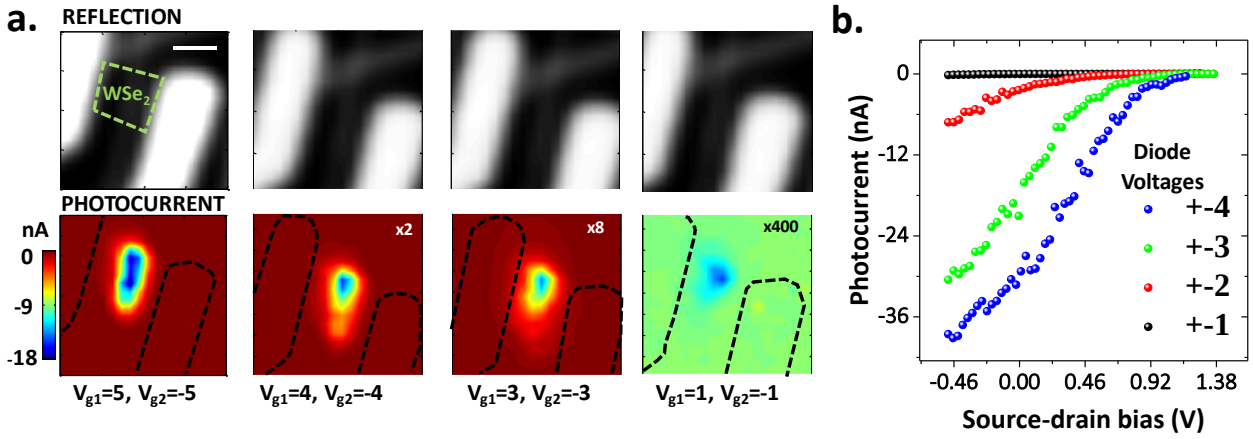

Figure 4.4. **Photocurrent Sensitivity**. **a,** Scanning-laser (10 mW at 532 nm) reflection (top row) and corresponding photocurrent (PC, bottom row) images at different p-n junction fields as controlled by the opposite split-gate voltages. **b,** Photocurrent as a function of bias showing high sensitivity with miniscule (≤ 1) voltages.

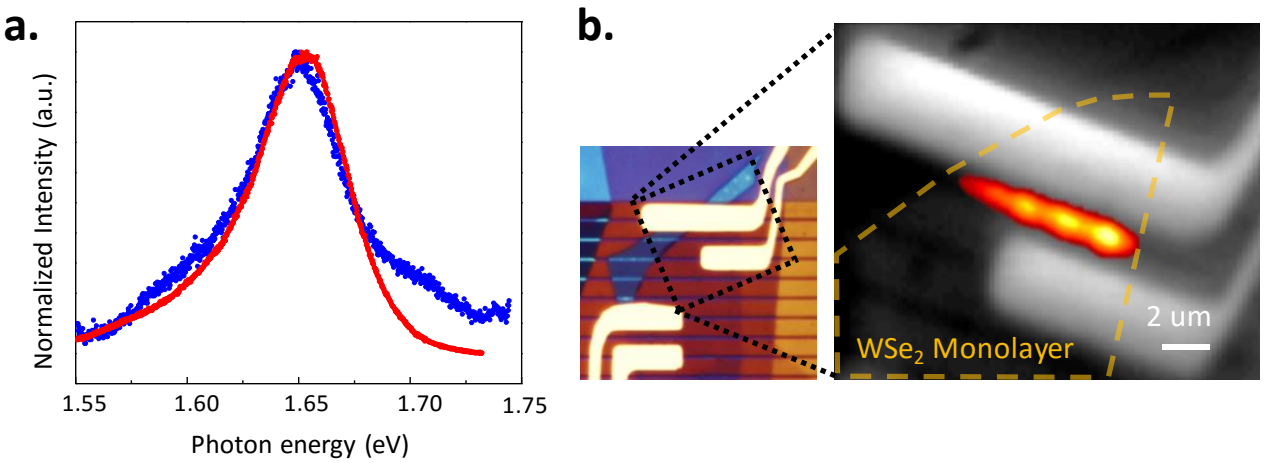

Figure 4.5. **Photoluminescence and Electroluminescence**. **a,** At 300 K, the EL spectrum (blue) generated by a current of 5 nA closely resembles the PL spectrum (red). **b**, EL image (red) superimposed on device image (grayscale). The orange dashed lines outline the WSe_2 monolayer. Scale bar: 2 µm.

4.6 Excitonic Electroluminescence

When the device is configured as a p-n junction ($V_{g1} = -V_{g2} = 8$ V), but not otherwise, I observe bright electroluminescence. Good spectra can be obtained even at room temperature with a current of 5 nA, as illustrated (blue) in Figure 4.5a. To understand the nature of the EL, I superimpose a normalized PL spectrum of undoped monolayer WSe_2 (red). It is known that the PL of WSe_2 is from the recombination of direct-gap excitons; thus the similarity between the EL and PL spectra implies that the injected electrons and holes form excitons before recombining radiatively. This is a natural consequence of the large exciton binding energy due to the strong Coulomb interaction in monolayer TMDs. Figure 4.5b shows an image of the total EL intensity (colored) superimposed on a simple white-light reflection image (grayscale). It is clear that the EL emanates from the entire length of the monolayer junction between the two gates.

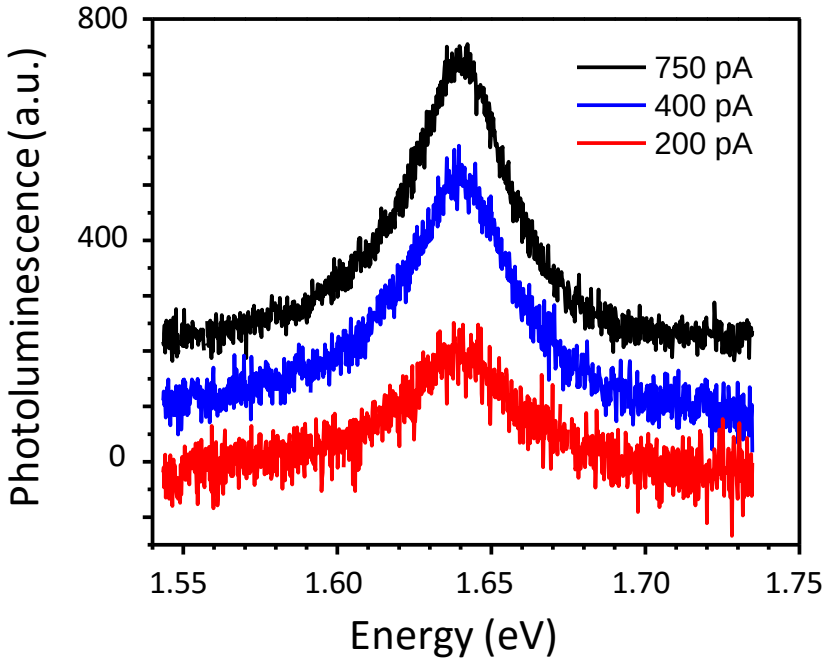

Figure 4.6. **Minimum Room Temperature EL Detection**. Background subtracted spectra of the electroluminescence (EL) at various injection currents.

The above current value for producing EL is three orders of magnitude smaller than in MoS_2 FETs[47, 105]. In fact, in our best device I can observe EL at an injection current at even lower currents at room temperature. Figure 4.6 shows the EL spectra at various bias currents at room temperate. An excitonic EL peak is clearly visible at currents as low as 200 pA.

4.7 Tuning Excitonic Emission

At low temperatures the EL spectrum develops interesting structure. Figure 4.7a shows a plot of EL intensity as a function of current and photon energy. There are three main spectral features: a narrow higher-energy peak (green arrow), a broad central peak (brown arrow), and a lower-energy peak (black arrow). The shapes and relative intensities of these features change with current. Their

origins can be deduced from a comparison with the PL, whose intensity is plotted in Figure 4.7b as a function of photon energy and common gate voltage $V_g=V_{g1}=V_{g2}$. Here I see the tuning of the dominant exciton species as the carrier density is changed by gating[13]. The PL feature which is strongest at $V_g = 0$ is due to X^0 recombination. It has a similar width to, and is at the same position (1.69 eV) as, the narrow EL peak, which I therefore identify as the X^0 emission. The dominant PL feature at $V_g > 0$, which shifts from 1.663 eV to 1.625 eV as V_g increases from 0 to +8 V, is due to X^- (of which there are multiple species[13]). The broad EL feature occurs in the same range of energies, implying that it is dominated by X^-. The dominant feature in the PL at $V_g < 0$ is due to X^+. This aligns with the high-energy shoulder (grey arrow) on the broad EL feature at about 1.670 eV. There is also a band of emission from impurity-bound excitons (X^I) in the PL which matches the lower-energy EL feature centered at 1.59 eV.

The finding that X^- dominates the EL in Figure 12a is consistent with the observation that X^- has much stronger PL than the other exciton species (Figure 4.7b). The shifts of the trion peaks in the PL with V_g imply that the trion binding energy depends on perpendicular electric field. Hence the fact that the width of the broad peak in the EL matches the full range of X^- energies in the PL is explained by the variation of the perpendicular electric field across the junction. On the other hand the X^0 peak shifts very little with V_g in the PL and hence is insensitive to field; thus the X^0 EL peak is also sharp. The X^0 EL linewidth is found to be as narrow as 5 meV, which is an order of magnitude smaller than for EL from MoS_2[95, 101].

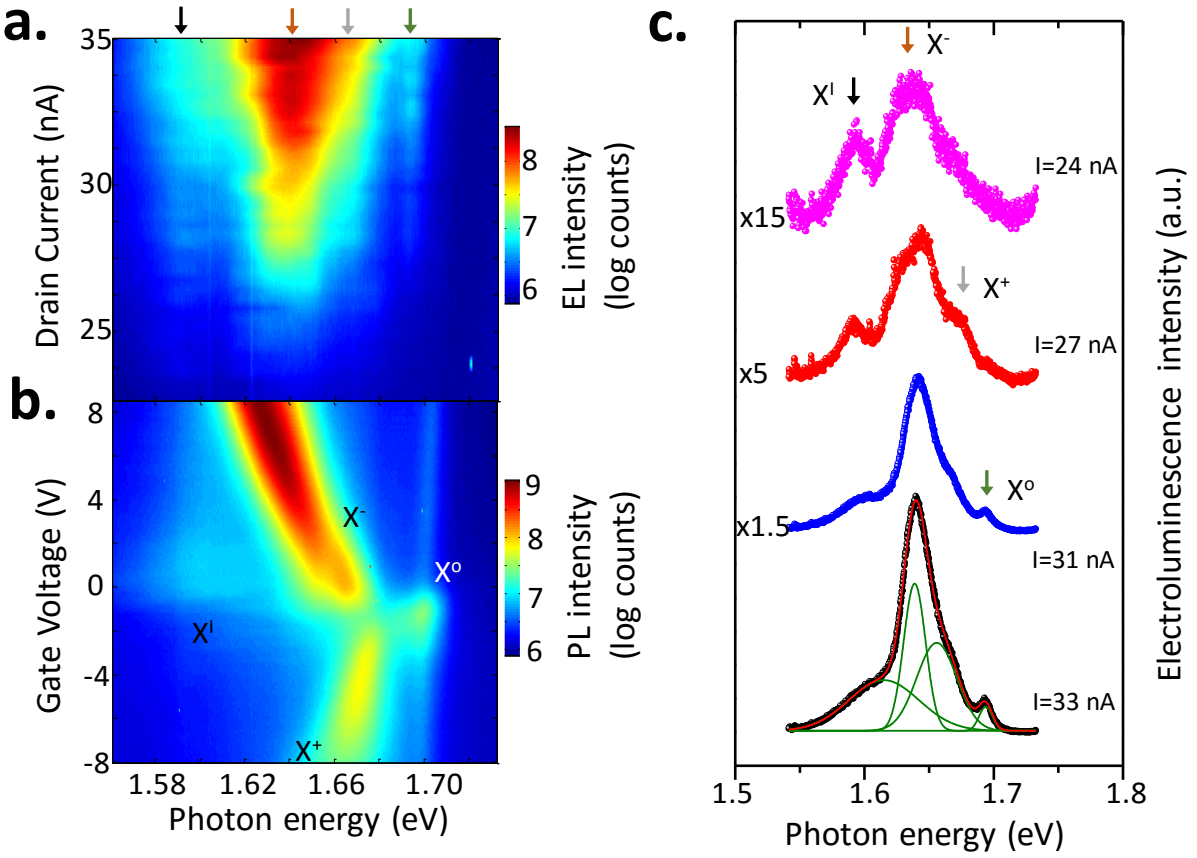

Figure 4.7. **Tuning Exciton Electroluminescence at 60 K**. a, Electroluminescence (EL) intensity plot as function of bias current and photon energy. From left to right, the arrows indicate the impurity-bound exciton (X^I), the charged excitons (X^- then X^+), and the neutral exciton (X^o). b, Plot of Photoluminescence (PL) intensity as a function of photon energy and gate voltage $V_g=V_{g1}=V_{g2}$. c, Selected EL spectra at different bias currents. As the current increases, I observe EL tuning from X^I through X^- and X^+ and finally X^o. The bottom spectrum is fit by four Gaussian lineshapes, one for each exciton species.

In Figure 4.7c I show the EL spectra at selected current values, illustrating sequential population of the excitonic states, which could be due to current pumping or to changes in the electric field at the junction under different source-drain biases. At the lower current (24 nA) only

the excitons with lowest energy (X^I and X^-) are seen. At a higher current (27 nA) the X^+ shoulder appears, and at 31 nA an X^0 peak is also present. At the highest current (33 nA) I illustrate how the spectrum can be decomposed into four Gaussian peaks. It is also apparent that the relative strength of the X^I peak decreases as the current increases.

The above observations reflect complex exciton dynamics which are not yet fully understood. Time-resolved PL measurements have shown that the lifetimes (for radiative and nonradiative processes combined) of the free excitons and the impurity-bound excitons are about 5 ps and 100 ps respectively[86, 105–107] in monolayer MoS_2, which I expect to be similar to WSe_2. The electron-hole pair injection rate is $\frac{I}{e}$ (e is electron charge), which is one pair per 5 ps at 32 nA, comparable to the lifetime of a free exciton but much shorter than that of X^I. Therefore, there could be only of order one free exciton but many impurity-bound excitons present in the junction. I speculate that the presence of multiple X^I combined with the strong Coulomb interactions enhances non-radiative recombination, which limits the X^I emission at higher currents. Alternatively, the saturation of the X^I peak could also be due to the filling of impurity states as observed in standard PL and photocurrent experiments.

4.8 LED EFFICIENCY

Before calculating the device efficiency, it is prudent to explain how the experimental setup was calibrated. For EL, the signal is collected by a 40X, NA 0.6 objective, passed through the 685 nm dichroic beam splitter and sent into the spectrometer setup. The efficiency of the system is $\alpha = \alpha_{obj}\alpha_{NA}\alpha_{spec}\beta_{spec}$, where α_{obj} is the transmission efficiency of the object leg, α_{NA} is the collection efficiency of the objective itself limited by numerical aperture, α_{spec} is the collection efficiency of the spectrometer leg, and β_{spec} is the ratio of efficiencies of the spectrometer

components (grating and CCD) at 660 nm (our calibration laser, see below) to those in the EL spectral range. The CCD and grating specification sheets were used to estimate β_{spec}. A Thorlabs S120VC power meter and a 660 nm diode laser were used to calibrate α_{obj} and α_{spec}. Finally, the objective collection efficiency is given by the integral over the solid angle defined by the numerical aperture[101, 108]:

$$\alpha_{NA} = \frac{3}{4\pi}\int_0^{2\pi} d\phi \int_0^{\arcsin(NA/n)} d\theta \sin\theta = \frac{3}{2}\left(1 - \sqrt{1 - \left(\frac{NA}{n}\right)^2}\right).$$

In our case, n = 1 since the WSe_2 is not covered with any material. The total photon emission rate from the junction is then $G = G_{\text{measured}}/\alpha$. The rate of electron and hole injection is I/e, and hence the efficiency (number of photons produced per injected electron) is $\frac{e}{I}G$.

With the above information, the total photon emission rate at the largest applied current of 35 nA is estimated to be about 16 million sec^{-1}. This is 10 times larger, for 1000 times smaller current, than reported for MoS_2 devices[29, 47]. It corresponds to 1 photon per 10^4 injected electron-hole pairs. We expect that the overall device efficiency could be improved by increasing the injection current for a given voltage by reducing contact resistance, improving the WSe_2 crystal quality, and by employing improved membrane transfer techniques.

4.9 Final Remarks

I demonstrated that EL from WSe_2 is undoubtedly from excitons which has significant implications. It has been conclusively demonstrated using polarization-resolved PL that the excitons in monolayer WSe_2 are formed in the ±K valleys[13]. The excellent match of the EL with the PL thus proves that the EL also comes from such valley excitons. However, no circular polarization of EL greater than the experimental error has been observed (Figure 4.8a). To

understand this, consider that in the experiments described here the injected electrons and holes populate both valleys equally as sketched in Figure 4.8b, forming excitons in both valleys and thus producing light that is an incoherent, equal mix of right and left circular polarization. Looking forward, schemes for overcoming this EL valley degeneracy are discussed in Section 4.10: Future 1: Valley Polarized LED, below.

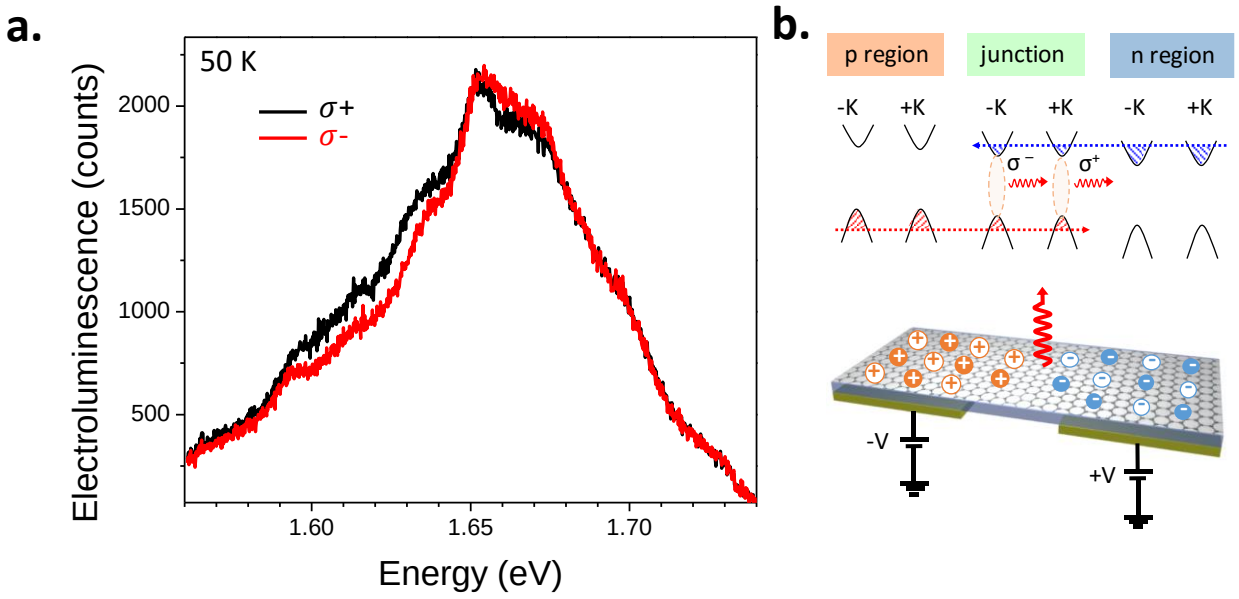

Figure 4.8. **Lateral Valley LED**. **a,** Electroluminescence (EL) under left (σ-) and right (σ+) polarization detection showing no appreciable polarization. The difference in left and right circularly polarized EL shows inconsistent fluctuations and never exceeds 5%, the systematic error of this measurement due to optics. Currently, we attribute any perceived polarization to the time-dependent fluctuations in the EL. **b,** Band diagram and device schematic showing EL generation from valley excitons. Wavy red arrows indicate electroluminescence. Dashed red (blue) arrow indicates the direction of hole (electron) flow. Filled and empty circles indicate carriers in the +K and -K valleys. Both valleys are shown to be populated leading to EL that has both right (σ^+) and left (σ^-) circular polarization.

The above work is published in Nature Nanotechnology[49] and it is important to note that two very similar studies were conducted and published alongside it[50, 51].

4.10 FUTURE 1: VALLEY POLARIZED LED

As a result of the spin-valley locking in monolayer TMDs, where the +K and -K band edges have opposite spin[18], It might be possible that using ferromagnetic contacts to obtain spin-polarized injection will allow spin- and valley-LEDs with controllably polarized emission[109]. Similarly, a high performing device in a vertical magnetic field might also produce an observable effect.

However, a different approach that exploits only the intrinsic properties of the materials has emerged as the most promising. Valley polarization in WSe_2 electroluminescence was recently observed and attributed to trigonal warping of the electronic bands[52]. This is the fact that the shape of the bands at the valleys is not perfectly parabolic[110, 111], and that at large doping levels and with an applied in-plane E-field, each valley contributes different amounts of carriers to the conduction (Figure 4.9a). This causes the EL to have an overall circular polarization, which is switchable if the E-field is reversed. Using ion gel gating to obtain high doping and thus strong trigonal warping, circularly polarized EL was observed in various MX_2 samples including WSe_2 and $MoSe_2$[52].

Conversely, this simplified picture has been modified and challenged by recent theory. When electron spin is accounted for, trigonal warping, or, more descriptively, anisotropy of the valley Fermi pockets, produces different effects depending on how the applied E-field is aligned to the crystal axis. Along the armchair direction, there should be an overall circular polarization in the EL, dependent on the direction of the E-field like the previous case (Figure 4.9b). However, along the zig-zag direction, the carriers from each valley drift to opposite directions perpendicular to the

E-field producing a spatial variant polarization in the EL. And further, the spatial invariance does not reverse when the E-field is reversed (Figure 4.9c).

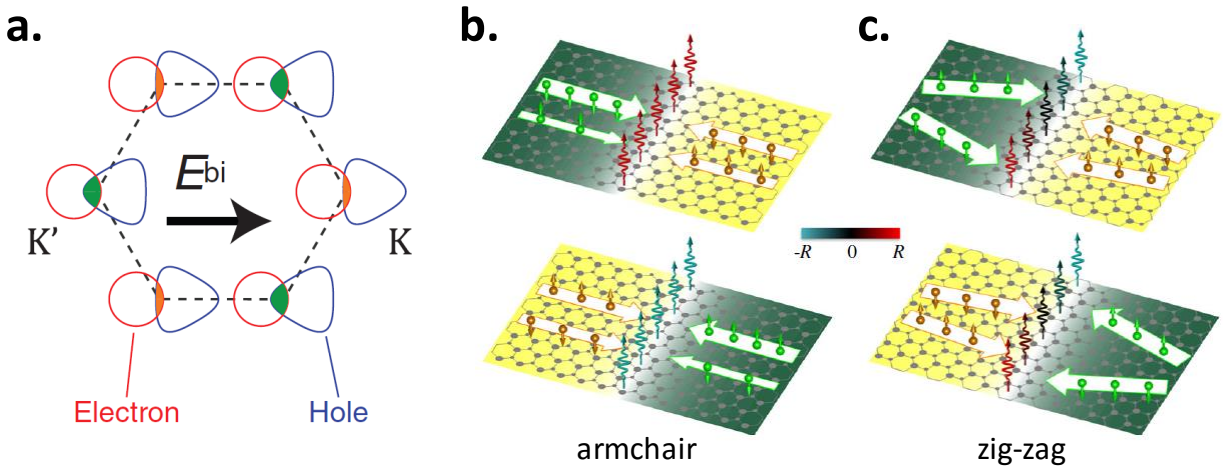

Figure 4.9. **Valley Polarized Electroluminescence Schemes**. **a,** Carrier contribution from each valley under electric field due to trigonal warping. Orange (green) color represent free carrier density in K (K') valley. From reference [52]. **b**, Circularly polarized electroluminescence from p-n junction that is perpendicular to the armchair direction. **c**, same as **b** but with p-n junction perpendicular to the zig-zag direction. Green (yellow) color denotes hole (electron) doped region. Red (teal) squiggly arrows represent right (left) circularly polarized light. Red (green) pins with arrows denote carriers and their spin (and thus valley) current. The junction direction and E-field is reverse between top and bottom image. From reference [112].

This prediction stands as untested and, if observed, could cast doubt on the trigonal warp results mentioned about from reference [52]. With this in mind, it is important to test the spatial dependence of the polarization of EL from a new generation of lateral LED devices. For these devices, second harmonic generation (SHG) measurements on the WSe_2 crystals can be used to

determine the armchair axis[113], allowing for the intentional fabrication of devices whose current will run either along the zig-zag or armchair direction. Such a study could finally pinpoint the interplay between trigonal warping and spin-valley currents in lateral TMD devices.

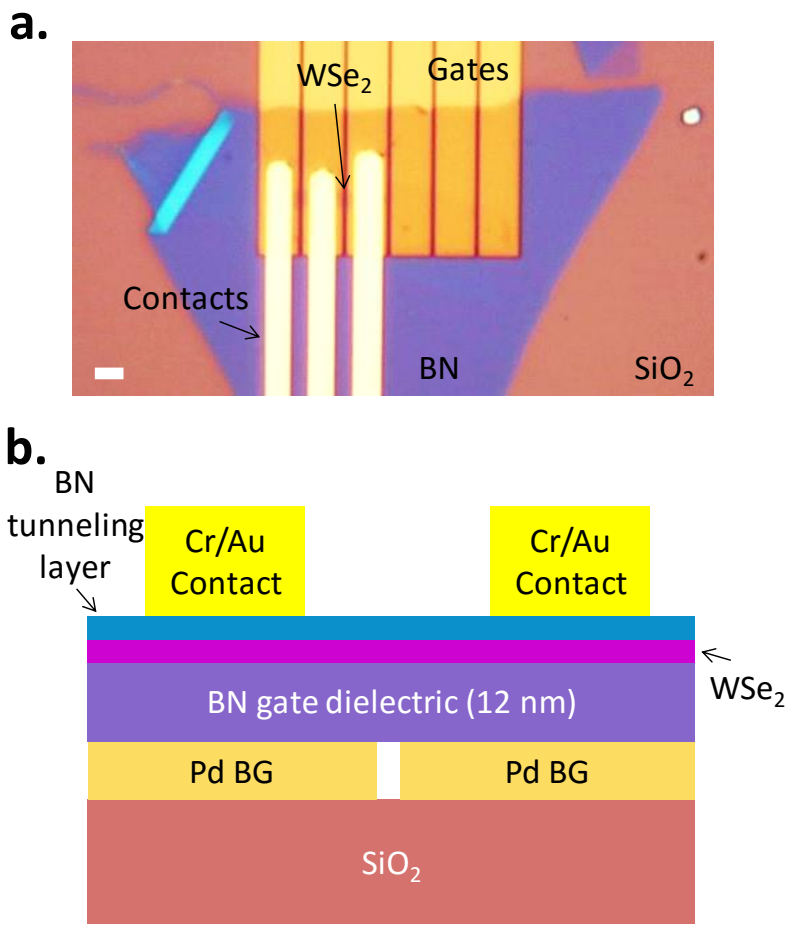

Figure 4.10. **New WSe_2 LED**. **a,** Microscope image of device. Here, fabrication resulted in two adjacent devices. The tunneling BN (t-BN) is not visible, only the BN gate dielectric in blue. Scale bar: 1 μm. **b,** Schematic of device showing tunneling BN layer between metallic contacts sand monolayer WSe_2.

4.11 FUTURE 2: IMPROVED DEVICE DESIGN AND $MoSe_2$ LED

In order to improve the success of future studies, improvements on the lateral LED device design are needed. The first step to take is to implement cleaner monolayer transfer and stacking techniques such as the PC dry transfer and possibly performing the transfer in a glove box or vacuum chamber. The second major improvement can be to the contacts, specifically using a thin (1 to 2 layers) of BN between the metallic contacts and the active semiconducting monolayer. Thin layers of BN like this have been shown to allow carrier tunneling with high efficiency[34, 35]. Tunneling contacts have the added bonus that if the layer is large enough, it can seal and passivate the entire device, protecting it from environmental degradation[36].

Combining these two improvements, next generation WSe_2 LEDs were studied. Figure 4.10a shows the microscope image of the sample showing two devices. The tunneling BN layer (t-BN) is not easily visible here, but after PC transfer fabrication it was the top layer and so now is present between the monolayer WSe_2 and the EBL fabricated Cr/Au contacts (Figure 4.10b).

This device showed markedly improved EL performance. Figure 4.11a shows a spatial image of the EL (red) from running both devices simultaneously overlaid onto the device area (black and white). To drive both devices, the middle gate is set positive (V+ in the figure) establishing an n-doped region in the middle, while the outer gates are set negative (V- in the figure) to establish two outer p-doped regions in the WSe_2. Applying a positive bias to the outer contacts source contacts (S in figure) drives current into the grounded drain contact (D in figure).

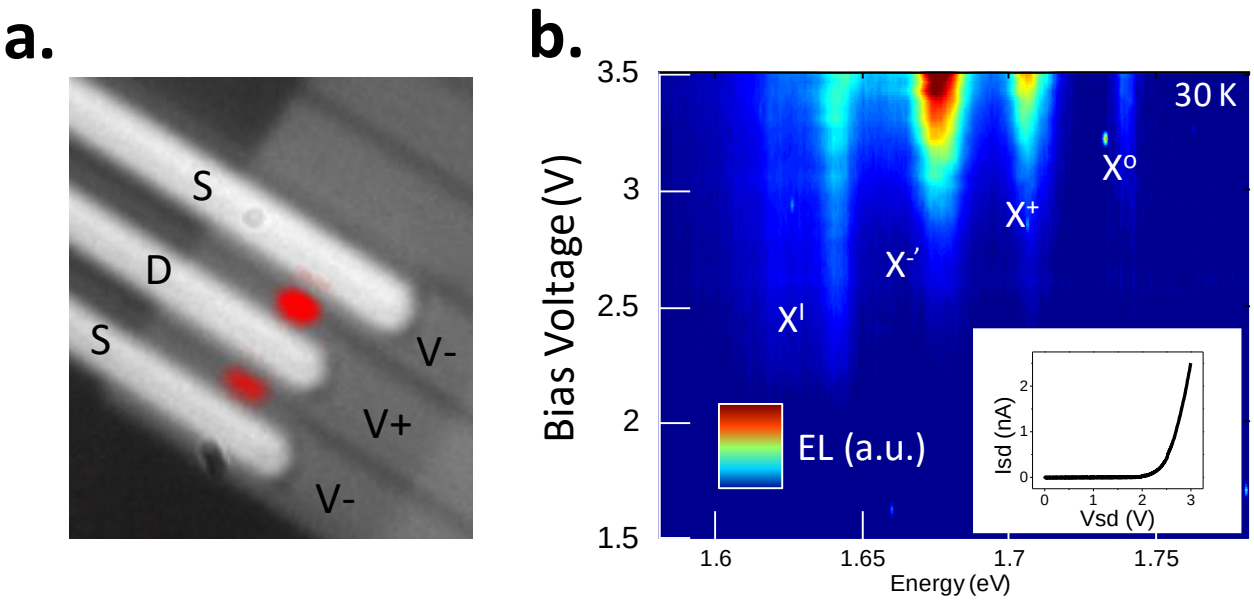

Figure 4.11. **Improved Exciton EL**. **a,** Electroluminescence (red, arbitrary units) overlaid onto spectrometer image of devices (black and white). The middle gate was set positive (V+) establishing an n-doped WSe_2 middle region while the outer gates were set negative (V-) to establish two p regions. Carriers were injected into the outer source (S) contacts and collected at the middle drain contact (D). **b,** EL vs. Bias voltage shows improved separation of exciton states and obvious state filling trend. Inset: Current vs Bias Voltage curve taking during EL sweep.

Looking at the bias voltage dependence of the EL spectrum reveals improved excitonic emission. In Figure 4.11b, we see obvious evidence of state filling where the exciton states at lowest energy (the impurity exciton X^I here, at ~1.64 eV) are first to emit light but as the bias is increased the higher energy states (charged and neutral excitons) become brighter. Most strikingly, we see a significant reduction in the overlap of the individual exciton peaks hinting that the sample is cleaner than the previous device design results. Finally, it's important to note that the current needed to observe EL (inset in Figure 4.11b) in these new devices is about an order of magnitude

less than before which is testament for the efficiency t-BN contacts. This design process has become the standard for lateral LED fabrication as well be shown below for monolayer $MoSe_2$ LED and TMD HS LEDs studies.

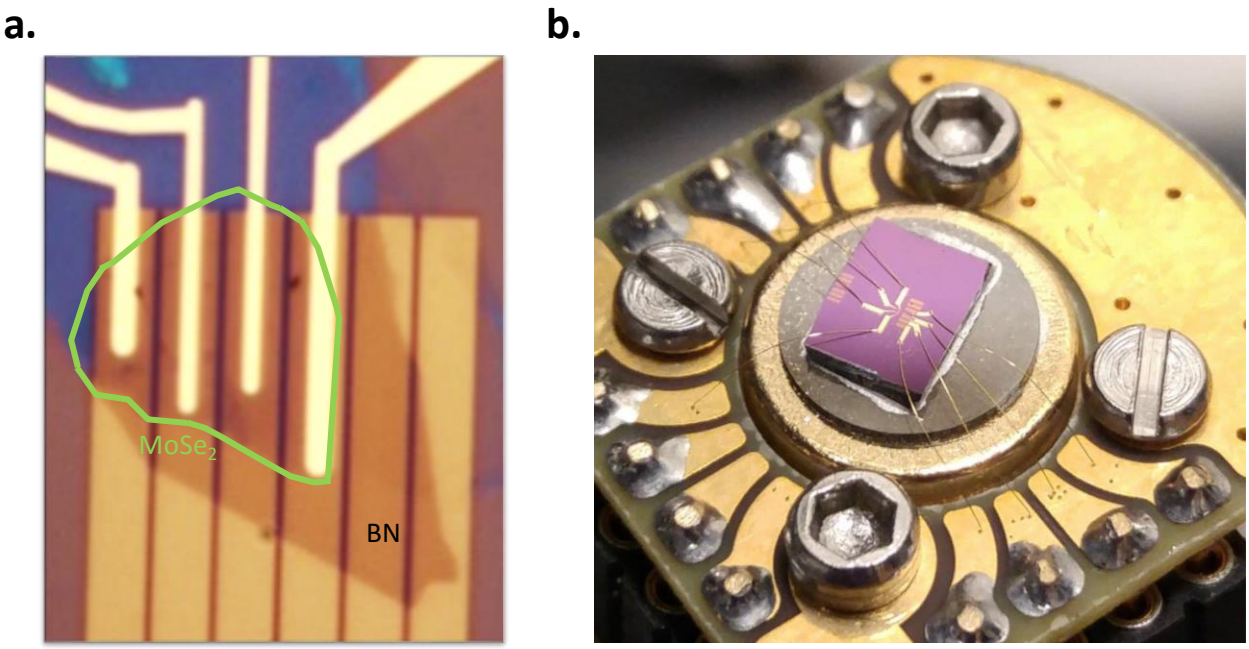

Figure 4.12. **$MoSe_2$ Lateral LED**. **a,** Microscope image of t-BN lateral $MoSe_2$ LEDs. Here we have 3 adjacent devices thanks to large BN and $MoSe_2$ (green outline) flakes. **b,** Camera image of the device mounted to cryostat chip carrier with wire bonds attached to contact pads.

In Chapter 5 we present the study of an LED with the active layer being a HS of WSe_2 and $MoSe_2$. Thus, here we present monolayer $MoSe_2$ LED data to illustrate that this lateral LED device design works universally with all TMDs. Figure 4.12a shows a microscope image of the sample which resulted in three adjacent $MoSe_2$ p-n junctions. This device was fabricated with the PC dry transfer technique and has monolayer t-BN contacts along with a 10 nm thick BN dielectric layer. For some insight into how these devices are measured inside our optical cryostat, we show in

Figure 4.12b a camera photograph of the silicon chip mounted to the chip-carrier with wire bonds connected it to the outside circuitry.

Focusing on one device, with back gate voltages $V_{GP} = -0.5\,V$ and $V_{GN} = 5\,V$ and a bias voltage of $V_{SD} = 3.5\,V$ giving a current of 1.3 nA, we observe a strip of EL emitted from almost the entire junction between two gates (red color Figure 4.13a). Looking at the spectrum of the EL we observe the two characteristic $MoSe_2$ exciton and trion peaks (X^o, X^- and X^+ in Figure 4.13b) which due to this spectrum being strikingly similar to the PL shown in Figure 3.3b in Section 3.1: Spectral Features. In contrast to the PL, where the trion peak is either X^+ or X^- depending on the doping, it is assumed the EL trion peak at ~ 770 nm is made up of both charge species as they each are injected from their respective p and n sides of the lateral junction. A weak and lower energy peak at around 925 nm is also observed in the EL (X? in Figure 4.13b inset). The origin of this peak requires further studies to identify but it is important to note because the interlayer exciton emission in a WSe_2-$MoSe_2$ HS is in the same spectral range albeit much brighter and narrower.

The bias dependent of the EL in this device shows standard state filling as described for WSe_2 LEDs above (Figure 4.13c). Interestingly, there are very sharp peaks observable within the exciton peaks (X^D in Figure 4.13c) which due to their linewidths can be attributed to defect bound excitons that are actually thought to be single quantum emitters[114]. Thus the result here is that we can electrically pump single quantum emitters using this LED device design.

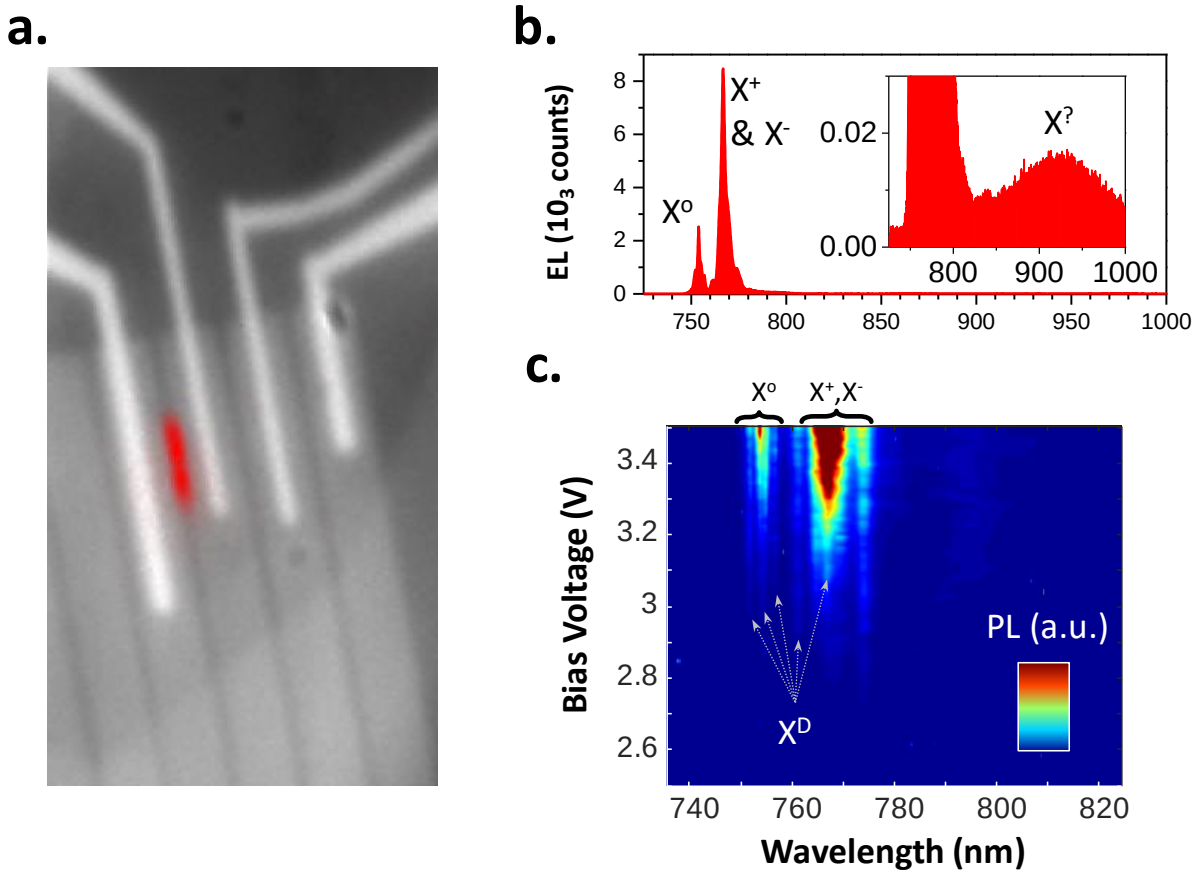

Figure 4.13. **$MoSe_2$ Excitonic Electroluminescence**. **a,** Electroluminescence (EL) (red, arbitrary units) overlaid onto spectrometer image of devices (black and white). **b,** EL spectrum of device shown in (a). The lower wavelength peak (higher energy) is the neutral exciton (Xo) while the higher wavelength (lower energy peak) is the charged exciton (a mixture of X- and X+ from the trions from both the n an p sides of the device). Inset shows a weak and broad emission is present at around 925 nm which has yet to be identified ($X^?$). **c,** EL vs. bias voltage shows standard state filling (lower energy excitons emit first) as well as sharp, likely defect bound excitons (X^D) within both exciton peaks.

Chapter 5. ATOMICALLY SHARP HETEROSTRUCTURES

So far in this Thesis we have presented the study of semiconductor physics at the ultimate 2D limit by investigating single layer atomically thin materials. The next logical leap to take is to sandwich two 2D semiconductors together and study the first atomically sharp semiconductor heterostructure juctions akin to the quasi-2D GaAs-AlGaAs or GaN-AlGaN junctions. In this chapter we present breakthroughs made in studying 2D heterojunctions between monolayers of $MoSe_2$ and WSe_2. In addition to establishing a built-in p-n junction between the materials due to type-II band alignment, this HS also exibits a unique interlayer exciton that shows promise for photonic devices. We refer the reader to references [68, 115] for more details.

5.1 HETEROSTRUCTURE AND INTERLAYER EXCITON INTRODUCTION

The diverse family of van der Waals materials offers a unique platform for building pristine heterojunctions with designed functionalities at the atomically thin limit[6]. Two-dimensional (2D) materials with metallic (graphene), semiconducting (group VIB transition metal chalcogenides), and insulating (boron nitride) properties are now readily available and can be cleanly stacked[32] into complex heterostructures (HSs). This has led to exciting progress both in science, such as the artificial superlattice in Hofstadter's butterfly[59–61], and band-gap engineered devices, mainly efficient light emitting diodes and photodetectors[37, 116].

In individual layers of transition metal chalcogenides (TMDs), the direct band-gaps[11, 39] and valley dichroism[13, 19, 21, 56, 109] have suggested a new valleytronics paradigm is imminent and have already inspired diverse applications in photovoltaics and light emitting devices (LEDs)[29, 37, 47–50, 52]. Vertically stacking two TMDs together forms a new type of optically active heterojunction with type-II band alignment[62–64, 117]. This results in an built-

in vertical p-n junction at the atomic scale and causes optically excited electrons and holes to be subsequently separated into opposite layers[66, 67].

Due to the reduced screening effects in 2D, the spatially separated electron and hole still experience strong Coulomb interaction and thus form tightly bound interlayer excitons (X_I). X_I has a few hundred meV binding energy[118], inherits valley dependent physical properties from monolayers[119], and exhibits electrically tunable population and valley polarization lifetimes on the order of tens of ns[115]. However, the role of X_I in optoelectronic devices remains elusive due to the following facts. As a result of the reduced overlap of the spatially separated electron and hole wave functions, X_I oscillator strength is expected to be dramatically reduced compared to intralayer excitons in individual monolayers. In addition, the inevitable twist between the monolayers during the fabrication also gives rise to the misalignment of band edges, i.e. X_I is momentum indirect[115, 119]. It is unclear how this momentum indirect exciton with weak oscillator strength will behave in optoelectronic devices, such as light emitting diodes (LEDs) and photodetectors. Further, X_I has only been observed in photoluminescence measurements. The weak oscillator strength and momentum indirect nature make it challenging to directly observe the interlayer exciton by resonant optical excitation. An approach to resonantly probe X_I and determine its oscillator strength is necessary for the realization of exotic physical phenomena (e.g. interlayer exciton valley currents[119] and efficient optoelectronic devices based on X_I.

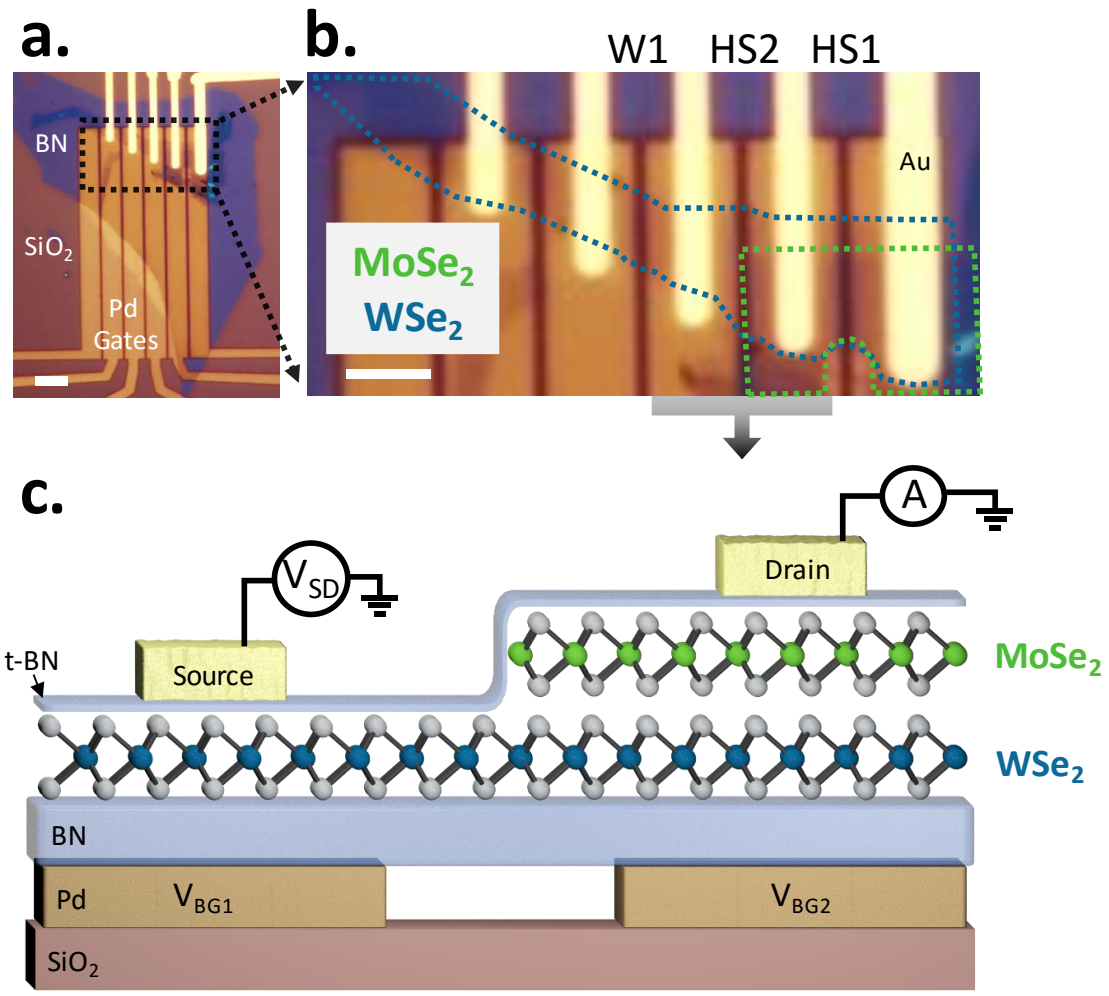

Figure 5.1. **Device description**. **a,** Wide view microscope image of device area. Scale bar 2 μm. b. Zoom view of active area of showing three distinct devices. Dotted lines outline $MoSe_2$ (green) and WSe_2 (blue) monolayers. HS2 is the device made up of two Pd gates and two Au contacts below the HS1 label. Scale bare 2 μm. c. Cartoon of HS2 showing all material layers and electrical contacts.

5.2 HS LED Device Design

In this paper, we report electrostatically defined p-n junction devices made of $MoSe_2$-WSe_2 HSs which enables us to resonantly probe and investigate the optoelectronic response of X_I. The p-n junction design used here is adopted from Ref. [49]. Palladium back gates separated by 300 nm gaps are used to dope adjacent p and n regions in the 2D heterostructure above them (Figure 5.1a-c). To construct the HS device, the following layers are stacked using a modified version of the polycarbonate (PC) based dry transfer technique[71]. First a roughly 10 nm thick BN layer serves as the gate dielectric. Then a single layer each of $MoSe_2$ and WSe_2 are stacked with care taken to align their armchair crystal axes, which are identified by polarization resolved second harmonic generation (SHG) measurements[113]. Minimizing the twist angle between the layers aligns the combined Brillouin zone for both layers allowing for light cones to exist at small momenta and thus bright interlayer exciton emission[115, 119] (see next section).

On top of the TMDs, a single layer of BN is used both as a passivation layer to protect the active device as well as an efficient tunneling contact (t-BN in Figure 5.1c)[36]. Au source and drain contacts are defined directly on top of the tunneling BN layer.

Figure 5.1b is a microscope image of the active area of the fabricated device, with the blue and green dashed lines indicating the boundaries of monolayer WSe_2 and $MoSe_2$, respectively. There are three distinct p-n junctions in this particular device, a monolayer WSe_2 labeled W1, and two heterostructures, labelled as HS1 and HS2. For HS2, our transfer technique enables precise placement on the order of 1 μm allowing the edge of $MoSe_2$ layer to be positioned directly along the gap between two gates. This is essentially a half-HS device, in which only one side of the device is a HS while the other side is a single layer of WSe_2 (Figure 5.1c), allowing direct electrical contact to each constituent monolayer of the heterostructure. This device was the goal during

fabrication with the idea to directly inject the charge carrier that is favored by the constituent material due to band alignment and charge transfer discussed below. The main focus of this chapter will be the results from HS2, while the data from HS1 and W1 can be found in Appendix A.

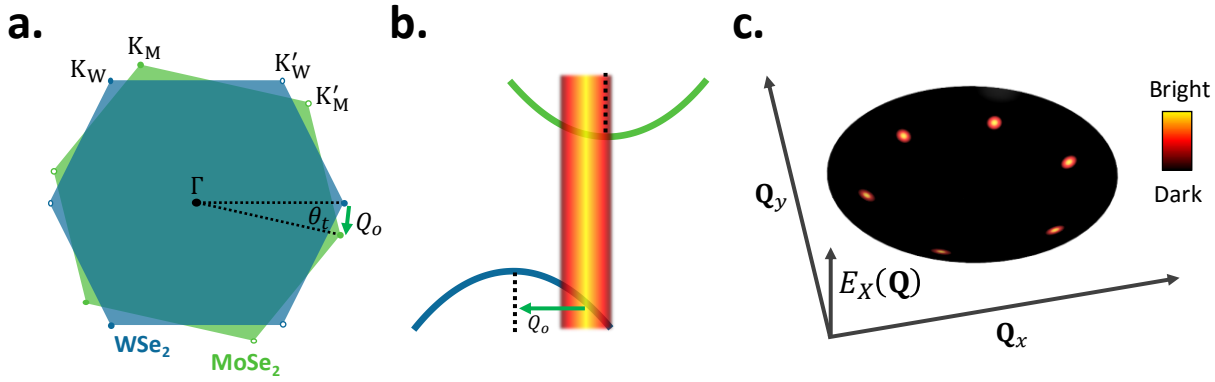

Figure 5.2. **Twist angles and light cones**. **a,** Two hexagonal Brillion zones when stacked with a small twist angle θ_t will result in the K valleys between materials having a momentum offset of Q_o. **b**, Light cone at Q_o from the WSe_2 valence band. **c,** The six light cones in the complete 2D interlayer exciton energy-momentum dispersion. Figures recreated based on reference [2].

5.3 Twist Angles and Light Cones

A small twist angle (θ_t) results in the K valleys of constituent materials in the TMD HS to become momentum mismatched in the first Brillion zone (Figure 5.2a). The displacement vector Q_o (green arrow in the figure) is the combined momentum of an electron and hole necessary to recombine for an optically bright interlayer transition[119]. This means there's a light cone at Q_o away from the K point (the band edge) of a given material, e.g. the valence band edge of WSe_2 (Figure 5.2b). Only interlayer excitons with enough kinetic momentum will emit light. Further, due to six-fold rotation symmetry, there are six light cones in the complete 2D exciton energy-momentum

dispersion with the interlayer exciton optically dark at $\boldsymbol{Q} = 0$ (Figure 5.2c). Minimizing the twist angle minimizes the $\boldsymbol{Q}$ required for bright excitons and thus SHG is always used to line up the TMD armchair axes during HS fabrication.

5.4 BAND ALIGNMENT AND TRANSPORT

Having a contact to each constituent layer of the HS2 allows for layer specific carrier injection of the type preferred according to the HS band alignment and interlayer charge transfer[66, 68, 115, 120]. This is made clear in Figure 5.3a which illustrates the ungated band edge diagram along HS2. On the right side of the figure (the HS side), type-II band alignment results in $MoSe_2$ having the lowest energy conduction band and thus favoring electron injection, while WSe_2 has the highest energy valence band and thus favors holes. With this and having one contact directly to each layer, efficient ambipolar carrier injection should be possible via global back-gate doping (V_g in Figure 5.3b). The black curve in Figure 5.3b shows that hole conduction turns on at -2 V while electron conduction turns on at $+4$ V with a bias voltage of $V_{SD} = 500$ mV. An example source-drain bias curve (red) under p-doped conditions ($V_g = -2.5$ V) shows mostly Ohmic conduction despite a small barrier region near zero bias voltage similar to previous lateral TMD LEDs[49].

With ambipolar injection, setting the back gates to opposite voltages establishes a lateral p-n junction. Figure 5.3c illustrates gating configuration where a negative voltage on V_{BG1} injects holes into the WSe_2 while a positive voltage on V_{BG2} injects electrons into $MoSe_2$ resulting in the band diagram shown in the figure. Practically speaking, with $V_{BG1} = -1$ V and $V_{BG2} = 5$ V, sweeping the source-drain voltage V_{SD} from -3.5 to 3.5 V shows only forward bias conduction (blue line in Figure 5.3g), confirming a lateral p-n junction.

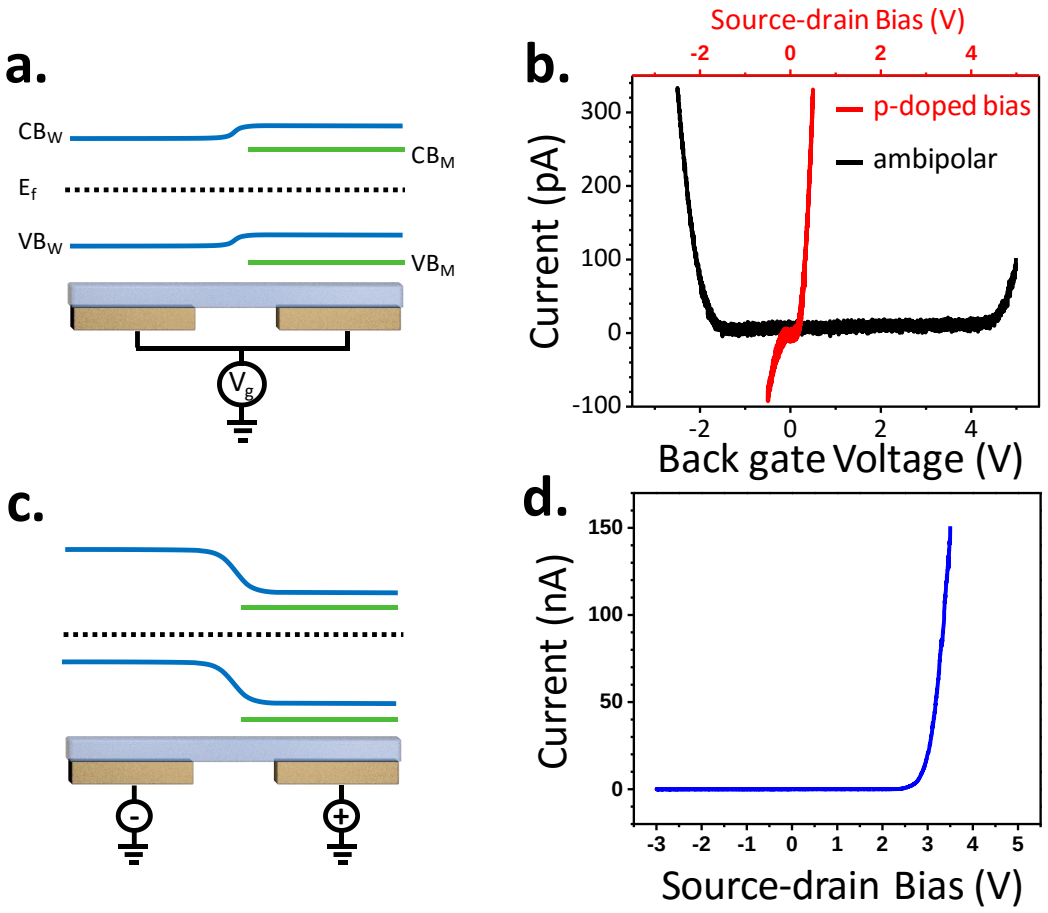

Figure 5.3. **Band alignment and transport**. **a,** Band diagram along HS2 with zero gate doping showing conduction band (CB) and valence band (VB) for WSe_2 (blue) and $MoSe_2$ (green). Dotted line is fermi level (Ef). The electrical setup for global back-gate doping where both gates are swept together is illustrated via the back gates connected together and bias by Vg. **b**. Ambipolar (black curve with VSD = 500 mV) and p-doped bias (red curve with VG = -2 V) conduction of device in the global back-gate setup. **c,** Band diagram along HS2 under p-n junction gating where – and + refer to the voltage applied to the individual back gates being negative and positive. **d,** p-n junction diode conduction curve under gating setup illustrated in (f).

The reason for the smaller voltage on V_{BG1} is because of the interplay with V_{SD} which is applied to the source contact electrode on WSe_2 whereas the drain electrode on $MoSe_2$ is grounded. As V_{SD} is ramped up and drives source-drain current, the voltage drop across the boron nitride (BN) dielectric increases and thus the WSe_2 hole doping increases such that at $V_{SD} = 3.5$ V, the gating in WSe_2 is comparable to the gating in $MoSe_2$ when $V_{BG2} = 5$ V. If the gate voltages were equal and opposite, say -5 and +5 V, as V_{SD} is increased the BN dielectric would break down before forward bias conduction occurs. This is a limitation of these electrostatically defined lateral p-n junctions. In the negative V_{SD} regime, we have swept V_{BG1} to – 8 V in order to ensure comparable p and n doping on respective sides of the device and no reverse bias conduction is observed confirming we have a diode.

5.5 Interlayer Electroluminescence

The formation of p-n junction allows us to investigate electroluminescence by applying forward bias. Figure 5.4a shows a microscope image (top) of the device along with a corresponding spectrometer image (bottom) of the EL (red) at $V_{SD} = 3.5$ V bias overlaid onto the device (black and white). Clearly, the EL originates from the HS region along the gap between the gates (red arrow) with a lack of EL coming from the WSe_2-only region (black arrow). This suggests that either most of the current is flowing through the HS region (possibly due to better ambipolar doping) or that the emission in the HS region is brighter because only the lower energy interlayer emission is accessed in these conditions. This is resolved by comparing the spectra of EL to un-gated photoluminescence (PL) of HS1 under 532 nm excitation, both at 5 K (Figure 5.4b). In PL (black curve), we observe emission from the intralayer excitons of both $MoSe_2$ and WSe_2 (1.56 to 1.74 eV[12, 13]) as well as emission below 1.4 eV characteristic of the $MoSe_2$-WSe_2 interlayer

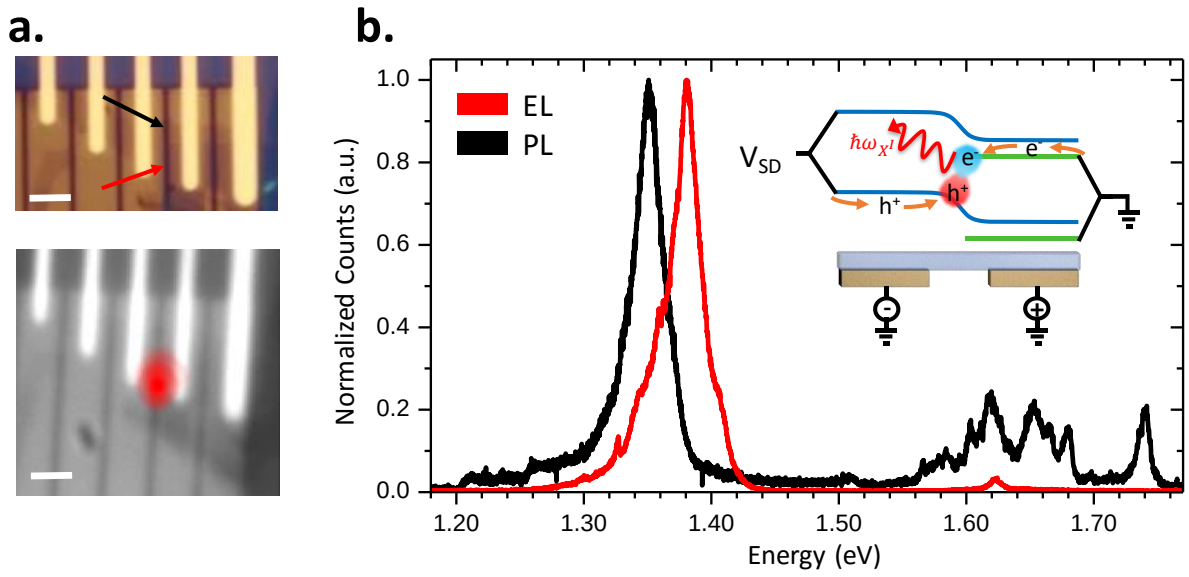

Figure 5.4. **Interlayer Exciton Electroluminescence**. **a,** Top: microscope image of device area with arrows pointing to WSe_2-only region (black) and HS region (red) of HS2 device. Bottom: electroluminescence (EL) image (red) overlaid on top of white light illuminated spectrometer image of device area (black and white). Both scale bars 2 μm. **b.** Spectra of EL (red) compared to photoluminescence (black) for HS2. Inset cartoon illustrates which layer each source and drain contact (black lines) is connected to and how carriers are thus injected into the device and then the p-n junction recombination area (orange arrows). In the center, the carriers bind into an interlayer exciton (red-blue cloud illustrates the interlayer diode) before emitting light at the interlayer binding energy, $\hbar\omega_{X^I}$.

exciton[68, 115]. However the EL (red curve) is clearly dominated by interlayer emission with a small amount of intralayer emission observed at about 1.62 eV, likely from the $MoSe_2$ trion[12]. This result demonstrates that despite the weak electron-hole wavefunction overlap, the lower energy of X_I makes it the dominant recombination pathway at the junction (cartoon inset in Figure

5.4b) compared to intralayer excitons. Sequentially speaking, the injected electrons in the $MoSe_2$ conduction band and holes in the WSe_2 valence band meet in the p-n junction, bind into X_I due to strong Coulomb interactions, and then recombine to emit light.

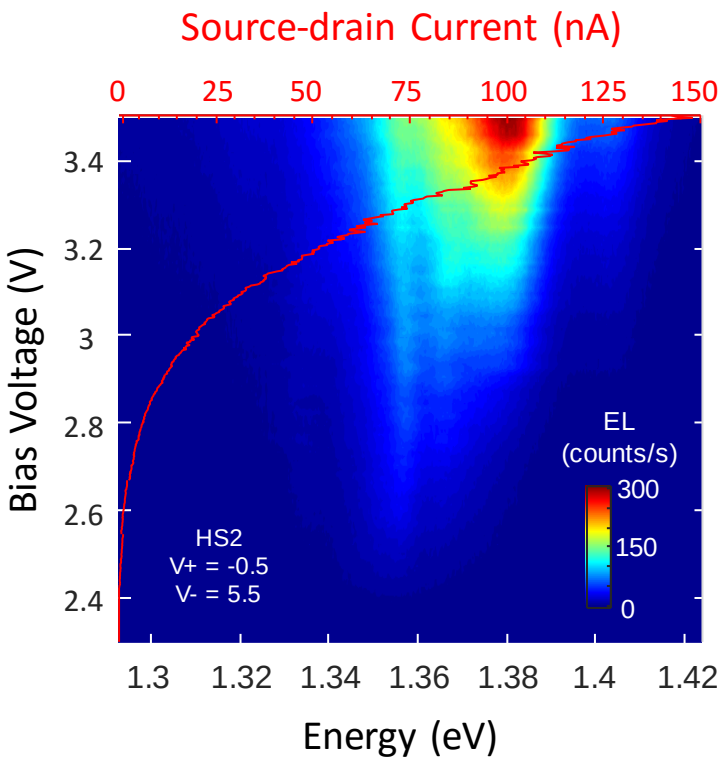

Figure 5.5. **EL Bias Dependence**. Source-drain bias dependence of interlayer exciton EL in HS2 with corresponding diode transport curve (red) overlaid.

The EL from HS2 also shows possible state filling effects similar to previous lateral monolayer TMD LEDs[49], where emission favors lower energy states and higher energy states can be accessed with larger source-drain bias voltages[49]. Mapping the low energy EL versus V_{SD} at 30 K, we see this behavior even within the interlayer emission itself (Figure 5.5). As V_{SD} is swept from 2.3 V to 3.5 V, the dominant emission moves from 1.355 eV to 1.38 eV. In contrast,

vertical electric field modulation of the interlayer dipole has previously shown continuously tunable X_I PL energy over a roughly 200 meV range[68]. This can also explain the EL vs bias behavior here since the bias voltage sweep modulates the vertical fields due to changing the voltage drop to each back-gate. Future work is needed to determine the roles of state filling and dipole tuning in this HS system.

5.6 INTERLAYER PHOTOCURRENT AND LIGHT CONE

The maximum EL efficiency observed here (~0.1 %) is comparable to that of single layer WSe_2 LEDs of similar design[49–51] which becomes interesting once the oscillator strength of interlayer and intralayer states are compared. To do this, photocurrent (PC) measurements were performed with $V_{BG1} = -3$, $V_{BG2} = +3$, and $V_{SD} = 0$, the photovoltaic condition. Figure 5.6a illustrates the band diagram and charge extraction for this scheme where photoexcited electron-hole pairs are separated by the p-n junction field and current is collected by the contacts. In Figure 5.6b inset, we show a PC scanning map (red in arbitrary units) under 2 μW, 632 nm excitation overlaid on a laser reflection map (black and white), which shows PC response is localized at the p-n junction region. Focusing the laser on this bright PC spot, wavelength dependent PC measurements were then performed. Figure 5.6b shows PC amplitude on a log scale showing intralayer exciton resonances clearly observable between 1.6 and 1.7 eV. PC amplitude drops drastically once the photo-excitation is below the lowest energy bright intralayer exciton, which is the $MoSe_2$ trion around 1.63 eV. Remarkably, a PC peak appears at about 1.41 eV, which corresponds to XI. This is the first observation of resonant optical excitation of interlayer exciton.

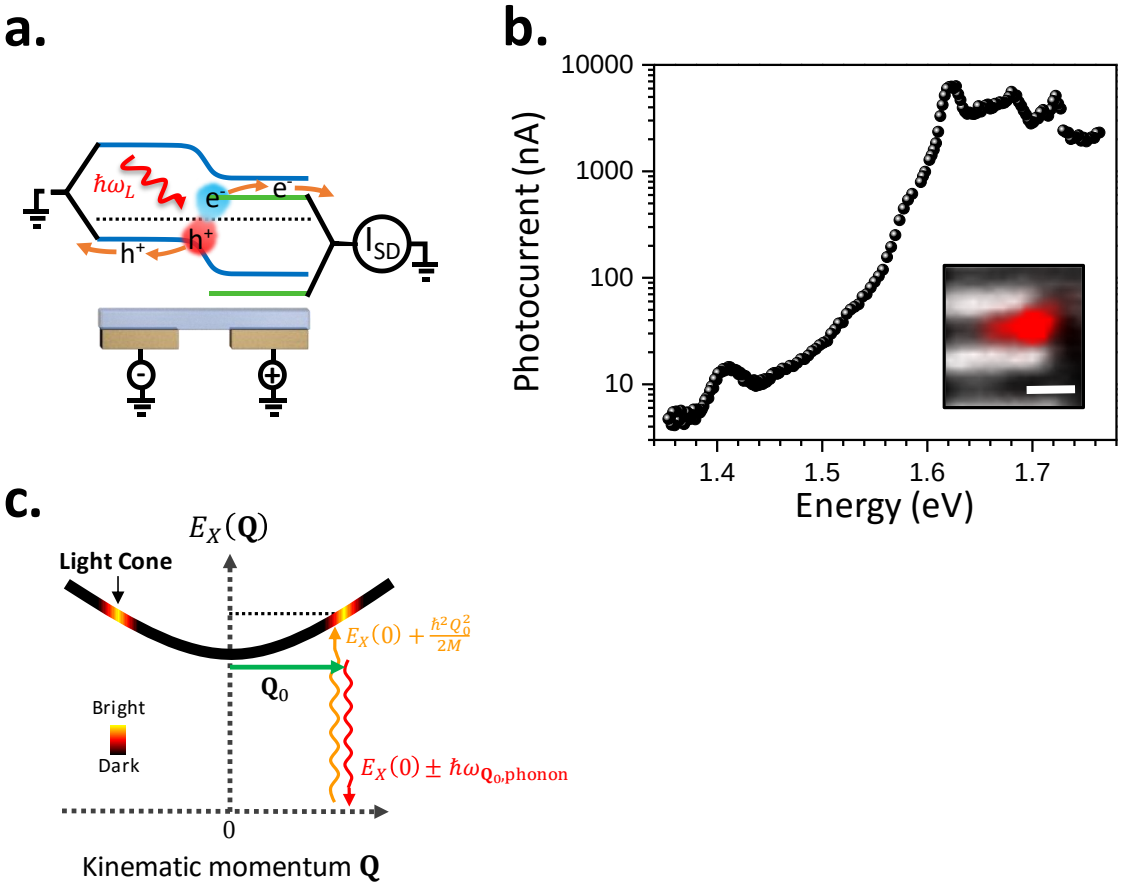

Figure 5.6. **Direct light coupling of interlayer exciton**. **a,** Cartoon illustration of photocurrent (PC) where incident laser light with energy $\hbar\omega_L$ creates electron-hole pairs that are separated by the p-n junction field and move out (orange arrows) to be collected by the contacts as current (I_{SD}). **b,** Wide range energy dependence of HS1 photocurrent (PC) under photovoltaic gating setup (see text). Inset: close up of scanning PC map (red, arbitrary units) overlaid onto corresponding scanning reflection map (black and white) of HS2. Scale bar is 2 μm. **c.** Interlayer exciton energy-momentum dispersion diagram. Light cones (yellow) exist at finite kinetic momentum (Q_O) for interlayer excitons. Excitons with the lowest energy (E_X) must be phonon-scattered into the light cone to emit light under photoluminescence or electroluminescence (red transition). PC must occur at the light cone and thus requires excitons with significant kinetic energy (orange transition).

The peak energy of the XI in PC spectrum is about 20~30 meV higher than any interlayer EL and PL peaks. This can be understood by considering that the light cones for interlayer transitions in samples with small twist angles are located at finite exciton momentum[119]. This unique aspect of the interlayer exciton dispersion is shown in Figure 5.6c, where the momentum conserving optical transitions appear at finite exciton momenta. Resonant excitation (orange squiggly line in Figure 5.6c) generates interlayer excitons only at the light cones with total energy $E_X(0) + \frac{\hbar^2 Q_0^2}{2M}$, where $E_X(0)$ is the binding energy of the exciton at rest and the second term is the kinetic energy for exciton center-of-mass momentum Q_0 and effective mass M. In contrast, EL and PL emissions (red squiggly line in Figure 5.6c) are primarily from cold excitons which are phonon-scattered into the light cones and emit with energy $E_X(0) \pm \hbar\omega_{Q_0,\text{phonon}}$. In device HS2, polarization-resolved second harmonic generation measurements confirms the twist angle to be about 3 degrees (Figure 5.7), which corresponds to an exciton kinetic energy of tens of meV at the light cones. Therefore, the PC resonance is expected to be at higher energy than the interlayer exciton PL and EL, which is consistent with our measurement results.

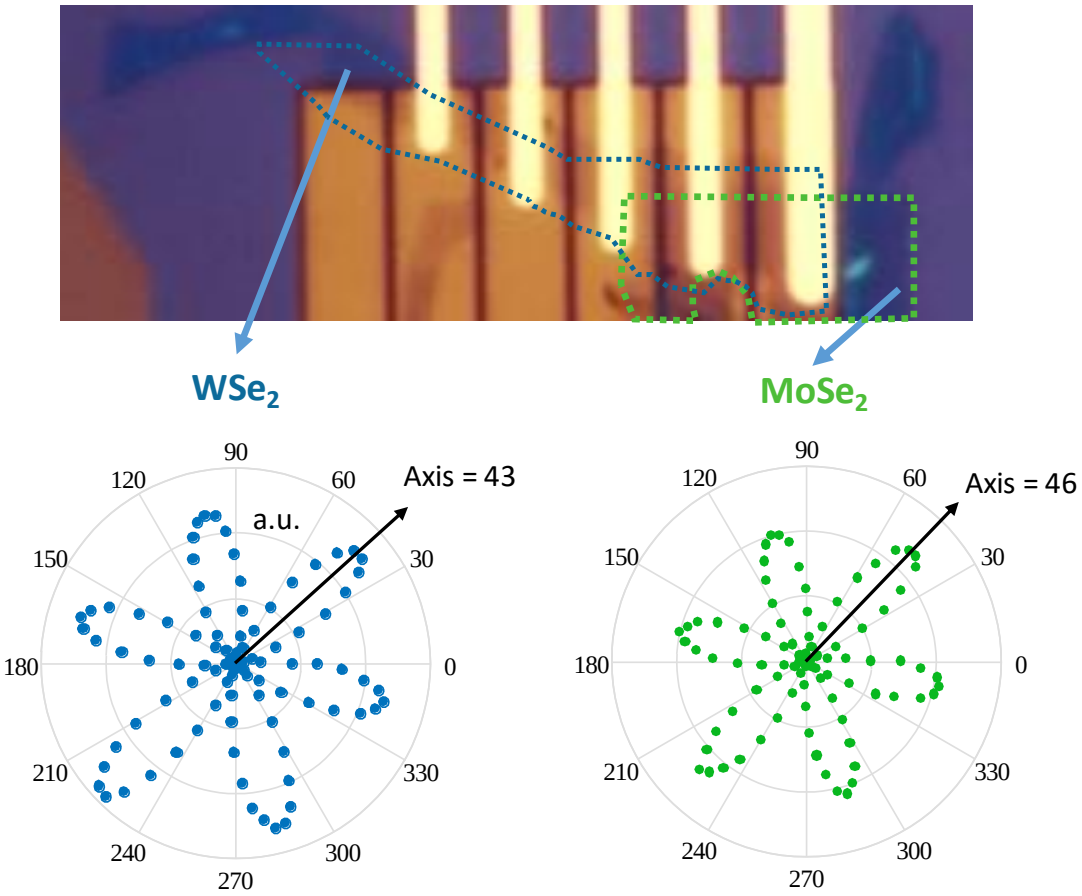

Figure 5.7. **Second Harmonic Generation (SHG) vs. Linear polarization angle of incident light**. Data taken from monolayer areas of constituent materials as indicated by the blue arrows. For WSe_2 ($MoSe_2$), incident light set to 1480 (1560) nm and SHG signal collected at 740 (780) nm. The maximum SHG signal corresponds to the armchair axes of each crystal[113]. Looking at the difference in the armchair of each we estimate a 3-degree twist angle for the heterostructure region

5.7 Interlayer Coupling Strength

Resonant excitation of the X_I enables us to compare the interlayer and intralayer exciton oscillator strengths. To do so, the spot size and power of the laser vs. wavelength was calibrated

using a knife edge and photodiode respectively. This allowed the PC to be normalized to the laser irradiance giving photoresponse units of $mA/(\mu W/um^2)$. In the intralayer region (Figure 5.8a) we see strongly coupled (large photoresponse) features as described above. In contrast, the interlayer photoresponse (Figure 5.8b) is about 200 times weaker. If we assume the photocurrent is proportional to number of optically generated excitons, which has a linear dependence on exciton oscillator strengths for a given photo excitation density, we infer that the X_I oscillator strength is two orders of magnitude smaller than intralayer excitons. This is consistent with theoretical prediction where, the strength of the exciton light coupling, determined by the oscillator strength, is proportional to the electron-hole spatial overlap. In the intralayer configuration (see illustration in Figure 5.8c), the electron and hole are confined to the same 2D layer and so have large overlap leading to strong light coupling. But in the interlayer (Figure 5.8d), they are separated to different layers resulting in minimal overlap and suppression of light coupling. Since this suppression is expected to be dependent on layer separation, which is sample dependent, the observed interlayer to intralayer coupling ratio here provides an order of magnitude estimation.

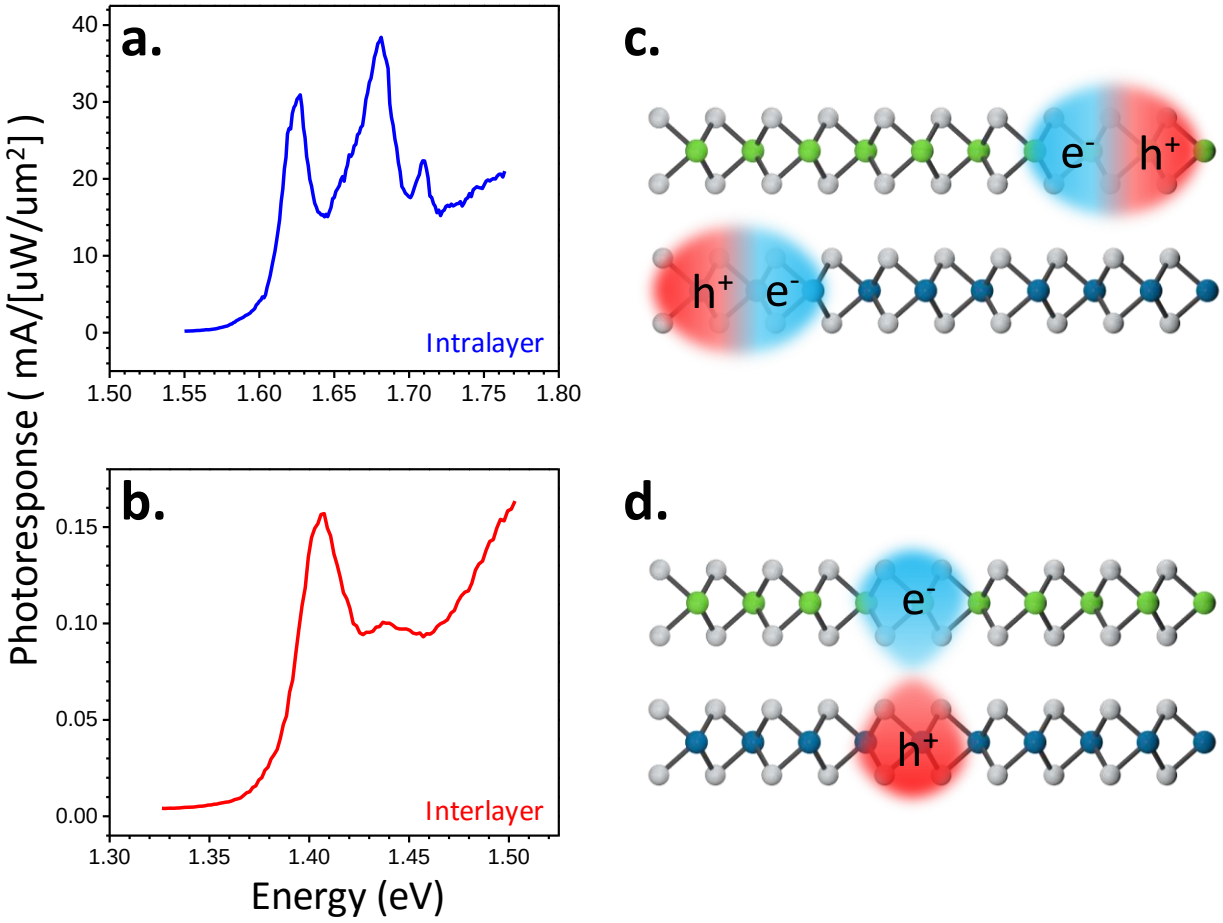

Figure 5.8. **Photoresponse comparison of interlayer to intralayer Excitons**. **a,** and **b,** show photoresponse as a function of laser excitation energy for intralayer and interlayer energy ranges respectively. **c** and **d,** illustrate qualitative wave function overlap between electrons and holes for intralayer and interlayer excitons respectively emphasizing on the interlayer exciton has small overlap.

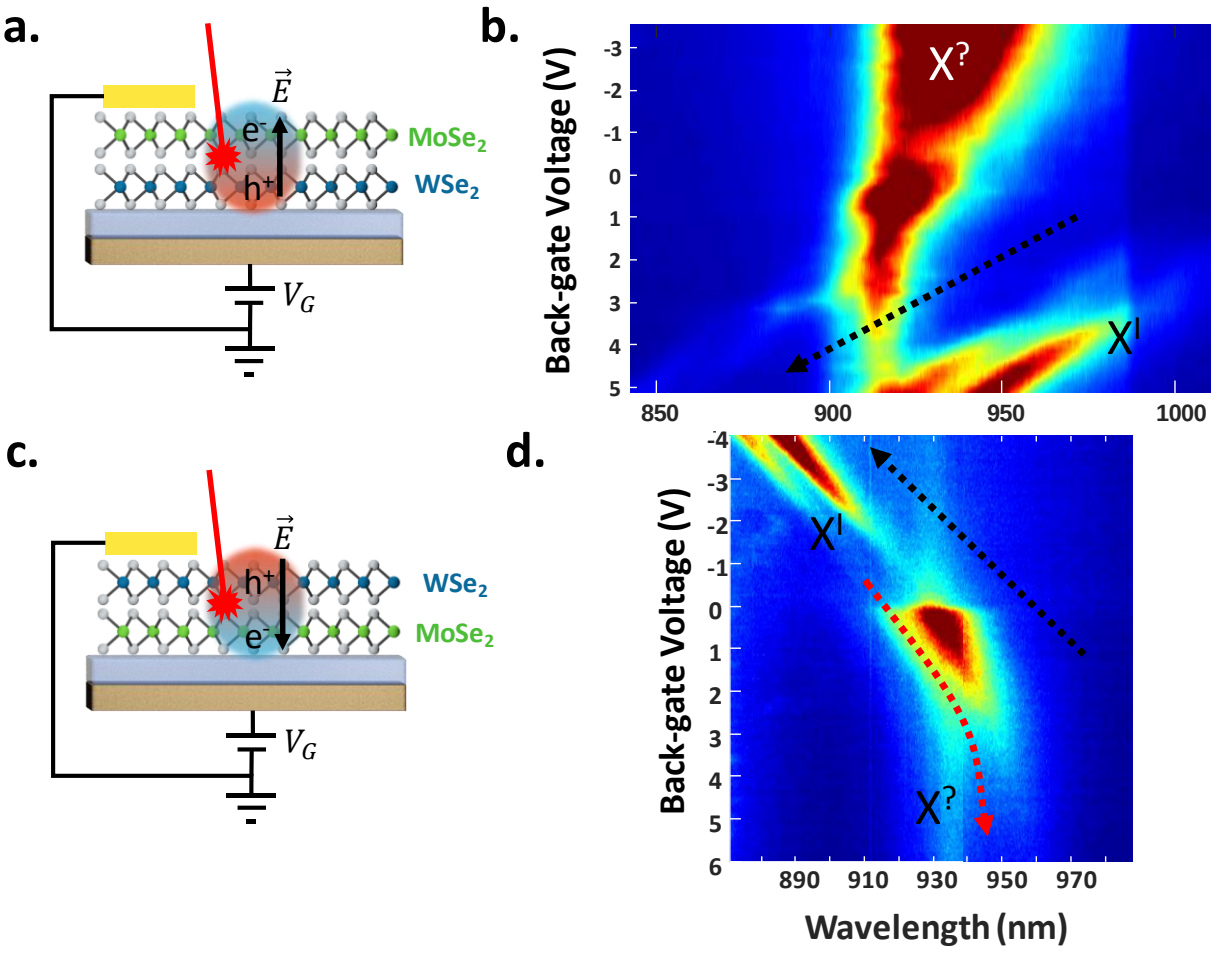

Figure 5.9. **Interlayer PL Gate Dependence and Stacking order**. **a (c),** $MoSe_2$-WSe_2 (WSe_2-MeSe2) HS junction has the interlayer electric field pointing up (down). **b (d),** Gate dependence PL of device in a (c). Interlayer exciton features (X^I) blue-shift along the black arrow direction with positive (negative) gate due to interlayer dipole energy tuning. Red arrow indicates reduction in dipole shifting due to possible charge screening. $X^?$ is an unidentified exciton feature that shows minimal gate dependence and is possibly related to $MoSe_2$ alone.

5.8 FINAL REMARKS

The interlayer exciton studied in this chapter has shown lifetimes that extend into the μs range[115]. Further, TMDs have recently been shown to be easily coupled to microfabricated photonic crystal cavities showing enhanced emission[53] and even low threshold optically pumped lasing[54]. If we can better understand the interlayer dynamics and couple this long lived emitter state to a resonant cavity, we predict the possibility of creating the first 2D nanolaser. Such a device could have profound implications for photonic circuits and components in general.

Finally, there has been a lot of observed spectral features of the interlayer exciton and more work is needed to identify the excitonic source of them all. We have performed preliminary gate dependent PL studies of HS of both stacking order (interlayer dipole due to charge transfer is reversed) to begin to shed light on this issue.

For $MoSe_2$ on top of WSe_2 (Figure 5.9a) the photoexcited electrons transfer to the top layer and the holes to the bottom creating an electric field pointing up corresponding to the coulomb interaction of the interlayer excitons. If a positive voltage is applied to the back gate the electric field is increased leading to an increase in the emission energy of the interlayer exciton (blue shifting of X^I in Figure 5.9b along the black arrow). Conversely with WSe_2 on top of $MoSe_2$ (Figure 5.9c) a negative voltage is required to blue-shift X^I (Figure 5.9d) since the interlayer dipole is now reverse with respect to the z-direction.

The above two behaviors are the only well understand interlayer exciton features as they correspond to dipole tuning by the gate which confirms the nature of the charge separated interlayer exciton[68]. However in figures Figure 5.9b and d we observe 3 other mysterious features: 1) In both figures, there is a peak that experiences less spectral shifting with gate that is around 930 nm ($X^?$ in both figures). Possibly this is the low energy feature observed in monolayer

$MoSe_2$ LEDs presented in Section 4.11. 2) In both figures, the interlayer exciton seems to be split into two peaks, such as at 950 nm and 925 nm at V_G = 5 V in Figure 5.9b. And in Figure 5.9b, both of these peaks having a higher energy copy seen as faint peaks at around 850 nm at V_G = 5 V. 3). The slope of the gate dependent emission energy drops off for Figure 5.9b in negative voltages and Figure 5.9d in positive voltages. This can be understood as possible charge screen of the gate by the bottom layer of the heterostructure. For instance, with $MoSe_2$ on the bottom, under a positive gate voltage photoexcited electrons charge transfer to the bottom layer and screen the positively charged gate. The dipole energy between the top and bottom layers is thus no longer modulated by the gate and the spectral shifting is reduced (red line in Figure 5.9d). For future HS studies of any kind it will be important to confirm all of these features through further PL, EL, and PC studies.

BIBLIOGRAPHY

1. Novoselov KS, Geim a K, Morozov S V, Jiang D, Zhang Y, Dubonos S V, Grigorieva I V, Firsov a a (2004) Electric field effect in atomically thin carbon films. Science 306:666–9. doi: 10.1126/science.1102896

2. Novoselov KS, Geim a K, Morozov S V, Jiang D, Katsnelson MI, Grigorieva I V, Dubonos S V, Firsov a a (2005) Two-dimensional gas of massless Dirac fermions in graphene. Nature 438:197–200. doi: 10.1038/nature04233

3. Bolotin KI, Sikes KJ, Jiang Z, Klima M, Fudenberg G, Hone J, Kim P, Stormer HL (2008) Ultrahigh electron mobility in suspended graphene. Solid State Commun 146:351–355. doi: 10.1016/j.ssc.2008.02.024

4. Zhu S, Yuan S, Janssen GC a. M (2014) Optical transmittance of multilayer graphene. EPL (Europhysics Lett 108:17007. doi: 10.1209/0295-5075/108/17007

5. Nair RR, Blake P, Grigorenko a N, Novoselov KS, Booth TJ, Stauber T, Peres NMR, Geim a K (2008) Fine structure constant defines visual transparency of graphene. Science 320:1308. doi: 10.1126/science.1156965

6. Geim a K, Grigorieva I V (2013) Van der Waals heterostructures. Nature 499:419–25. doi: 10.1038/nature12385

7. Watanabe K, Taniguchi T, Kanda H (2004) Direct-bandgap properties and evidence for ultraviolet lasing of hexagonal boron nitride single crystal. Nat Mater 3:404–409. doi: 10.1038/nmat1134

8. Dean CR, Young a F, Meric I, Lee C, Wang L, Sorgenfrei S, Watanabe K, Taniguchi T, Kim P, Shepard KL, Hone J (2010) Boron nitride substrates for high-quality graphene electronics. Nat Nanotechnol 5:722–726. doi: 10.1038/nnano.2010.172

9. Xue J, Sanchez-Yamagishi J, Bulmash D, Jacquod P, Deshpande A, Watanabe K, Taniguchi T, Jarillo-Herrero P, LeRoy BJ (2011) Scanning tunnelling microscopy and spectroscopy of ultra-flat graphene on hexagonal boron nitride. Nat Mater 10:282–285. doi: 10.1038/nmat2968

10. Novoselov KS, Jiang D, Schedin F, Booth TJ, Khotkevich V V, Morozov S V, Geim a K (2005) Two-dimensional atomic crystals. Proc Natl Acad Sci U S A 102:10451–3. doi: 10.1073/pnas.0502848102

11. Mak KF, Lee C, Hone J, Shan J, Heinz TF (2010) Atomically Thin MoS_2: A New Direct-Gap Semiconductor. Phys Rev Lett 105:2–5. doi: 10.1103/PhysRevLett.105.136805

12. Ross JS, Wu S, Yu H, Ghimire NJ, Jones AM, Aivazian G, Yan J, Mandrus DG, Xiao D, Yao W, Xu X (2013) Electrical control of neutral and charged excitons in a monolayer semiconductor. Nat Commun 4:1474. doi: 10.1038/ncomms2498

13. Jones AM, Yu H, Ghimire NJ, Wu S, Aivazian G, Ross JS, Zhao B, Yan J, Mandrus DG, Xiao D, Yao W, Xu X (2013) Optical generation of excitonic valley coherence in monolayer WSe_2. Nat Nanotechnol 8:634–8. doi: 10.1038/nnano.2013.151

14. Mak KF, He K, Lee C, Lee GH, Hone J, Heinz TF, Shan J (2013) Tightly bound trions in monolayer MoS2. Nat Mater 12:207–11. doi: 10.1038/nmat3505

15. He K, Kumar N, Zhao L, Wang Z, Mak KF, Zhao H, Shan J (2014) Tightly bound excitons in monolayer WSe_2. Phys Rev Lett 113:026803. doi: 10.1103/PhysRevLett.113.026803

16. Chernikov A, Berkelbach TC, Hill HM, Rigosi A, Li Y, Aslan OB, Reichman DR, Hybertsen MS, Heinz TF (2014) Exciton Binding Energy and Nonhydrogenic Rydberg Series in Monolayer WS2. Phys Rev Lett 113:076802. doi: 10.1103/PhysRevLett.113.076802

17. Zhu B, Chen X, Cui X (2014) Exciton Binding Energy of Monolayer WS2. Sci Rep 5:5. doi: 10.1038/srep09218

18. Xiao D, Liu G-B, Feng W, Xu X, Yao W (2012) Coupled Spin and Valley Physics in Monolayers of MoS_{2} and Other Group-VI Dichalcogenides. Phys Rev Lett 108:196802. doi: 10.1103/PhysRevLett.108.196802

19. Kioseoglou G, Hanbicki a. T, Currie M, Friedman a. L, Gunlycke D, Jonker BT (2012) Valley polarization and intervalley scattering in monolayer MoS2. Appl Phys Lett 101:221907. doi: 10.1063/1.4768299

20. Mak KF, He K, Shan J, Heinz TF (2012) Control of valley polarization in monolayer MoS_2 by optical helicity. Nat Nanotechnol 7:494–498. doi: 10.1038/nnano.2012.96

21. Cao T, Wang G, Han W, Ye H, Zhu C, Shi J, Niu Q, Tan P, Wang E, Liu B, Feng J (2012) Valley-selective circular dichroism of monolayer molybdenum disulphide. Nat Commun 3:887. doi: 10.1038/ncomms1882

22. Jariwala D, Sangwan VK, Lauhon LJ, Marks TJ, Hersam MC (2014) Emerging device applications for semiconducting two-dimensional transition metal dichalcogenides. ACS Nano 8:1102–20. doi: 10.1021/nn500064s

23. Butler SZ, Hollen SM, Cao L, Cui Y, Gupta JA, Gutiérrez HR, Heinz TF, Hong SS, Huang J, Ismach AF, Johnston-Halperin E, Kuno M, Plashnitsa V V, Robinson RD, Ruoff RS, Salahuddin S, Shan J, Shi L, Spencer MG, Terrones M, Windl W, Goldberger JE (2013) Progress, challenges, and opportunities in two-dimensional materials beyond graphene. ACS Nano 7:2898–926. doi: 10.1021/nn400280c

24. Xu M, Liang T, Shi M, Chen H (2013) Graphene-like two-dimensional materials. Chem Rev 113:3766–98. doi: 10.1021/cr300263a

25. Stébé B, Ainane A (1989) Ground state energy and optical absorption of excitonic trions

in two dimensional semiconductors. Superlattices Microstruct 5:545–548. doi: 10.1016/0749-6036(89)90382-0

26. Radisavljevic B, Radenovic A, Brivio J, Giacometti V, Kis A (2011) Single-layer MoS2 transistors. Nat Nanotechnol 6:147–150. doi: 10.1038/nnano.2010.279

27. Chen C-F, Park C-H, Boudouris BW, Horng J, Geng B, Girit C, Zettl A, Crommie MF, Segalman R a, Louie SG, Wang F (2011) Controlling inelastic light scattering quantum pathways in graphene. Nature 471:617–20. doi: 10.1038/nature09866

28. Lu Y, Goldsmith BR, Kybert NJ, Johnson a. TC (2010) DNA-decorated graphene chemical sensors. Appl Phys Lett 97:083107. doi: 10.1063/1.3483128

29. Ye Y, Ye Z, Gharghi M, Zhu H, Zhao M, Wang Y, Yin X, Zhang X (2014) Exciton-dominant electroluminescence from a diode of monolayer MoS 2. Appl Phys Lett 104:193508. doi: 10.1063/1.4875959

30. Chhowalla M, Shin HS, Eda G, Li L-J, Loh KP, Zhang H (2013) The chemistry of two-dimensional layered transition metal dichalcogenide nanosheets. Nat Chem 5:263–75. doi: 10.1038/nchem.1589

31. Larentis S, Fallahazad B, Tutuc E (2012) Field-effect transistors and intrinsic mobility in ultra-thin $MoSe_2$ layers. Appl Phys Lett 101:223104. doi: 10.1063/1.4768218

32. Wang L, Meric I, Huang PY, Gao Q, Gao Y, Tran H, Taniguchi T, Watanabe K, Campos LM, Muller D a, Guo J, Kim P, Hone J, Shepard KL, Dean CR (2013) One-dimensional electrical contact to a two-dimensional material. Science 342:614–7. doi: 10.1126/science.1244358

33. Xu S, Han Y, Long G, Wu Z, Chen X, Han T, Ye W, Lu H, Wu Y, Lin J, Shen J, Cai Y, He Y, Lortz R, Wang N (2015) High-quality BN / WSe 2 / BN heterostructure and its quantum oscillations. 2:

34. Britnell L, Gorbachev R V, Jalil R, Belle BD, Schedin F, Katsnelson MI, Eaves L, Morozov S V, Mayorov AS, Peres NMR, Neto AHC, Leist J, Geim AK, Ponomarenko L a, Novoselov KS (2012) Electron tunneling through ultrathin boron nitride crystalline barriers. Nano Lett 12:1707–10. doi: 10.1021/nl3002205

35. Lee G-H, Yu Y-J, Lee C, Dean C, Shepard KL, Kim P, Hone J (2011) Electron tunneling through atomically flat and ultrathin hexagonal boron nitride. Appl Phys Lett 99:243114. doi: 10.1063/1.3662043

36. Cao Y, Mishchenko A, Yu GL, Khestanova E, Rooney AP, Prestat E, Kretinin a V, Blake P, Shalom MB, Woods C, Chapman J, Balakrishnan G, Grigorieva I V, Novoselov KS, Piot B a, Potemski M, Watanabe K, Taniguchi T, Haigh SJ, Geim a K, Gorbachev R V (2015) Quality Heterostructures from Two-Dimensional Crystals Unstable in Air by Their Assembly in Inert Atmosphere. Nano Lett 15:4914–4921. doi: 10.1021/acs.nanolett.5b00648

37. Withers F, Del Pozo-Zamudio O, Mishchenko A, Rooney a. P, Gholinia A, Watanabe K, Taniguchi T, Haigh SJ, Geim a. K, Tartakovskii a. I, Novoselov KS (2015) Light-emitting diodes by band-structure engineering in van der Waals heterostructures. Nat Mater 14:301–306. doi: 10.1038/nmat4205

38. Kappera R, Voiry D, Yalcin SE, Branch B, Gupta G, Mohite AD, Chhowalla M (2014) Phase-engineered low-resistance contacts for ultrathin MoS2 transistors. Nat Mater 13:1128–1134. doi: 10.1038/nmat4080

39. Splendiani A, Sun L, Zhang Y, Li T, Kim J, Chim C-Y, Galli G, Wang F (2010) Emerging photoluminescence in monolayer MoS2. Nano Lett 10:1271–5. doi: 10.1021/nl903868w

40. Yin Z, Li HH, Jiang L, Shi Y, Sun Y, Lu G, Zhang Q, Chen X, Zhang H (2012) Single-layer MoS2 phototransistors. ACS Nano 6:74–80. doi: 10.1021/nn2024557

41. Lee HS, Min SW, Chang YG, Park MK, Nam T, Kim H, Kim JH, Ryu S, Im S (2012) MoS 2 nanosheet phototransistors with thickness-modulated optical energy gap. Nano Lett 12:3695–3700. doi: 10.1021/nl301485q

42. Choi W, Cho MY, Konar A, Lee JH, Cha G-B, Hong SC, Kim S, Kim J, Jena D, Joo J, Kim S (2012) High-detectivity multilayer MoS(2) phototransistors with spectral response from ultraviolet to infrared. Adv Mater 24:5832–6. doi: 10.1002/adma.201201909

43. Lopez-Sanchez O, Lembke D, Kayci M, Radenovic A, Kis A (2013) Ultrasensitive photodetectors based on monolayer MoS2. Nat Nanotechnol 8:1–5. doi: 10.1038/nnano.2013.100

44. Bernardi M, Palummo M, Grossman JC (2013) Extraordinary sunlight absorption and one nanometer thick photovoltaics using two-dimensional monolayer materials. Nano Lett 13:3664–70. doi: 10.1021/nl401544y

45. Britnell L, Ribeiro RM, Eckmann A, Jalil R, Belle BD, Mishchenko A, Kim Y-J, Gorbachev R V, Georgiou T, Morozov S V, Grigorenko AN, Geim AK, Casiraghi C, Castro Neto AH, Novoselov KS (2013) Strong light-matter interactions in heterostructures of atomically thin films. Science 340:1311–4. doi: 10.1126/science.1235547

46. Tsai M-L, Su S-H, Chang J-K, Tsai D-S, Chen C-H, Wu C-I, Li L-J, Chen L-J, He J-H (2014) Monolayer MoS2 Heterojunction Solar Cells. ACS Nano. doi: 10.1021/nn502776h

47. Sundaram RS, Engel M, Lombardo A, Krupke R, Ferrari AC, Avouris P, Steiner M (2013) Electroluminescence in single layer MoS2. Nano Lett 13:1416–1421. doi: 10.1021/nl400516a

48. Lopez-Sanchez O, Alarcon Llado E, Koman V, Fontcuberta I Morral A, Radenovic A, Kis A (2014) Light generation and harvesting in a van der waals heterostructure. ACS Nano 8:3042–3048. doi: 10.1021/nn500480u

49. Ross JS, Klement P, Jones AM, Ghimire NJ, Yan J, Mandrus DG, Taniguchi T, Watanabe

K, Kitamura K, Yao W, Cobden DH, Xu X (2014) Electrically tunable excitonic light-emitting diodes based on monolayer WSe_2 p-n junctions. Nat Nanotechnol 9:268–72. doi: 10.1038/nnano.2014.26

50. Pospischil A, Furchi MM, Mueller T (2014) Solar-energy conversion and light emission in an atomic monolayer p-n diode. Nat Nanotechnol 9:257–61. doi: 10.1038/nnano.2014.14

51. Baugher BWH, Churchill HOH, Yang Y, Jarillo-Herrero P (2014) Optoelectronic devices based on electrically tunable p-n diodes in a monolayer dichalcogenide. Nat Nanotechnol 9:262–7. doi: 10.1038/nnano.2014.25

52. Zhang YJ, Oka T, Suzuki R, Ye JT, Iwasa Y (2014) Electrically switchable chiral light-emitting transistor. Science 344:725–8. doi: 10.1126/science.1251329

53. Wu S, Buckley S, Jones AM, Ross JS, Ghimire NJ, Yan J, Mandrus DG, Yao W, Hatami F, Vučković J, Majumdar A, Xu X (2014) Control of two-dimensional excitonic light emission via photonic crystal. 2D Mater 1:011001. doi: 10.1088/2053-1583/1/1/011001

54. Wu S, Buckley S, Schaibley JR, Feng L, Yan J, Mandrus DG, Hatami F, Yao W, Vučković J, Majumdar A, Xu X (2015) Monolayer semiconductor nanocavity lasers with ultralow thresholds. Nature 520:69–72. doi: 10.1038/nature14290

55. Zhu ZY, Cheng YC, Schwingenschlögl U (2011) Giant spin-orbit-induced spin splitting in two-dimensional transition-metal dichalcogenide semiconductors. Phys Rev B 84:153402. doi: 10.1103/PhysRevB.84.153402

56. Zeng H, Dai J, Yao W, Xiao D, Cui X (2012) Valley polarization in MoS2 monolayers by optical pumping. Nat Nanotechnol 7:490–3. doi: 10.1038/nnano.2012.95

57. Yuan H, Bahramy MS, Morimoto K, Wu S, Nomura K, Yang B-J, Shimotani H, Suzuki R, Toh M, Kloc C, Xu X, Arita R, Nagaosa N, Iwasa Y (2013) Zeeman-type spin splitting controlled by an electric field. Nat Phys 9:563–569. doi: 10.1038/nphys2691

58. Wu SF, Ross JS, Liu GB, Aivazian G, Jones A, Fei ZY, Zhu WG, Xiao D, Yao W, Cobden D, Xu XD (2013) Electrical tuning of valley magnetic moment through symmetry control in bilayer MoS2. Nat Phys 9:149–153. doi: 10.1038/nphys2524

59. Dean CR, Wang L, Maher P, Forsythe C, Ghahari F, Gao Y, Katoch J, Ishigami M, Moon P, Koshino M, Taniguchi T, Watanabe K, Shepard KL, Hone J, Kim P (2013) Hofstadter's butterfly and the fractal quantum Hall effect in moiré superlattices. Nature 497:598–602. doi: 10.1038/nature12186

60. Ponomarenko L a, Gorbachev R V, Yu GL, Elias DC, Jalil R, Patel a a, Mishchenko a, Mayorov a S, Woods CR, Wallbank JR, Mucha-Kruczynski M, Piot B a, Potemski M, Grigorieva I V, Novoselov KS, Guinea F, Fal'ko VI, Geim a K (2013) Cloning of Dirac fermions in graphene superlattices. Nature 497:594–7. doi: 10.1038/nature12187

61. Hunt B, Sanchez-Yamagishi JD, Young a F, Yankowitz M, LeRoy BJ, Watanabe K,

Taniguchi T, Moon P, Koshino M, Jarillo-Herrero P, Ashoori RC (2013) Massive Dirac fermions and Hofstadter butterfly in a van der Waals heterostructure. Science 340:1427–30. doi: 10.1126/science.1237240

62. Kang J, Tongay S, Zhou J, Li J, Wu J (2013) Band offsets and heterostructures of two-dimensional semiconductors. Appl Phys Lett 102:012111. doi: 10.1063/1.4774090

63. Kośmider K, Fernández-Rossier J (2013) Electronic properties of the MoS2-WS2 heterojunction. Phys Rev B 87:075451. doi: 10.1103/PhysRevB.87.075451

64. Terrones H, López-Urías F, Terrones M (2013) Novel hetero-layered materials with tunable direct band gaps by sandwiching different metal disulfides and diselenides. Sci Rep 3:1549. doi: 10.1038/srep01549

65. Fogler MM, Butov L V, Novoselov KS (2014) High-temperature superfluidity with indirect excitons in van der Waals heterostructures. Nat Commun 5:5. doi: 10.1038/ncomms5555

66. Hong X, Kim J, Shi S-F, Zhang Y, Jin C, Sun Y, Tongay S, Wu J, Zhang Y, Wang F (2014) Ultrafast charge transfer in atomically thin MoS2/WS2 heterostructures. Nat Nanotechnol 9:682–686. doi: 10.1038/nnano.2014.167

67. Ceballos F, Bellus M, Chiu H, Zhao H (2014) Ultrafast Charge Separation and Indirect Exciton Formation in a MoS_2-MoSe_2 van der Waals heterostructure. ACS Nano 12717–12724.

68. Rivera P, Schaibley JR, Jones AM, Ross JS, Wu S, Aivazian G, Klement P, Seyler K, Clark G, Ghimire NJ, Yan J, Mandrus DG, Yao W, Xu X (2015) Observation of long-lived interlayer excitons in monolayer $MoSe_2$–WSe_2 heterostructures. Nat Commun 6:6242. doi: 10.1038/ncomms7242

69. Li X, Magnuson CW, Venugopal A, Tromp RM, Hannon JB, Vogel EM, Colombo L, Ruoff RS (2011) Large-area graphene single crystals grown by low-pressure chemical vapor deposition of methane on copper. J Am Chem Soc. doi: 10.1021/ja109793s

70. Kim KS, Zhao Y, Jang H, Lee SY, Kim JM, Kim KS, Ahn J-H, Kim P, Choi J-Y, Hong BH (2009) Large-scale pattern growth of graphene films for stretchable transparent electrodes. Nature 457:706–710. doi: 10.1038/nature07719

71. Zomer PJ, Guimarães MHD, Brant JC, Tombros N, van Wees BJ (2014) Fast pick up technique for high quality heterostructures of bilayer graphene and hexagonal boron nitride. Appl Phys Lett 105:5. doi: 10.1063/1.4886096

72. Lampert M (1958) Mobile and Immobile Effective-Mass-Particle Complexes in Nonmetallic Solids. Phys Rev Lett 1:450–453. doi: 10.1103/PhysRevLett.1.450

73. Finkelstein G, Shtrikman H, Bar-Joseph I (1996) Negatively and positively charged excitons in GaAs/Al_xGa_{1-x}As quantum wells. Phys Rev B 53:R1709–R1712. doi:

10.1103/PhysRevB.53.R1709

74. Kheng K, Cox R, D'Aubigné M (1993) Observation of negatively charged excitons X^- in semiconductor quantum wells. Phys Rev Lett 71:1752–1755.

75. Scholes GD, Rumbles G (2006) Excitons in nanoscale systems. Nat Mater 5:683–696. doi: 10.1038/nmat1710

76. High AA, Novitskaya EE, Butov L V, Hanson M, Gossard AC (2008) Control of exciton fluxes in an excitonic integrated circuit. Science 321:229–231. doi: 10.1126/science.1157845

77. Carter SG, Birkedal V, Wang CS, Coldren L a, Maslov a V, Citrin DS, Sherwin MS (2005) Quantum coherence in an optical modulator. Science 310:651–653. doi: 10.1126/science.1116195

78. Kira M, Koch SW, Smith RP, Hunter a. E, Cundiff ST (2011) Quantum spectroscopy with Schrödinger-cat states. Nat Phys 7:799–804. doi: 10.1038/nphys2091

79. Eisenstein JP, Macdonald a H (2004) Bose-Einstein condensation of excitons in bilayer electron systems. Nature 432:691–4. doi: 10.1038/nature03081

80. Butov L V, Gossard a C, Chemla DS (2002) Macroscopically ordered state in an exciton system. Nature 418:751–4. doi: 10.1038/nature00943

81. Deng H, Yamamoto Y (2010) Exciton-polariton Bose-Einstein condensation. Rev Mod Phys 82:1489–1537. doi: 10.1103/RevModPhys.82.1489

82. Chen W, Fritze M, Walecki W, Nurmikko A, Ackley D, Hong J, Chang L (1992) Excitonic enhancement of the Fermi-edge singularity in a dense two-dimensional electron gas. Phys Rev B 45:8464–8477. doi: 10.1103/PhysRevB.45.8464

83. Finkelstein G, Shtrikman H, Bar-Joseph I (1995) Optical Spectroscopy of a Two-Dimensional Electron Gas near the Metal-Insulator Transition. Phys Rev Lett 74:976–979. doi: 10.1103/PhysRevLett.74.976

84. Evans BL, Hazelwood RA (1971) Optical and structural properties of $MoSe_2$. Phys status solidi 4:181–192. doi: 10.1002/pssa.2210040119

85. Coehoorn R, Haas C, de Groot R (1987) Electronic structure of $MoSe_2$, MoS_2, and WSe_2. II. The nature of the optical band gaps. Phys Rev B 35:6203–6206. doi: 10.1103/PhysRevB.35.6203

86. Korn T, Heydrich S, Hirmer M, Schmutzler J, Schüller C (2011) Low-temperature photocarrier dynamics in monolayer MoS2. Appl Phys Lett 99:102109. doi: 10.1063/1.3636402

87. Warburton R, Schaflein C, Haft D, Bickel F, Lorke A, Karrai K, Garcia J, Schoenfeld W,

Petroff P (2000) Optical emission from a charge-tunable quantum ring. Nature 405:926–929. doi: 10.1038/35016030

88. Esser A, Runge E, Zimmermann R (2000) Photoluminescence and radiative lifetime of trions in GaAs quantum wells. Phys Rev B 62:8232–8239.

89. Vercik a., Gobato YG, Brasil MJSP (2002) Thermal equilibrium governing the formation of negatively charged excitons in resonant tunneling diodes. J Appl Phys 92:1888. doi: 10.1063/1.1494851

90. Siviniant J, Scalbert D, Kavokin a., Coquillat D, Lascaray J-P (1999) Chemical equilibrium between excitons, electrons, and negatively charged excitons in semiconductor quantum wells. Phys Rev B 59:1602–1604. doi: 10.1103/PhysRevB.59.1602

91. Esser a., Runge E, Zimmermann R, Langbein W (2000) Trions in GaAs Quantum Wells: Photoluminescence Lineshape Analysis. Phys Status Solidi 178:489–494. doi: 10.1002/1521-396X(200003)178:1<489::AID-PSSA489>3.0.CO;2-R

92. O'Donnell KP, Chen X (1991) Temperature dependence of semiconductor band gaps. Appl Phys Lett 58:2924–2926. doi: 10.1063/1.104723

93. Stébé B, Feddi E, Ainane A, Dujardin F (1998) Optical and magneto-optical absorption of negatively charged excitons in three- and two-dimensional semiconductors. Phys Rev B 58:9926–9932. doi: 10.1103/PhysRevB.58.9926

94. Tongay S, Zhou J, Ataca C, Lo K, Matthews TS, Li J, Grossman JC, Wu J (2012) Thermally Driven Crossover from Indirect toward Direct Bandgap in 2D Semiconductors: $MoSe_2$ versus MoS2. Nano Lett 12:5576–5580. doi: 10.1021/nl302584w

95. Chen J, Perebeinos V, Freitag M, Tsang J, Fu Q, Liu J, Avouris P (2005) Bright infrared emission from electrically induced excitons in carbon nanotubes. Science 310:1171–4. doi: 10.1126/science.1119177

96. Marty L, Adam E, Albert L, Doyon R, Ménard D, Martel R (2006) Exciton Formation and Annihilation during 1D Impact Excitation of Carbon Nanotubes. Phys Rev Lett 96:136803. doi: 10.1103/PhysRevLett.96.136803

97. Mann D, Kato YK, Kinkhabwala A, Pop E, Cao J, Wang X, Zhang L, Wang Q, Guo J, Dai H (2007) Electrically driven thermal light emission from individual single-walled carbon nanotubes. Nat Nanotechnol 2:33–8. doi: 10.1038/nnano.2006.169

98. Kioseoglou G, Yasar M, Li C, Korkusinski M, Diaz-Avila M, Hanbicki A, Hawrylak P, Petrou A, Jonker B (2008) Intershell Exchange and Sequential Electrically Injected Spin Populations of InAs Quantum-Dot Shell States. Phys Rev Lett 101:227203. doi: 10.1103/PhysRevLett.101.227203

99. Xia F, Steiner M, Lin Y, Avouris P (2008) A microcavity-controlled, current-driven, on-

chip nanotube emitter at infrared wavelengths. Nat Nanotechnol 3:609–13. doi: 10.1038/nnano.2008.241

100. Essig S, Marquardt CW, Vijayaraghavan A, Ganzhorn M, Dehm S, Hennrich F, Ou F, Green AA, Sciascia C, Bonaccorso F, Bohnen K-P, Löhneysen H v, Kappes MM, Ajayan PM, Hersam MC, Ferrari AC, Krupke R (2010) Phonon-assisted electroluminescence from metallic carbon nanotubes and graphene. Nano Lett 10:1589–94. doi: 10.1021/nl9039795

101. Mueller T, Kinoshita M, Steiner M, Perebeinos V, Bol A a, Farmer DB, Avouris P (2010) Efficient narrow-band light emission from a single carbon nanotube p-n diode. Nat Nanotechnol 5:27–31. doi: 10.1038/nnano.2009.319

102. Shambat G, Ellis B, Majumdar A, Petykiewicz J, Mayer MA, Sarmiento T, Harris J, Haller EE, Vučković J (2011) Ultrafast direct modulation of a single-mode photonic crystal nanocavity light-emitting diode. Nat Commun 2:539. doi: 10.1038/ncomms1543

103. Zhao W, Ghorannevis Z, Chu L, Toh M, Kloc C, Tan P-H, Eda G (2013) Evolution of electronic structure in atomically thin sheets of WS2 and WSe_2. ACS Nano 7:791–7. doi: 10.1021/nn305275h

104. Huang J-K, Pu J, Hsu C-L, Chiu M-H, Juang Z-Y, Chang Y-H, Chang W-H, Iwasa Y, Takenobu T, Li L-J (2014) Large-Area Synthesis of Highly Crystalline WSe_2 Monolayers and Device Applications. ACS Nano 8:923–930. doi: 10.1021/nn405719x

105. Shi H, Yan R, Bertolazzi S, Brivio J, Gao B, Kis A, Jena D, Xing HG, Huang L (2013) Exciton dynamics in suspended monolayer and few-layer MoS_2 2D crystals. ACS Nano 7:1072–80. doi: 10.1021/nn303973r

106. Lagarde D, Bouet L, Marie X, Zhu CR, Liu BL, Amand T, Urbaszek B, Tan PH (2014) Carrier and Polarization Dynamics in Monolayer MoS2. Phys Rev Lett 112:047401. doi: 10.1103/PhysRevLett.112.047401

107. Sim S, Park J, Song J-G, In C, Lee Y-S, Kim H, Choi H (2013) Exciton dynamics in atomically thin MoS2: Interexcitonic interaction and broadening kinetics. Phys Rev B 88:075434. doi: 10.1103/PhysRevB.88.075434

108. Fushman I, Englund D, Vučković J (2005) Coupling of PbS quantum dots to photonic crystal cavities at room temperature. Appl Phys Lett 87:241102. doi: 10.1063/1.2138792

109. Yao W, Xiao D, Niu Q (2008) Valley-dependent optoelectronics from inversion symmetry breaking. Phys Rev B 77:235406. doi: 10.1103/PhysRevB.77.235406

110. Kormányos A, Zólyomi V, Drummond ND, Rakyta P, Burkard G, Fal'Ko VI (2013) Monolayer MoS2: Trigonal warping, the Γ valley, and spin-orbit coupling effects. Phys Rev B - Condens Matter Mater Phys 88:045416. doi: 10.1103/PhysRevB.88.045416

111. Liu G Bin, Shan WY, Yao Y, Yao W, Xiao D (2013) Three-band tight-binding model for

monolayers of group-VIB transition metal dichalcogenides. Phys Rev B - Condens Matter Mater Phys 88:1–10. doi: 10.1103/PhysRevB.88.085433

112. Yu H, Wu Y, Liu G-B, Xu X, Yao W (2014) Nonlinear Valley and Spin Currents from Fermi Pocket Anisotropy in 2D Crystals. Phys Rev Lett 113:1–5. doi: 10.1103/PhysRevLett.113.156603

113. Seyler KL, Schaibley JR, Gong P, Rivera P, Jones AM, Wu S, Yan J, Mandrus DG, Yao W, Xu X (2015) Electrical control of second-harmonic generation in a WSe_2 monolayer transistor. Nat Nanotechnol 1–5. doi: 10.1038/nnano.2015.73

114. He Y-M, Clark G, Schaibley JR, He Y, Chen M-C, Wei Y-J, Ding X, Zhang Q, Yao W, Xu X, Lu C-Y, Pan J-W (2015) Single quantum emitters in monolayer semiconductors. Nat Nanotechnol 10:497–502. doi: 10.1038/nnano.2015.75

115. Rivera P, Seyler KL, Yu H, Schaibley JR, Yan J, Mandrus DG, Yao W, Xu X (2016) Valley-polarized exciton dynamics in a 2D semiconductor heterostructure. Science (80-) 351:688–691. doi: 10.1126/science.aac7820

116. Lee C-H, Lee G, van der Zande AM, Chen W, Li Y, Han M, Cui X, Arefe G, Nuckolls C, Heinz TF, Guo J, Hone J, Kim P (2014) Atomically thin p-n junctions with van der Waals heterointerfaces. Nat Nanotechnol 1–29. doi: 10.1038/nnano.2014.150

117. Chiu M, Zhang C, Shiu HW, Chuu C, Chen C-H, Chang CS, Chen C, Chou M, Shih C, Li L (2014) Determination of band alignment in transition metal dichalcogenides heterojunctions. 20.

118. Wilson NR, Nguyen P V., Seyler KL, Rivera P, Marsden AJ, Laker ZPL, Constantinescu GC, Kandyba V, Barinov A, Hine NDM, Xu X, Cobden DH (2016) Band parameters and hybridization in 2D semiconductor heterostructures from photoemission spectroscopy. 10.

119. Yu H, Wang Y, Tong Q, Xu X, Yao W (2015) Anomalous Light Cones and Valley Optical Selection Rules of Interlayer Excitons in Twisted Heterobilayers. Phys Rev Lett 115:187002. doi: 10.1103/PhysRevLett.115.187002

120. Furchi MM, Pospischil A, Libisch F, Burgdörfer J, Mueller T (2014) Photovoltaic effect in an electrically tunable Van der Waals heterojunction. Nano Lett 14:4785–4791. doi: 10.1021/nl501962c

APPENDIX A

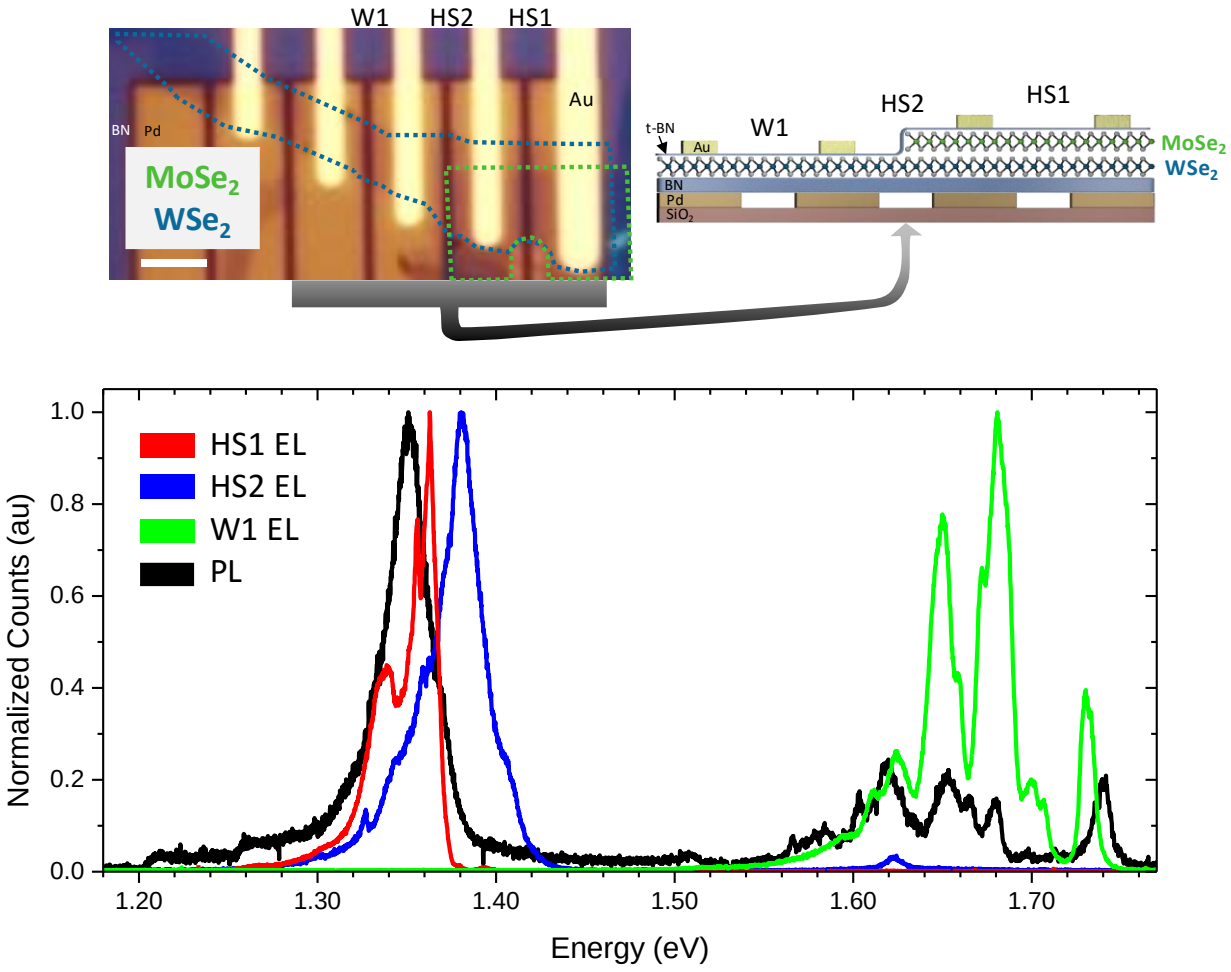

The above data taken is under similar voltages as discussed in Section 5.4: Band alignment and transport. Here the EL of HS1 and W1 are compared above to the photoluminescence (PL) of undoped HS1 (black). In red is the full-HS device HS1 which shows good spectral alignment with the PL. This hints that the half-HS device HS2 (blue) described in Chapter 5, which is blue-shifted from PL, is possibly experiencing edge effects which have been known to blue-shift PL. Finally, in green we have the emission from the single layer WSe_2 device W1 which shows EL only from intralayer exciton states between 1.6 and 1.74 eV[49].

VITA

Jason Solomon Ross was born to Ellie and Elliot Ross in Glendale, CA and raised in Agoura Hills, CA. After high school he attended Santa Barbara Community College where he found a passion for physics and eventually found an opportunity to perform his first research on gallium nitride high mobility transistors at UCSB. This experience exposed him to the wonders of clean room microfabrication and the physics of electron transport in confined systems. He subsequently transferred to UC Berkeley and obtained his BA in Physics while performing research in the thermodynamics of silicon nanowires using a nanocalorimeter device-on-a-chip. At the time of his graduation, he had acquired a strong interest in two-dimensional materials, specifically graphene, which led him to attend graduate school at the University of Washington and work under the tutelage of Dr. Xiaodong Xu. This decision proved to be his most prescient as no other experience has taught him more about how to perform research on the cutting-edge of science.